# Characterization of Performance and Current Drive Mechanism for the Rotating Magnetic Field Thruster

by

Christopher L. Sercel

A dissertation submitted in partial fulfillment
of the requirements for the degree of
Doctor of Philosophy
(Aerospace Engineering)
in the University of Michigan
2024

Doctoral Committee:

Assistant Professor Benjamin A. Jorns, Chair
Professor Emeritus Alec D. Gallimore
Professor Ryan D. McBride
Dr. Kurt A. Polzin, NASA Marshall Space Flight Center

Christopher L. Sercel
csercel@umich.edu
ORCID iD: 0009-0006-5374-4689

# DEDICATION

For Danielle
I practice the sacred arts so that you'll think I'm cool

# ACKNOWLEDGEMENTS

The completion of this work would not have been possible without the support of so many people who have helped along the way. I'd like to acknowledge some of them here.

**To my wife Danielle**: I can't describe how important your support has been. I would never have gotten this far without you to keep me going. I love you.

**To my parents**: I will be forever grateful for the curiosity and respect for knowledge and physical insight that you have instilled in me from an early age. I can say with confidence that I would not have taken the path I did if it weren't for those early science fairs and tinkering around in the garage with carbon arcs and Jacob's ladders. You gave me the structure and oversight not to have electrocuted myself, but enough freedom to be able to learn from a shock or two.

**To my brothers**: You both are such a large part of who I am today. Alex, thank you for leading the way our whole lives. Who knows if I would even have decided to pursue a doctorate if my big brother didn't do it first. Nick, your friendship means the world to me. I love being able to blow off some steam by getting way too upset at video games with you.

**To Tate**: I shudder to think how much longer this whole process would have taken without your partnership working on this thruster. Through all the late-night pumpdowns and early-next-morning thruster failures, entire data sets taken on the last day of the campaign, and thruster builds and re-builds, its been a team effort. Putting out fires (only occasionally literally) wouldn't have been the same with anyone else.

**To the rest of my colleagues at PEPL**: Thank you for helping to keep PEPL such a wonderful place to work and learn. I initially chose to do my doctorate here in no small part because I felt like the students actually liked each other when I came to visit. Grad school is a stressful place to be, and nothing helps quite like knowing everyone else in the trenches with you has your back.

**To Ben**: When asked advice from undergraduates how to go about choosing the graduate program that's right for them, I often give the advice to view the doctoral process less as

enrolling in a school and more as entering into a master/apprentice relationship. Thank you for your mentorship throughout the last five years. I couldn't imagine a better example to follow than yours.

This work was supported by NASA Space Technology Research Fellowship Grant 80NSSC18K1190.

# TABLE OF CONTENTS

# LIST OF FIGURES

FIGURE

# LIST OF TABLES

TABLE

# ABSTRACT

The Rotating Magnetic Field (RMF) Thruster is a propulsion concept which, depending on the operating regime, could enable a wide variety of mission architectures. The RMF thruster can be operated either in the pulsed-mode, ejecting dense field-reversed configuration (FRC) plasmoids to produce impulse, or in the continuous wave (CW)-mode, producing a steady jet of plasma. Operation in pulsed-mode causes the RMF thruster to resemble an inductive pulsed plasma thruster, though avoiding the very high voltage and current transients which those devices require and which make power supply design especially difficult. Operation in the CW-mode causes the RMF thruster to resemble an electrodeless applied field magnetoplasmadynamic thruster, with the lack of electrodes removing a key lifetime limitation. Critically, in either case the RMF thruster's lack of plasma wetted electrodes make it ideal for in-situ resource utilization, air-breathing, or multimode propulsion architechtures, all of which demand the capability to operate on unconventional, often oxidizing, propellants.

Despite these potential advantages, however, performance characterization of this thruster design remains sparse, with relatively few groups having made thrust and efficiency estimates. Indeed, no direct thrust measurements to our knowledge have been published. Scaling laws for the RMF thruster, too, are unconvincing, with no realistic upper bound to performance being suggested from the theory employed to date. In this work, we seek to remedy this gap in knowledge by designing, building, and directly characterizing the RMF thruster with an eye towards performance trends. Observations of those trends can then help to inspire further insight into the physics behind RMF thruster behavior and eventually provide intuition as to how to optimize this device.

Two devices are designed and used in this work, with results from the first directly informing the design of the second. We first employ a first-principles approach based on existing theory for RMF current drive to arrive at the design for the PEPL RMFv2 thruster. We then use it to make the first ever direct performance measurements for this class of device. While efficiency is found to be low, the RMFv2 thruster's verified performance allows us to employ probing techniques to understand loss mechanisms and whether the RMF current drive is indeed functioning as intended. Satisfied that current is being produced and having gained insight into how power is inefficiently converted into kinetic energy in the plume,

we present the updated PEPL RMFv3 thruster. The enhanced flexibility of this improved test article—including capability to operate in the CW-mode for the first time for an RMF thruster—allows us to explore operating parameter space even further. Our results for this characterization campaign contradict existing RMF current drive theory and inspire a re-examination of current generation scaling laws. Our updated model is compared to experimental data and is found to match quantitatively. This new model presents a much different picture for the ideal operational regime for the RMF thruster.

We present throughout this work the first direct performance measurement of an RMF thruster, direct evidence of FRC plasmoid formation, acceleration, and ejection in an RMF thruster, as well as a significant update to the analytic model used for this device which has gone largely unchallenged for over 60 years. Ultimately, we have greatly improved our understanding of the physics behind RMF current generation and plasma acceleration, and have grounded this intuition in experiment. The knowledge produced in this work will help guide future research into the RMF thruster toward realizing the advantages this device has to offer.

# CHAPTER 1

# Introduction

## 1.1 Electric Propulsion

### 1.1.1 The Rocket Equation

At its most fundamental, the purpose of any propulsion device—be it a gridded ion thruster or jet engine—is to accelerate propellant to high speed and eject in the opposite direction of vehicle motion. Thrust is produced by momentum transfer to that propellant. Applying conservation of momentum to such a system and solving for the final velocity of the vehicle results in the equation

$$\Delta v = v_{ex} \ln \left( \frac{M_0}{M_f} \right) \tag{1.1}$$

where $\Delta v$ is the change in vehicle velocity, $v_{ex}$ is the effective exhaust velocity of the propellant, and $M_0$ and $M_f$ are the initial and final masses after having released the propellant. Eq. 1.1 is known as the rocket equation, and was most famously derived by Konstantin Tsiolkovsky in 1897. Formulation in terms of $\Delta v$ is crucial for space applications, where the difficulty of reaching a target is more often measured in the change of velocity required for orbital injection than the actual distance to be traversed. In the case of station-keeping maneuvers meanwhile, a higher $\Delta v$ capability implies a longer spacecraft lifetime on orbit. Eq. 1.1 implies that the higher the exhaust velocity, the higher $\Delta v$ can be achieved with the same propellant mass fraction. A higher initial mass fraction in turn represents cost, as the propellant mass must be launched into orbit along with the payload. High exhaust velocities, therefore, are crucial to enable challenging mission architectures at reasonable cost.

Of course, energy must be imparted to the propellant to accelerate it to the high speeds necessary for propellant mass-efficient operation. Chemical rockets access the energy stored in chemical bonds to provide this power. This provides the advantage that energy can be imparted into the propellant at high rate, limited only by chemical reaction speed. However,

it also results in a fundamental limitation that the energy imparted to the propellant can only be as great as the energy stored in those bonds per unit mass $\epsilon_i$. Applying conservation of energy per unit mass results in the limit

$$v_{ex,chem} = \sqrt{2\epsilon_i} \tag{1.2}$$

for a perfectly efficient system, where $\epsilon_i$ refers to the specific energy of the reaction. No chemical rocket, therefore, can achieve exhaust velocities greater than $\sim \mathcal{O}(10^3)$ m/s.

In electric propulsion, meanwhile, energy is stored electrically and imparted to the propellant by various means. This work focuses on plasma propulsion, in which a neutral propellant gas is ionized so that the resulting free electrons and ions can be manipulated with electric and magnetic fields and thereby accelerated to great speeds. While electric propulsion takes many forms, all types share the same advantage: the power source is divorced from the propellant, allowing in principle arbitrarily high specific energy and therefore exhaust velocities:

$$v_{ex,EP} = \sqrt{\frac{2P}{\dot{m}}} \tag{1.3}$$

for mass flow rate $m$ and input power $P$. Typical exhaust velocities for electric propulsion systems in use today are approximately an order of magnitude higher than chemical propulsion technologies. Electric propulsion can therefore be highly effective from the perspective of propellant mass requirements to achieve a given $\Delta v$.

### 1.1.2 Key Figures of Merit

Several key figures of merit are used to compare electric propulsion devices. First, thrust $T$ can be derived directly from the same conservation of momentum framework as was used to arrive at the rocket equation:

$$T = \dot{m} v_{ex}. \tag{1.4}$$

With higher thrust, the time required to reach final velocity can be reduced, which is beneficial not only from a trip time perspective but also to minimize non-ideal effects such as gravity loss. Thrust for electric propulsion systems is low relative to chemical rockets (often measured in milliNewtons, although lower and higher thrust systems exist), but can be applied over a long period of time (thruster lifetime demonstrated to over 10,000 hours for the recent Psyche mission, for example [2])to achieve high total momentum change. Specific

impulse $I_{sp}$ is defined as

$$I_{sp} = \frac{v_{ex}}{g_0} \tag{1.5}$$

where $g$ is the gravitational constant measured at sea level. Intuitively, $I_{sp}$ refers to the change in momentum which can be achieved by the propulsion system per unit weight of propellant. The higher the $I_{sp}$, the greater $\Delta v$ can be achieved at a given mass fraction. Next, the total electrical efficiency $\eta$ of a device can be calculated by examining the ratio of axially-directed jet power to total input power

$$\eta = \frac{P_J}{P} = \frac{T^2}{2\dot{m}P}. \tag{1.6}$$

Significantly, thrust-to-power $\frac{T}{P}$ and specific impulse trade with each other at a given efficiency. While a higher $I_{sp}$ can be desirable to conserve propellant, having too high of an $I_{sp}$ can lead to prohibitively high trip times due to the commensurately lower thrust for the fixed power available to the spacecraft. Different electric propulsion systems tend to operate efficiently at varying thrust-to-power and specific impulse, making certain technologies better suited to certain applications.

Because additional batteries, solar cells, or any other power generation or storage mechanism requires additional spacecraft mass, a high efficiency system is highly desirable. This therefore contributes to the concept of specific mass

$$\alpha = \frac{M_{prop}}{P} \tag{1.7}$$

where $M_{prop}$ is the combined mass of the thruster and power supply together. The specific mass of a propulsion system is a key figure of merit to determine whether rapid transit between orbits can be achieved [3]. Equivalently to $\alpha$, we often employ its inverse, specific power, to compare electric propulsion systems. A thruster with a high specific power typically is associated with high thrust density and can thus save mass for the spacecraft.

### 1.1.3 Types of Electric Propulsion

While myriad electric thruster concepts exist which employ a wide variety of schemes to impart electrical energy into propellant, they can generally be categorized into three main groups: electrothermal, electrostatic, and electromagnetic devices.

**Electrothermal thrusters** function by imparting thermal energy to the propellant which is then converted to kinetic energy by means of pressure gradients. Some electrother-

mal schemes heat largely unionized neutral gas, while others focus on electron heating of a plasma. Key examples of the former type are resistojets and arcjets. These devices drive currents through resistors to heat the propellant flowing through the thruster, with a resistojet using a physical heater, often a wire, while an arcjet uses a sustained electrical discharge between a typically centrally-mounted cathode and an annular anode which doubles as a nozzle. The resistoject comes with the limitation that propellant temperature cannot exceed that of the heating element, which reduces maximum specific impulse to a few hundred seconds but grants high efficiencies approaching unity [4]. Arcjets avoid this limit via their contactless heating approach, achieving specific impulses up to 2000 s in exchange for lowered efficiencies peaking at about 50% [5]. Continuing this trend toward higher temperatures the magnetic nozzle acts on the hot electrons in a plasma. A radial pressure gradient induces an azimuthal diamagnetic drift on the electrons which in turn accelerates them via the Lorentz force with the radial component of the field [6, 7]. These devices are capable of specific impulses up to $\sim$2500 s depending on power level and propellant choice.

**Electrostatic thrusters** operate by accelerating the ions in a plasma via steady electric fields. The classic example of an electrostatic thruster is the Gridded Ion Thruster (GIT). As the name implies, the GIT device employs conductive grids biased to high voltages to accelerate the ions supplied by a plasma. These devices can reach very high specific impulses of up to 10,000 s in certain operating regimes [8], but tend to exhibit poor thrust density, requiring a very large device to produce enough thrust for many missions. Electrospray thrusters similarly employ grids biased to high voltages, but rather than plasma use conductive liquid propellant which coats a field of small (10s of $\mu$m) emitter needles. This avoids ionization cost and leads to very effective storage of the dense liquid propellant. Electrosprays promise high efficiency and range of specific impulses depending on propellant choice. However, electrosprays suffer from resiliency issues where electrical shorts between emitter needles and extractor grids limit thruster lifetime. Further, the small scale of the electrospray requires that many emitter/extractor pairs be employed in parallel to produce meaningful thrust, causing the odds of failure to approach unity as the number of emitters is increased [9, 10].

Finally, **electromagnetic thrusters** use electromagnetic fields to accelerate plasmas. The magnetoplasmadynamic thruster (MPD) and its cousin the applied field MPD (AF-MPD) are notable examples of steady-state electromagnetic thrusters. In these devices, a strong current (kiloAmps) flows between a centrally mounted cathode and an annular anode. This current is redirected azimuthally by the presence of an axial magnetic field (generated by the return current in the case of the self-field MPD and by external magnets for the AF-MPD) and interacts with the radial component of that field via the Lorentz force to produce

thrust. These devices can have specific impulses up to 6000 s depending on propellant choice and operating regime [11], but face lifetime limitations due to electrode wear. A wide variety of pulsed electromagnetic schemes exist such as the Pulsed Inductive Thruser (PIT) which pushes a strong pulsed current (typically 10s of kA) through a planar coil to induce an opposite current in a plasma sheet [12]. The plasma is then accelerated by the interaction of those magnetic fields with a force proportional to the square of the antenna current transient.

These categorization are not absolute and overlap exists between them. The Hall Effect Thruster (HET), for example, is often argued to be in either the electrostatic or electromagnetic category [13]. It accelerates ions via an electric field, but that field is only produced because electrons become trapped in a Hall drift by the presence of a magnetic field. The HET is currently the most flown type of electric propulsion device because of its high efficiency (up to ∼60%) as well as a specific impulse and thrust-to-power which fall within a useful regime for many propulsion applications (1500-3000 s) [14].

## 1.2 Inductive Pulsed Plasma Thrusters

In this section we present a brief review of Inductive Pulsed Plasma Thrusters (IPPTs) to help motivate our research on the RMF thruster.

### 1.2.1 Overview and Advantages

An IPPT is a propulsion system which pulses high curents through coils or antennas to inductively drive currents in a plasma via Ampere's Law and Faraday's Law:

$$\vec{\nabla} \times \vec{B} = \mu_0 \vec{j} \tag{1.8}$$

$$\vec{\nabla} \times \vec{E} = -\frac{\partial \vec{B}}{\partial t} \tag{1.9}$$

for magnetic field $\vec{B}$, electric field $\vec{E}$, and current density $\vec{j}$. In this process, the rapidly increasing current in the coil induces an equally rapidly increasing magnetic field in the region of a seed plasma via Eq. 1.8. Because the magnetic field is time-varying, a curled electric field is therefore produced via Eq. 1.9 which in turn creates plasma currents via Ohm's Law (Eq. 2.8). The plasma currents then push off the original magnetic field via a Lorentz force interaction:

$$\vec{f_L} = \vec{j} \times \vec{B} \tag{1.10}$$

where $f_L$ is a force density caused by this interaction. In this way, the current density is proportional to the rate of change of the coil current ($\vec{j} \propto \dot{I}_c$) and the magnetic field $\vec{B}$ is proportional to its magnitude ($\vec{B} \propto I_c$) allowing the force to scale quadratically with the antenna current ($F \propto I_c \dot{I}_c \approx \frac{I_c^2}{\tau}$ for current rise time $\tau$).

This force generation mechanism has three key benefits we wish to highlight. First, the quadratic force scaling with antenna current gives IPPTs very high force density and specific power. That thrust scales like $T \propto I_c^2$ implies power scales like $P \propto I_c^4$. IPPTs therefore are attractive for very high power system architectures (>100 kW) where the use of more conventional Hall thrusters or Gridded Ion thrusters would require either prohibitively large devices or the parallelization of many smaller devices, increasing system complexity. Second, the pulsed nature of the IPPT can be an advantage in and of itself as it enables power throttling through the entire thruster operating range without reducing efficiency. Varying access to electrical power on orbit can reduce the effectiveness of conventional electric propulsion systems which typically operate optimally at a certain power level.

Finally, the current generation scheme does not rely on a direct plasma discharge. No cathode and anode are required for IPPT operation, and therefore the plasma current is not limited by the current which can be extracted from a cathode. More importantly, however, we avoid the need for plasma-wetted electrodes which can wear and reduce lifetime, especially with exotic propellants. The IPPT then is naturally suited to in-situ resource utilization (ISRU) applications in which available propellant on the moon and Mars chiefly consists of carbon dioxide, water, and other non-noble species [15, 16, 17]. IPPTs would also therefore be attractive for multimode propulsion, in which two or more propulsive modes are integrated into a single spacecraft and the thruster's impact on specific power can be mitigated via shared hardware between modes [18].

### 1.2.2 Types of IPPTs

Two major categories of IPPTs can be identified. These are divided between open magnetic flux thrusters and closed magnetic flux thrusters [19].

Open magnetic flux thrusters involve inductive coils oriented in the azimuthal direction. When the high amplitude current pulse discussed above is released, the resulting plasma current will also be azimuthally oriented but will mirror the initial current pulse in direction. Thus, the thruster resembles two counter-rotating, axially symmetric current loops. Such a configuration produces a repelling force between the two current loops causing the plasma to be accelerated away. When the inductive coil forms a planar sheet, the device is known as a Pulsed Inductive Thruster (PIT). PITs are perhaps the most studied IPPT and have

achieved efficiencies of up to 60% [20]. A major challenge in the operation of a PIT is that current must be induced and impulse generated in the plasma over a very short period of time lest the plasma exit an effective coupling range for the inductive coil. The conical theta-pinch thruster (CTP-IPPT) seeks to remedy this shortcoming by employing a conical rather than planar inductive coil. Multiple cone angles have been investigated ranging from 20 to 60 degrees, with optimal performance corresponding to an intermediate angle of 38 degrees. However, efficiency was relatively low for this device, peaking at less than 6% [21].

Closed magnetic flux IPPTs differ from their open flux conterparts because the current induced in the ionized propellant is allowed to form a closed internal magnetic field structure, known as a plasmoid. The confined nature of the plasma has the potential to reduce wall losses and allow thermal energy in the plasma to be converted into kinetic energy via the Lorentz force with a diamagnetic drift current. The most studied type of closed magnetic flux IPPT involves the formation of a field reversed configuration, or FRC plasmoid. This type of thruster is similar in structure to the CTP-IPPT, but differs in that the the theta-pinch FRC involves the application of a steady bias magnetic field to aid confinement and plasmoid ejection. Much of the Lorentz force therefore does not directly arise from the inductive coil's magnetic field, but rather that of the bias. Study into this type of plasmoid formation with the goal of plasma confinement and fusion in mind goes back to the early 1960s as far as we are aware [22], and has been a topic of consistent study throughout the decades since (e.g. Refs. [23, 24, 25, 26]), with modern research being published even today [27, 28]. Several groups have studied the theta-pinch FRC thruster using various geometries including an annular variation which seeks to reduce the transient voltages required for FRC formation by forming the plasmoid in an annulus between two sets of inductive coils [29, 30, 31].

Another closed mangetic flux IPPT is the Magnetically Accelerated Plasmoid (MAP) thruster, which was investigated and developed by the University of Washington [32, 33]. The MAP thruster was a scheme to accelerate a plasmoid already formed by either RMF or theta-pinch using a peristaltic bias field. In such an architecture, the cone structure employed by the RMF thruster and corresponding radial magnetic field is eschewed in favor of a tube inside a series of coils. Current is then pulsed through these coils in series to provide temporary positive radial field just upstream of the plasmoid, forcing it forward. In this manner, the plasmoid rides a wave of magnetic pressure forward, with its axial velocity limited in principle by the phase velocity of the pulsed magnetic wave. This thruster reported per-shot impulses as high as 0.3 N-s and corresponding specific impulses of 18-20 ks when operating on deuterium. However, we note that the detailed methods and analysis used to arrive at this figure are not published as far as we are aware. However, this thruster concept has seen more attention very recently with the Magnetic Induction Plasma Engine (MIPE),

a propulsion device which closely resembles the MAP. However, the MIPE critically does not require the pre-formation of an FRC plasmoid, although it is possible the transient fields involved in the acceleration process produce a theta-pinch FRC as a side effect. The MIPE was reported to show efficiency as high as 37% with specific impulse up to 2300 s [34], making it a very attractive technology if these results can be replicated.

### 1.2.3 Challenges

While IPPTs represent a thruster architecture with several compelling benefits, they remain at a low technology level compared to state-of-the-art electric propulsion devices such as Hall thrusters. The low readiness level for these thrusters can be attributed to two primary challenges: difficulty in modeling and difficulty in design and testing.

IPPTs by nature involve highly coupled systems in nonequilibrium states. Numerical modeling, magnetohydrodynamic (MHD) in particular, has seen success for some IPPTs such as the PIT, for which models match experiment reasonably well [35, 36, 37]. However, many physical assumptions are required for these models to be effective which reduces the physical insight which might be extracted from them. Circuit modeling takes a reduced order approach by abstracting the thruster and plasma into an equivalent electrical circuit whose behavior can be described with a system of partial differential equations (e.g Refs [38, 39, 40]). However, this approach too requires significant simplifying assumptions to function. In particular the mutual inductance between the plasma and the inductive coil is a complex and time-varying quantity which involves model parameters which must be learned.

Secondly, a common theme for IPPTs is that higher pulse energies are associated with improved performance. These high energy pulses require very high transient currents and voltages which reduce the lifetimes of power switching circuitry. Steady-state switching reduces this concern somewhat but requires lower transient voltages and currents than can be achieved. Beyond the switching components, the capacitors themselves which are required to store the energy to produce these high current pulses tend to experience reduced lifetime at higher voltages [41]. Lifetime concerns owing to electrical circuit failure make a major advantage of the IPPT, lack of electrodes which can erode, moot. Taking these effects together, we see that effective IPPTs will tend to face lifetime concerns without improvements to power switching circuitry or an alternative scheme which does not require such high current and voltage transients.

## 1.3 The Rotating Magnetic Field Thruster

### 1.3.1 Thruster Overview

The canonical RMF thruster is shown in diagram form in Fig. 1.1. It consists of a conical discharge chamber which is surrounded by magnets to apply a steady bias magnetic field which approximately conforms to the thruster walls. Neutral gas and a seed plasma are allowed to flow into the cone from a variety of injection and pre-ionization schemes. The RMF itself is generated by set of antennas, each of which takes the form of a Helmholtz pair oriented transverse to the thruster axis and at an angle with its fellows. By driving an oscillating current through each antenna, phase offset by the same angle as the physical orientation, a rotating magnetic field is produced. The RMF can be generated by any number of antennas so long as their fields superpose correctly. The RMFv2 thruster, for example, uses a two-phase system in which the antennas are orthogonally oriented, while the RMFv3 thruster employs a three-phase architecture where the antennas are 120 degrees separated. This scheme is inspired by the operation of an induction motor, where the rotor has been replaced by a plasma volume.

The rotating magnetic field entrains seed electrons which produce an azimuthal current as they are dragged along with the rotating field. This current causes further ionization of the background neutral gas. The resulting azimuthal currents can interact via the Lorentz force with the radial component of the bias magnetic field to produce thrust, and with the axial component of the bias field to provide plasma confinement from the walls. When operated in pulsed-mode, this results in the creation of a field reversed configuration (FRC) plasmoid, a type of plasma confinement technique. In addition, the rapid onset of plasma current can couple inductively to nearby conductive structural elements in the thruster body, which in turn produce magnetic fields that can provide a source of Lorentz interaction and additional confinement. Indeed, in the fusion community—where the RMF scheme is used for plasma confinement—the conductance of such elements, which are often referred to as flux conservers, is an important figure of merit [42]. In this work, we refer to this transient magnetic field and thrust mechanism as the 'structure' force, as it requires the plasma to couple to conductive thruster structural elements.

When operated in pulsed-mode, the RMF thruster may be considered a member of a family of devices known as inductive pulsed plasma thrusters (IPPTs) discussed above. The RMF thruster shares many of its potential strengths with other in-family devices such as the Pulsed Inductive Thruster (PIT) [43, 44], the conical theta-pinch thruster [45], and the Faraday Accelerator with Radio-frequency Assisted Discharge (FARAD) thruster [46]. These include high throttlability while maintaining efficiency and specific impulse, high specific

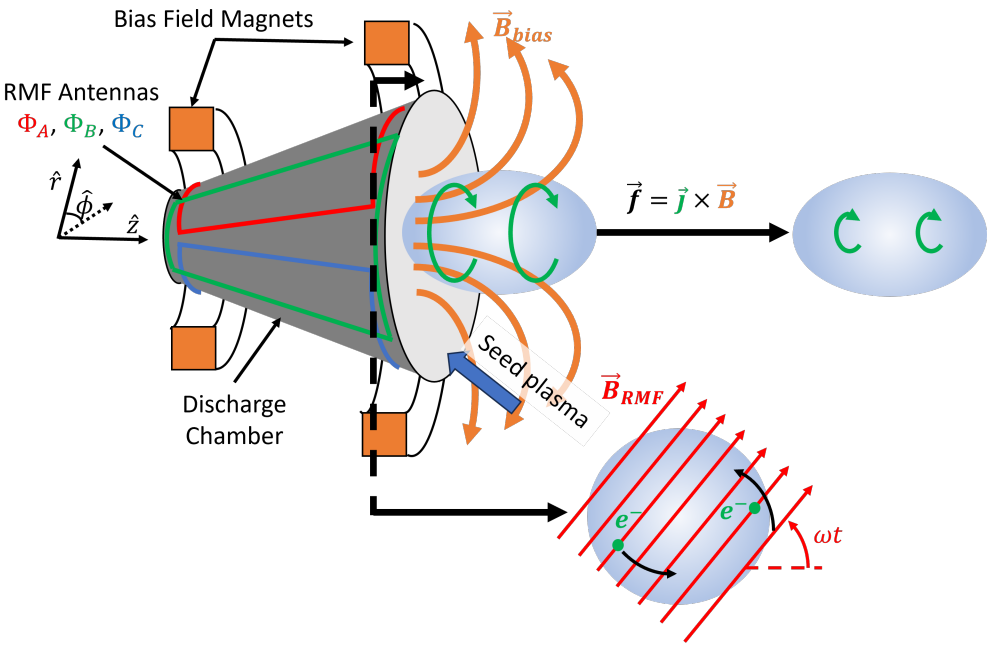


Figure 1.1: Canonical geometry of an RMF thruster, in this case employing a three-phase RMF antenna.

power, and in-situ resource utilization (ISRU) compatibility. The high specific power of these devices stems primarily from quadratic thrust scaling with induced azimuthal plasma current ($T \propto I_\phi^2$) which is provided by fields generated by transient, secondary induced currents in the thruster body in the case of the RMF. However, the RMF current drive scheme differs critically from these other devices in how it induces the plasma currents which produce the Lorentz force for acceleration. Instead of employing a scheme by which the plasma current depends on the amplitude of the magnetic field produced by externally mounted antennas, the ideal RMF current drive only depends on the frequency of the applied rotating field. This in principle allows the RMF thruster to avoid the high current and voltage transients (e.g. 30 kV and 100 kA for the PIT Mk V [35]) which make power supply design challenging for other IPPTs.

Alternatively, the RMF thruster scheme can be operated in the continuous wave (CW)-mode, which corresponds to 100% duty cycle. In this mode, the RMF thruster instead resembles an applied field magnetoplasmadynamic thruster (AF-MPD). These devices exhibit high thrust density and power scaling [47, 48] and have been highlighted as potential baseline technology for nuclear electric propulsion powered missions to Mars by the 2030s [49]. With that said, the roadmap and NASA report also highlight several technical challenges with MPDs that must be resolved. Chief among these are limitations related to lifetime/efficiency. MPDs traditionally undergo substantial erosion and efficiency loss due

to ion and electron transport to the plasma-wetted surfaces. The RMF thruster, however, has no need for plasma-wetted electrodes due to its alternative current generation scheme. Taken together, we see that RMF technology has the potential to solve major challenges for its more traditional analogues in both the pulsed-mode and the CW-mode architectures.

The RMF thruster bears much resemblance to the theta-pinch FRC thrusters discussed in the previous section. Those thrusters were successful in current drive and plasmoid formation and were able to achieve impulse estimates in some cases. However we see the theta-pinch FRC as less suited to space propulsion applications than the RMF. While the end result of each current drive scheme is similar, the key differentiating factor is how the plasma current scales with antenna current. As mentioned above, the theta-pinch current is proportional to the rate of change of the transient current in the antenna, which in turn makes it proportional to the voltage which can be applied across that same antenna. The need for higher plasma currents therefore would drive designs to prohibitively high voltages, making power supply design challenging. It is precisely this need for very high voltages and current transients which the RMF thruster seeks to remedy while maintaining effective current drive.

### 1.3.2 Technology Origins and Past Efforts

Fundamentally, the RMF thruster is just one technology which involves inductively driving azimuthal currents in a cylindrically confined plasma, the study of which goes back at least six decades and involves a rich history of research. It will not be possible to do justice to a full review of these works within the format of this dissertation. However, we present here a brief overview of those works most germane to our research.

The rotating magnetic field current drive scheme was first proposed by Blevin and Thonemann of Culham Laboratory in 1962 [50]. This work sought to employ the RMF to produce what later became known as a field-reversed configuration (FRC) plasmoid. The main goal of such a scheme is to provide plasma confinement using the (purely axial) bias magnetic field against the induced current which naturally seeks to expand outward. Blevin and Thonemann provide a self-consistent analytic model for the current drive mechanism and the electron density distribution. This work was expanded upon by Jones and Hugrass [51] who provided additional insight into the current generation scheme by identifying limitations on RMF strength required to fully penetrate the plasma. The FRX experiment at Los Alamos National Laboratory introduced the concept of a translating FRC plasmoid with the goal of applying adiabatic compression to increase plasma temperature and density toward fusion [52]. This plasmoid translation research helped to inspire the RMF thruster in its current form. We note as well that FRC translation and adiabatic compression toward the

goal of fusion is still an area of active research at the time of writing, with private organizations such as Helion Energy focusing on this technique. The first device of which we are aware which employs an RMF scheme to intentionally produce thrust was the Star Thrust Experiment (STX) from the University of Washington [53]. The STX sought to employ the RMF as a confinement heating scheme to feed a hot dense plasma into a magnetic nozzle.

First among the studies which focused on a thruster closely resembling the devices presented in this dissertation was the work by MSNW, LLC and the University of Washington with their Electrodeless Lorentz Force (ELF) thruster in 2009. However, the group at UW was studying RMF FRC operation as early as 2000 [54]. This RMF-based thruster was operated with nitrogen, air, oxygen, and xenon propellants in burst operation, i.e. with a limited number of consecutive pulses. Each pulse delivered between 10 and 70 Joules with an RMF frequency of 300 kHz. [55]. Because the burst operation precluded standard thrust stand measurement and the thruster itself was integrated mechanically with the vacuum chamber [56], performance could only be measured indirectly with a calibrated ballistic pendulum. The resulting per-shot impulse was used to infer thrust efficiency of up to $\sim 8\%$ [57] although this number does not include mass utilization, divergence effects, or losses associated with coupling power to the plasma. This group also performed path-finding demonstrations to show the thruster was capable of ISRU capability by testing with exotic propellants [58]. This work was identified by the Air Force Research Laboratory as a promising technology to compete with the PIT thruster [59].

More recently, the Furukawa group at the Tokyo University of Agriculture and Technology has developed a test unit and performed electrical and plasma-based measurements. In lieu of burst mode operation, Furukawa et al. operated their device with continuous pulsing, thus enabling time-averaged measurements of performance. Indirect measurements with a ballistic pendulum yielded thrust peaking at $\sim$7 mN for 3 kW operation at 60 sccm argon propellant flow rate and an RMF frequency of 700 kHz [60, 61]. Based on these reported values, we can infer a total efficiency of $\sim$0.5%. This group also performed experiments to measure the azimuthal current generated by their device as we do in Chapters 6 and 8, but found the currents driven to be only single percentages of what might be anticipated by applying the Blevin and Thonemann current drive of Eqs. 2.25 and 2.26 [62]. Future investigation on an updated device revealed improved current drive but only partial penetration of the RMF, leading to phase delay of the rotating field with radius. Further, much of the current driven was determined to be due to the diamagnetic drift rather than directly caused by electron entrainement in the rotating field [63].

One common method to understand the behavior of these pulsed systems is circuit modelling, in which the device is simplified into a reduced-order circuit model. This approach

has been successful for related technologies in the past [64, 65, 66, 67, 68]. In 2018, the University of Michigan constructed the PEPL RMFv1 thruster which operated up to 1.1 kW using circuit modelling to arrive at this design [69, 70]. However, performance measurements on this device showed null thrust generation [1]. With this said, future circuit modelling work by the University of Michigan showed improved agreement with experiment when modeling the RMF antenna/plasma relationship using gyrator terms rather than traditional induction [71, 72], indicating that a typical circuit approach may not be applicable to the RMF thruster as it is to other 'direct-drive' devices in which plasma current is directly proportional to antenna current transient. Taken together, these low efficiency results suggest either that the RMF thruster scheme is ineffective as a thrust device, or that there is fundamental misunderstanding in the field for how these devices operate and should be built. The work presented in this dissertation seeks to address this question and provide a route for future work to uncover enhanced performance.

## 1.4 Objectives

In light of the potential advantages of the RMF thruster over more conventional propulsion techniques, as well as the poor performance estimates that have been made, there is a pressing need for a better understanding of RMF thruster behavior. In particular, we note that the established model for current drive (which will be discussed in Sec. 2.3.2) does not provide significant performance limitations for the RMF thruster. Given that, the primary goal of this work was to improve the understanding of the performance and behavior of the RMF thruster from the perspective of RMF current drive and Lorentz force. A working test unit must be developed and characterized so that experiments to address unknown physics can be performed. That done, lessons learned can be applied to updated designs as both a means of improving thruster efficiency and testing physical hypotheses. With all this in mind, the objectives for this work are as follows:

1. Develop a working RMF thruster and perform baseline performance characterization
2. Use probing techniques to understand the major loss mechanisms in that device
3. Iterate the thruster design and characterization process to apply new knowledge of thruster behavior
4. Develop an updated current drive model to explain thruster behavior and validate it against experiment

## 1.5 Organization

Chapter 1 serves to provide a brief general introduction to electric propulsion to help provide context for this work as a whole. The RMF thruster operating theory is presented in detail in Chapter 2. This includes a discussion of our updated current drive model and how it differs from the established theory. In Chapter 3 and Chapter 4 we detail the experimental techniques used to make meaningful measurements of the RMF thruster performance and behavior, focusing on the physical apparatus and analysis techniques respectively. This work seeks not only to present the contributions listed in the preceding section, but to provide context for them by discussing the motivation for the design of each thruster and the experiments performed. Therefore Chapters 5 through 8, which represent the heart of this work, are presented in the chronological order in which they occurred. Chapter 5 discusses the design and initial baseline testing for the RMFv2 which exhibited poor performance. The question of why performance was low is then addressed using plasma probing techniques in Chapter 6. This structure is paralleled in Chapter 7 which discusses the design and performance measurements for the RMFv3 thruster and Chapter 8 which explains those performance measurements using probing to place the thruster behavior in the context of RMF current drive theory. Finally, we conclude with a discussion of how future research might be directed in Chapter 9.

# CHAPTER 2

# Theory for RMF Thruster Operation

## 2.1 Introduction

The theory for RMF current drive has, to our knowledge, gone largely unchallenged since its initial derivation by Blevin and Thonemann in 1962. Indeed, the established current drive model was invoked in the design of every RMF thruster of which we are aware [1, 57, 62]. In light of recent data acquired on the RFMv3 thruster which we present in Chapter 7, however, we present a revised version which relaxes certain assumptions to better capture the physics involved

## 2.2 Relevant Plasma Phenomenon

While this work is not intended as an introductory text on plasma dynamics (see e.g. Ref. [73] for that) we briefly introduce here some critical phenomenon relevant to the experiments and thrusters discussed later on. Rather than re-derive these concepts in later chapters we will refer to them here.

The plasma discussed in this dissertation can be thought of as composed of three distinct gas populations superposed over each other: neutral atoms, negatively charged electrons, and positively charged ions. Because the electrons and ions are attracted to either other, they tend to oscillate at the plasma frequency

$$\omega_p = \sqrt{\frac{e^2 n_e}{\epsilon_0 m_e}} \tag{2.1}$$

for electron charge $e$, density $n_e$, and mass $m_e$, and with $\epsilon_0$ as the permittivity of free space. Any disturbances to the plasma on a timescale slower than the plasma frequency, which is typically in the GHz range for the thrusters considered here, do not result in a net charge

imbalance in the plasma. Instead the plasma is considered largely quasi-neutral, as a so-called ambipolar electric field is developed which accelerates the two charged species together. We can therefore apply force to one species and expect the other to follow, resulting in an accelerated net-neutral gas.

As a general rule of thumb, electrons tend to resist crossing magnetic field lines. This is because the Lorentz force causes charged particles to orbit field lines at the cyclotron frequency

$$\omega_{ce} = \frac{eB}{m_e} \tag{2.2}$$

where $B$ is the magnetic field present. However, mechanisms which change the energy of the electrons such as collisions can allow the electrons to cross field lines. The degree of confinement is often discussed in terms of the Hall parameter

$$\Omega = \frac{\omega_{ce}}{\nu}. \tag{2.3}$$

where $\nu$ refers to the electron-heavy collision frequency. $\Omega/gg1$ implies electrons are strongly tied to magnetic field lines, while the reverse implies a low degree of confinement. While ions experience the same phenomenon, their increased mass ($M_i \approx 10^6 m_e$ for the xenon plasma used in this work) would require a commensurately higher magnetic field to be confined.

For the calculations in this work, we use the expressions for $\nu = \nu_{ei} + \nu_{en}$ (the contributions from election-ion collisions and electron-neutral collisions) for xenon from Ref. [74]:

$$\nu_{en} = \sigma_{en} n_n \sqrt{\frac{8eT_{eV}}{\pi m_e}} \tag{2.4}$$

$$\nu_{ei} = 2.9 \times 10^{-12} \frac{n_e \ln \Lambda}{T_{eV}^{\frac{3}{2}}} \tag{2.5}$$

for electron temperature $T_{eV}$ is in electron-volts and where the coulomb logarithm is

$$\ln \Lambda = 23 - \frac{1}{2} \ln \left( \frac{10^{-6} n_e}{T_{eV}^3} \right) \tag{2.6}$$

and the electron-neutral collision cross section is given by

$$\sigma_{en} = 6.6 \times 10^{-19} \left[ \frac{\frac{T_{eV}}{4} - 0.1}{1 + \left(\frac{T_{eV}}{4}\right)^{1.6}} \right] \tag{2.7}$$

.

We finally introduce Ohm's law, which describes the motion of massless electrons in a plasma in which the ions are not magnetized:

$$0 = \vec{E} + \vec{v} \times \vec{B} + \frac{m_e \nu}{e} \vec{v} + \frac{1}{n_e} \vec{\nabla} \left( n_e T_{eV} \right) \tag{2.8}$$

The small electron mass causes them to experience no net acceleration in this formulation because of their necessarily fast response to applied force. Therefore, this equation can be used to compute electron drifts. In particular, this equation will be invoked to describe the RMF current drive mechanism.

## 2.3 RMF Current Drive

We first present our theory for the RMF current drive mechanism which we will see in Chapter 8 explains observed thruster behavior and matches experimental measurement of current density before contrasting with the established theory. Both are derived in fundamentally similar manners with our updated model relaxing several key assumptions.

To anchor this analysis, we refer back to Fig. 1.1 which shows a diagram of an RMF thruster with the cylindrical coordinate system marked. We first consider the RMF in cylindrical coordinates $(r, \phi, z)$:

$$B_{\omega,r} = B_\omega \cos\left(\omega t - \phi\right) \tag{2.9}$$

$$B_{\omega,\phi} = B_\omega \sin\left(\omega t - \phi\right) \tag{2.10}$$

where $B_\omega$ is the RMF amplitude, $\omega$ is the RMF frequency, $t$ is time, and $\phi$ is the azimuthal coordinate. By Faraday's Law, a time-varying magnetic field gives rise to a curled electric field. This results in the axial electric field

$$\vec{E}_{\omega,z} = -r\omega B_\omega \cos\left(\omega t - \phi\right) \tag{2.11}$$

where $E_\omega$ is the electric field directly resulting from the RMF. To determine electron currents, we leverage Ohm's law for electrons assuming stationary unmagnetized ions (Eq. 2.8). Fundamentally, current density arises from a combination of electron density and drift speed

$$j_\phi = n_e v_\phi \tag{2.12}$$

for density $n_e$ and drift speed $v_\phi$. To arrive at the plasma azimuthal current density therefore we must calculate both the electron azimuthal drift speed $v_\phi$ and density $n_e$ as a function of

time and position.

### 2.3.1 Updated Model

We first derive our expression for azimuthal drift velocity. We make the following assumptions regarding plasma behavior:

- Electrons may drift in any direction in the thruster
- Electron temperature is uniform throughout the plasma
- Electron pressure gradients may exist in the radial direction only
- Ions are unmagnetized and stationary on the timescales considered
- The bias field $\vec{B}_0$ may have components in the $\hat{r}$ direction and $\hat{z}$ direction
- We cannot explicitly calculate the self-induced field $\vec{B}_{self}$ which is generated by the plasma currents. Instead we must take it as an input parameter which, like the bias field, may have components in the $\hat{r}$ direction in addition to the $\hat{z}$ direction

Therefore the full magnetic field may be written as

$$\vec{B} = \left(B_{0,r} + B_{self,r} + B_\omega \cos\left(\omega t - \phi\right)\right)\hat{r} + B_\omega \sin\left(\omega t - \phi\right)\hat{\phi} + \left(B_{0,z} + B_{self,z}\right)\hat{z} \tag{2.13}$$

and Ohm's Law under these assumptions appears as

$$v_\phi B_z - v_z B_\phi + \frac{\nu m_e}{e} v_r + \frac{1}{e n_e}\frac{\partial P}{\partial r} = 0 \tag{2.14}$$

$$v_z B_r - v_r B_z + \frac{\nu m_e}{e} v_\phi = 0 \tag{2.15}$$

$$E_z + v_r B_\phi - v_\phi B_r + \frac{\nu m_e}{e} v_z = 0. \tag{2.16}$$

Solving this system of equations for drift velocity, we find the result for $v_\phi$

$$v_\phi = \frac{-E_z\left(B_r - \frac{eB_\phi B_z}{\nu m_e}\right) + \frac{1}{e n_e}\frac{\partial P}{\partial r}\left(B_z + \frac{eB_\phi B_r}{\nu m_e}\right)}{|B|^2\left(1 + \left(\frac{\nu m_e}{e|B|}\right)^2\right)} \tag{2.17}$$

where $|B| = \sqrt{B_r^2 + B_\phi^2 + B_z^2}$ is the magnitude of the combined magnetic field from all sources. We note that the expression for $v_\phi$ in Eq. 2.17 is a function of all three dimensions. A phase-averaged $v_\phi$ is not convenient to write analytically for arbitrary values of the

parameters considered due to the proliferation of trigonometric functions throughout the expression.

To determine the radial density profile, we make the following additional assumptions:

- Plasma density is dictated by assuming a total number of electrons per axial slice of the thruster $N_0 = 2\pi \int_0^{R(z)} n(r) r dr$ where $R$ is the thruster radius
- Electrons are fully tied to the RMF and bias fields ($B_\omega, B_z/gg\sqrt{2}\frac{e}{\nu m}$)

This reduces Eq. 2.14 to

$$en_e \left(v_\phi B_z - v_z B_\phi\right) + \frac{\partial P}{\partial r} = 0. \tag{2.18}$$

We then recognize the first two terms as the radial component of $\vec{j} \times \vec{B}$ and neglect magnetic tension, which is valid in the limit that $\omega << \frac{1}{\tau_A}$ where $\tau_A$ is the Alfven time (in the case of our thrusters, $\frac{1}{\tau_A} \approx 1 \times 10^6 Hz$ and $\omega \approx 1 \times 10^5$ Hz). Under this condition, Eq. 2.18 is equivalent to magnetic pressure balanced against thermal pressure:

$$\vec{\nabla} \left(\frac{B^2}{2\mu_0}\right)_r = -\vec{\nabla} P_r, \tag{2.19}$$

which has the solution

$$n(r) = n_0 + \frac{B^2(0) - B^2(r)}{2\mu_0 e T_{eV}} \tag{2.20}$$

for

$$n_0 = \frac{N_0}{\pi R^2} + \frac{1}{\mu_0 e T_{eV} R^2} \int_0^R \left(B^2(r) - B^2(0)\right) r dr. \tag{2.21}$$

This expression for $n(r)$ suggests that we will see electron densities radially peaked at the location of lowest total magnetic field. In the event of FRC formation, the bias magnetic field will be reversed by the induced current close to centerline but enhanced close to the thruster wall. We can therefore anticipate high electron density in an annulus about the axis of the thruster. In the event that the driven current reverses the axial magnetic field at all radial locations (such as for very low or no bias field strength), we do not expect this model to hold as the electrons will rapidly move to and contact with the thruster walls. Such behavior would lead to enhanced recombination at the thruster walls and loss of ionization.

Applying the same assumptions required to determine electron density to Eq. 2.17 yields

the expression

$$v_\phi = \frac{-E_z B_r}{|B|^2} + \frac{\nabla P_r B_z}{e n_e |B|^2}. \tag{2.22}$$

Eq. 2.22 provides critical physical insight into the mechanism behind the current drive interaction. Two sources contribute to the azimuthal drift. First, an ExB drift results from the axial electric field caused by the RMF and the radial magnetic field resulting from the superposition of the bias, induced, and rotating fields. Second, we see a diamagnetic drift caused by electron heating which should be expected given that this diamagnetic drift is leveraged as the main thrust generation mechanism in other RF thrusters. In addition, we see that increasing the non-RMF magnetic fields serves to retard both these drifts. Crucially, this behavior is not represented in the previously established current drive theory and explains the experimentally observed thruster behavior in Chapters 7 and 8.

We can examine the effect of the bias field to retard electron motion with Fig. 2.1, which shows a plot of the electron slip as a function of the RMF to bias field ratio discounting the diamagnetic drift term from Eq. 2.22. Slip is a concept borrowed from the design of induction motors to describe the relative speeds of the rotor and the field generated by the stator, defined as

$$s = 1 - \frac{\omega_e}{\omega} \tag{2.23}$$

where we use $\omega_e$ to refer to the actual electron angular speed while $\omega$ refers to the field's rotational angular velocity. We arrive at the expression required to produce Fig. 2.1 by substituting in values for $E_z$, $B_r$, and $|B|$ from Eqns. 2.11 and 2.13 and divide the result by $r$ to calculate $\omega_e$. To more easily examine physical limits, we also ignore contributions from the self-field. To collapse this expression into the ratio of field strengths, we assign a bias field angle $\theta_B$ such that $B_{0,r} = B_0 \sin(\theta_B)$ and $B_{0,z} = B_0 \cos(\theta_B)$

$$s = 1 - \frac{\frac{B_\omega}{B_0 \sin(\theta_B)} \cos(\omega t - \phi) + \left(\frac{B_\omega}{B_0 \sin(\theta_B)}\right)^2 \cos^2(\omega t - \phi)}{1 + \cot^2(\theta_B) + \left(\frac{B_\omega}{B_0 \sin(\theta_B)}\right)^2 + 2\frac{B_\omega}{B_0 \sin(\theta_B)} \cos(\omega t - \phi)} \tag{2.24}$$

Because Fig. 2.1 discounts the diamagnetic drift and self-field, it only truly applies at the very beginning of current drive before significant ionization and plasma currents make these effects significant. However, it clearly shows how an RMF which is too weak—even in the limit of zero plasma resistivity—cannot produce an effective plasma current in the presence of a bias field. Significantly, we note that because we have ignored the effect of self-field, we

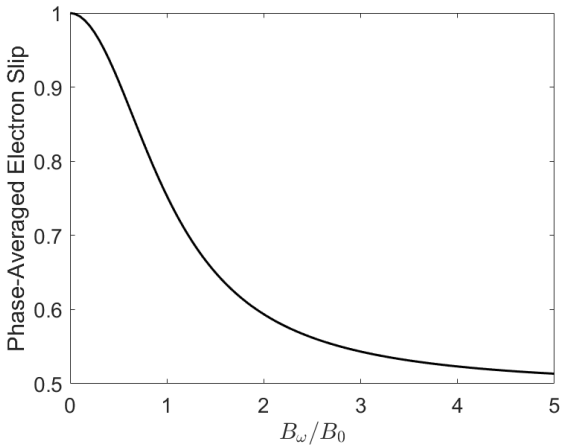


Figure 2.1: Phase averaged electron slip for a bias field angle of 17 degrees, discounting diamagnetic drift and the self-field

do not expect based on Fig. 2.1 that the RMF must be five times as strong as the bias field to produce plasma current in the steady-state. If enough current can be driven at start-up, the self-field generated by the plasma current will serve to effectively weaken the bias field creating a region where the static fields cancel in which the RMF can be effective. We can therefore draw the conclusion that FRC formation is necessary for effective RMF current drive.

### 2.3.2 Established Model

The current drive model culminating in Eqs. 2.20 and 2.22 was developed in response to experimental data gathered on the RMFv3 thruster which could not be explained by the previous current drive model, developed by Blevin and Thonemann. This phenomenon will be discussed in detail in Chapter 8. Significantly, this theory was used in the development of every RMF thruster we are aware of. The earlier theory has the distinct advantage that it is analytic, predictive, and self-consistent, while our model does not attempt to self-consistently predict the induced magnetic field. Because the induced magnetic field is of similar strength as the bias field, experimental measurement is required to apply our theory. This makes it useful for intuitive understanding, but not for direct application to thruster design.

We follow a similar route as previously to arrive at expressions for azimthal drift velocity and electron density. However, we are able to phase-average the velocity over an RMF cycle due to the simpler expression, and the resulting differential equation for the density is

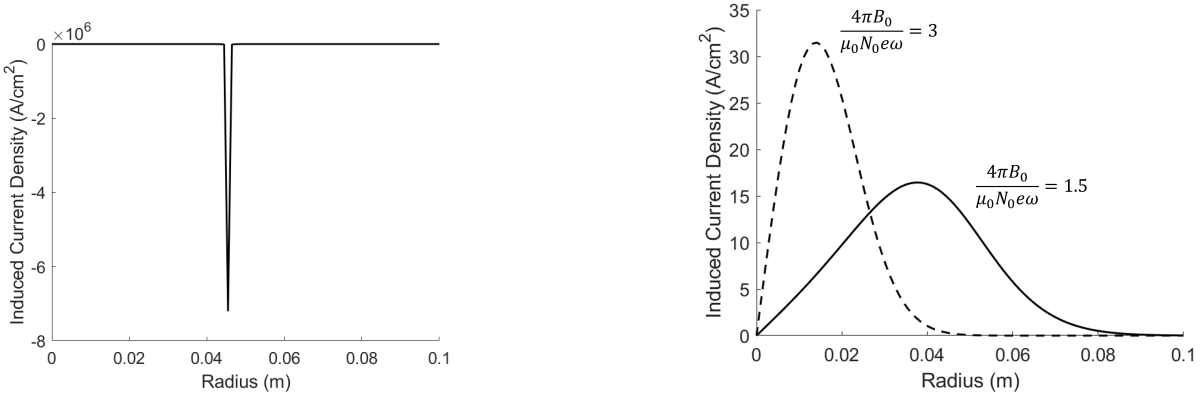


Figure 2.2: Plots of plasma current density with radius for various values of the confinement parameter a) $\frac{4\pi B_0}{\mu_0 N_0 e\omega} = 0.5$, and b) $\frac{4\pi B_0}{\mu_0 N_0 e\omega} = 1.5$ and 3. Analysis assumes electron temperature $T_{eV} = 8$ and linear electron density $N_0 = 1 \times 10^{17}$ 1/m, along with RMF frequency $\omega = 2.6 \times 10^6$ rad/s.

explicitly solvable:

$$\langle v_{\phi,BT} \rangle = \frac{-\omega r}{1 + 2\left(\frac{\nu m_e}{eB_\omega}\right)^2} \approx -\omega r. \tag{2.25}$$

$$n_{BT} = \frac{2B_0^2}{\mu_0 e T_{eV}} \frac{\left(\frac{4\pi B_0}{\mu_0 N_0 e\omega} - 1\right) \exp\left(\frac{B_0 \omega r^2}{2T_{eV}}\right)}{\left[1 + \left(\frac{4\pi B_0}{\mu_0 N_0 e\omega} - 1\right) \exp\left(\frac{B_0 \omega r^2}{2T_{eV}}\right)\right]^2} \tag{2.26}$$

We have placed brackets around $v_{\phi,BT}$ to denote that is is averaged over an RMF period. Similar to before, the expression for $n$ can only be achieved with the assumption of strongly magnetized electrons to the RMF. Unlike in Eq. 2.22, however, this results in synchronous rotation with the RMF so long as $2\left(\frac{\nu m_e}{eB_\omega}\right)^2 << 1$.

Eq. 2.26 introduces the key confinement parameter $\frac{4\pi B_0}{\mu_0 N_0 e\omega}$ which determines whether FRC formation occurs under these assumptions. Of specific relevance to this study is the situation in which $\frac{4\pi B_0}{\mu_0 N_0 e\omega} < 1$, where this theory predicts that the reversed field will be greater than the bias field even as $r$ approaches infinity, resulting in a nonphysical negative electron density everywhere. For $1 < \frac{4\pi B_0}{\mu_0 N_0 e\omega} < 2$ plasma confinement occurs and an FRC plasmoid forms, and for $\frac{4\pi B_0}{\mu_0 N_0 e\omega} > 2$ the induced field is not strong enough to reverse the bias field, resulting in electron density being confined to the axis. This effect is illustrated in Fig. 2.2. We see that when $\frac{4\pi B_0}{\mu_0 N_0 e\omega} < 1$ current is near zero everywhere but at one location when it spikes nonphysically negative. As this parameter is increased we see more physical depictions of

the current density. As we reach the regime of $\frac{4\pi B_0}{\mu_0 N_0 e\omega} > 2$, the current density must increase as the plasma becomes denser and more localized.

### 2.3.3 Field Penetration

It was later theorized that the Blevin and Thonemann model is valid only in the limit that surface currents in the plasma cannot effectively screen out the rotating field. The additional requirement was proposed by Jones and Hugrass in 1981 [75] that

$$\left(\frac{\nu}{\omega_{ce}}\right)^2 \left(\frac{R}{\delta}\right)^2 << 1, \tag{2.27}$$

is satisfied, where $\omega_{ce} = \frac{eB_\omega}{m_e}$ refers to the electron cyclotron frequency with the RMF, $R$ is the radius of the plasma column, and $\delta = \sqrt{\frac{2\nu_{ei} m_e}{\mu_0 e^2 n_e \omega}}$ is the classical skin depth of a highly ionized plasma. We have ensured in the designs of both the RMFv2 and RMFv3 thrusters that this requirement is satisfied, as will be addressed directly in Chapters 5 and 7.

### 2.3.4 Model Comparison

The updated model incorporates critical physics not included in the established theory which help to explain thruster behavior. Three critical phenomena arise from Eq. 2.22 which Eq. 2.25 does not explain. First, the presence of $|B|^2$ in the denominator of Eq. 2.22 provides a means by which an enhanced bias field can retard azimuthal electron motion. As will be discussed in Chapters 7 and 8 this effect is shown experimentally to be the case for the RMFv3 thruster and is likely significant for the RMFv2 thruster as well. Second, the new theory explicitly accounts for the diamagnetic drift. Given that the diamagnetic drift is the key thrust generation mechanism for other devices with similarly shaped magnetic fields, it is surprising in retrospect that the established model has no means to reproduce that current.

The final major differentiating factor between the two models becomes clear when we examine the limit that the rotating field is much stronger than any other fields present (i.e. $B_\omega / gg B_{0,r}, B_{0,z}, B_{self,r}, B_{self,z}$). By making this assumption, Eq. 2.25 simplifies to

$$v_\phi = \frac{\omega r B_\omega^2 \cos^2(\omega t - \phi)}{B_\omega^2 \left(\cos^2(\omega t - \phi) + \sin^2(\omega t - \phi)\right)} + \frac{\nabla P_r B_z}{B_\omega^2 \left(\cos^2(\omega t - \phi) + \sin^2(\omega t - \phi)\right)}. \tag{2.28}$$

Because $\sin^2(x) + \cos^2(x)$ is identically 1, Eq. 2.28 simplifies to

$$v_\phi = \omega r \cos^2(\omega t - \phi) \tag{2.29}$$

$$\langle v_\phi \rangle = \frac{1}{2}\omega r \tag{2.30}$$

This result is crucial as it shows clear disagreement with the established theory. Eq. 2.29 describes a situation depicted as a cartoon in Fig. 2.3. Electrons which are physically oriented at the angle $\phi = \omega t$ are fully entrained by the RMF and experience synchronous rotation, while any electrons not located at that angle experienced reduced velocity with a minimum of zero at $\phi = \omega t \pm \frac{\pi}{2}$. This implies that electrons will be 'picked up' by the RMF as it passes through the angle $\phi = \omega t$. In the limit of an entirely collisionless plasma, this would result in an azimuthal density distribution resembling a delta function centered at $\phi = \pm\omega t$. In reality, pressure effects and collisionality would cause electrons to eventually lag behind the RMF before they are picked up again at the next half-period.

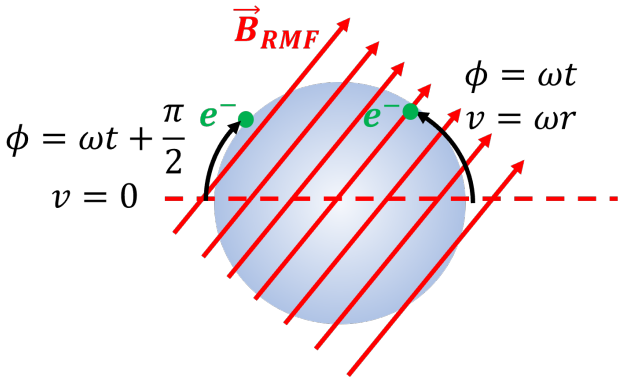


Figure 2.3: In the updated model, only electrons oriented at the angle $\phi = \omega t$ experience a drift at the full RMF angular velocity

## 2.4 Force Generation

As the goal of this device is to produce thrust, we briefly discuss here the thrust generation mechanisms which we identify in this device. These are broken down between Lorentz acceleration and non-Lorentz acceleration, which is due to electron pressure at the thruster wall:

$$F = F_W + F_L, \tag{2.31}$$

where $F_W$ is wall pressure force and $F_L$ is force caused by Lorentz effects. We discuss here the axial forces only as these will deliver net acceleration to the plasma. The wall pressure force is given by

$$F_W = \int_{A_W} en_e T_{eV} \cos(\theta_c) dA_W. \tag{2.32}$$

where $\theta_c$ is the local angle that the thruster wall normal vector makes with the axis and we integrate this surface force over the area of the thruster wall $A_W$. Meanwhile, the Lorentz-based force is given by

$$F_L = \int_{A_c} j_\phi B_r - j_r B_\phi dA_c \tag{2.33}$$

$$= \int_{A_c} (j_\omega + j_D)(B_{0,r} + B_{s,r})\, dA_c \tag{2.34}$$

where we split the azimuthal current $j_\phi$ into constituent pieces $j_\omega$ which is caused directly by the RMF and $j_D$ which is caused by the diamagnetic drift and integrate the resulting force density throughout the cross section of the thruster $A_c$. The diamagnetic drift current is explicitly predicted by Eq. 2.22 for our updated current drive model, but not in the Blevin and Thonemann formulation of Eq. 2.25. Meanwhile the radial magnetic field is decomposed into the bias field $B_{0,r}$ and the structure field $B_{s,r}$ which is caused by transient currents induced in nearby conductive structural elements of the thruster by the rapid onset of plasma currents. While the field directly induced by the plasma $B_{self}$ does interact with the plasma, it produces no net force as is shown experimentally in Ref [76]. This can be understood by considering that conservation of momentum dictates that the center of mass of a system of particles cannot accelerate without some outside influence. It is also experimentally shown in Chpt. 6 that the net force due to this field is zero at all times, though locally can be nonzero.

## 2.5 Performance Model

It can be shown that the overall electrical efficiency of the RMF thruster can be decomposed into four primary components:

$$\eta = \eta_d \eta_m \eta_c \eta_p \tag{2.35}$$

where $\eta_d$ refers to the divergence efficiency, $\eta_m$ is the mass utilization efficiency, $\eta_c$ is the coupling efficiency, and $\eta_p$ is the plasma efficiency. These terms are discussed in detail and

their values tabulated for the RMFv2 thruster in Ref. [77]. However, we will briefly define them here to provide insight into the design of the thrusters employed in this work. The efficiency contributions are calculated as follows:

$$\eta_d = \left(\frac{T}{T_{beam}}\right)^2 = \cos^2(\Theta) \tag{2.36}$$

$$\eta_m = \frac{\dot{m}_i}{\dot{m}} \tag{2.37}$$

$$\eta_c = \frac{P_p}{P} \tag{2.38}$$

$$\eta_p = \frac{T_{beam}^2}{2\dot{m}_i P_p} \tag{2.39}$$

where $T$ is the axial force imparted on the plasma, $T_{beam}$ is the total momentum flux in the ion beam spherically leaving the thruster, $\dot{m}_i$ is ion mass flow rate out of the thruster, and $P_p$ is the power successfully coupled into the plasma.

Divergence efficiency $\eta_d$ arises due to energy spent accelerating propellant in the radial direction which does not serve to generate useful impulse. The more collimated the beam, the higher this term. It is thought to primarily depend on the bias field. In particular, a more divergent field may serve to allow electrons to expand outward more readily. Mass utilization efficiency $\eta_m$ refers to the fraction of neutral particles which are successfully ionized, as unionized propellant cannot be accelerated via electric and magnetic fields. The degree of ionization, and thus the value of this term, is thought to be a consequence primarily of RMF amplitude and propellant flow rate (and therefore density). The same parameters, along with pulse length in the case of pulsed-mode operation, also impact the coupling efficiency $\eta_c$, which describes the fraction of total supplied power which is transmferred into the propellant. Finally, the plasma efficiency $\eta_p$ describes how well that coupled energy is converted into thrust, rather than being wasted on e.g. thermal losses.

Introducing this performance model allows us to intuitively identify four primary operating parameters by which we can increase device efficiency. First, a higher magnetic field strength may serve to reduce plasma wall losses by increasing plasma confinement as well as provide a stronger radial magnetic field for the azimuthal electron drift described in Eqs. 2.20 and 2.22 to react with via the Lorentz force. Second, reducing density will also translate into lower wall losses as well as lower excitation losses, with the extreme end of this phenomenon being CW-mode operation. Third, RMF strength must be high enough to effectively couple with the plasma but not so high that ohmic losses in the transmission lines and antennas, which scale like $I_\omega^2$, become dominant. Finally, changing pulse length may result in optimal coupling efficiency because any time for which the RMF is energized but propellant is not

being accelerated represents wasted power. Time pre-ionization and post-ejection of propellant therefore causes inefficiency, a phenomenon shared for all inductive pulsed thruster schemes [78].

## 2.6 Conclusions

In this section we have presented the theory of operation for the RMF thruster. We have discussed the established current drive model which has remain largely unchallenged to our knowledge since its initial derivation in 1962, and indeed was used in the design of every RMF thruster of which we are aware. We have also presented our update to this model, which relaxes several key assumptions to attempt to better explain thruster behavior. Chief among these relaxed assumptions was the stipulation that electron radial velocity be zero everywhere. This resulted in a theory which provides mechanisms by which an enhanced bias field may retard the electron azimuthal drift and by which the diamagnetic drift may take effect to enhance it. We then discuss how these currents might be leveraged to produce thrust, and how the efficiency of the RMF thruster can be broken down phenomenologically to better understand loss mechanisms.

# CHAPTER 3

# Experimental Apparatus

## 3.1 Introduction

The purpose of this section is to present the experimental setup used to characterize the RMFv2 and RMFv3 thrusters. To that end we begin by discussing the capabilities of the facility in which the experiments were performed. We follow this by explaining the use of each of the instruments used to take data. This includes quantitative direct measurement of thrust, RMF current waveforms, and induced magnetic fields. Qualitative conclusions about thruster operation can also be gleaned from high speed video, which is discussed here as well.

## 3.2 Facility

All data presented in this dissertation was taken at the Alec D. Gallimore Large Vacuum Test Facility (LVTF) at the Plasmadynamics and Electric Propulsion Laboratory (PEPL) of the University of Michigan, depicted in simplified schematic form in Fig. 3.1. LVTF is an approximately 6 m by 9 m chamber whose cryopumps provide up to an effective ∼500,000 L/s pumping speed for xenon [79], although not all pumps were used during the test campaigns discussed in this work. This resulted in a facility base pressure of $\approx 2 \times 10^{-7}$ Torr, with operating pressures on the order of $5 \times 10^{-6}$ Torr, measured in the plane of the thruster approximately 1 meter away according to pressure measurement best practices [80]. Myriad feedthroughs allowed for cooling water, propellant gas, data, and thruster telemetry to pass in and out of the chamber. Windows at three angles provided visual access to the thruster. Near-field probes such as the inductive probes analyzed in this work could be mounted on a two-axis motion stage at the thruster exit. A full suite of far-field probes which are not directly used here include Faraday, ExB, RPA, and Langmuir probes. These are positioned on a linear motion stage for individual alignment with the thruster behind a graphite shield

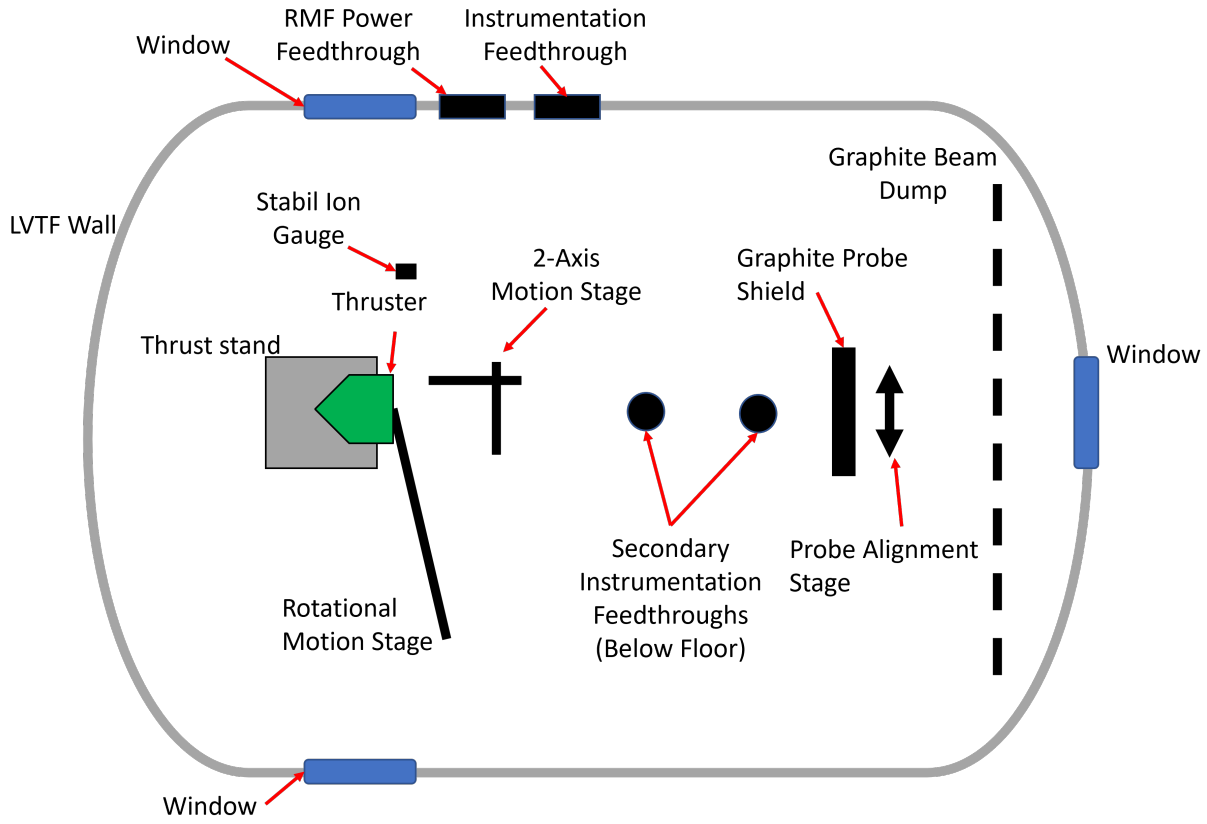


Figure 3.1: Test setup in the LVTF chamber, depicted in an overhead schematic view.

to provide protection against damaging high speed ions in the plume. Other probes, notably Faraday, can be mounted to a rotational arm whose center is co-located with the thruster exit to provide measurements swept throughout the plume.

## 3.3 Thrust Stand

### 3.3.1 Design

One of the major goals of this effort is to perform direct performance measurements of the RMF thruster. This can pose a technical challenge given that most state of the art thrust stands are designed to measure steady-state rather than pulsed devices. However, as was pointed out in Ref. [81], if the pulse rate is sufficiently faster than the natural frequency of a standard pendulum-based thrust stand, it is possible to infer the time-averaged performance. To this end, the RMF thruster was mounted on an inverted pendulum-type thrust stand designed with field-recognized best practices [82] in mind for measuring the performance of Hall thrusters. The thrust stand's natural frequency is approximately 1 Hz, while the

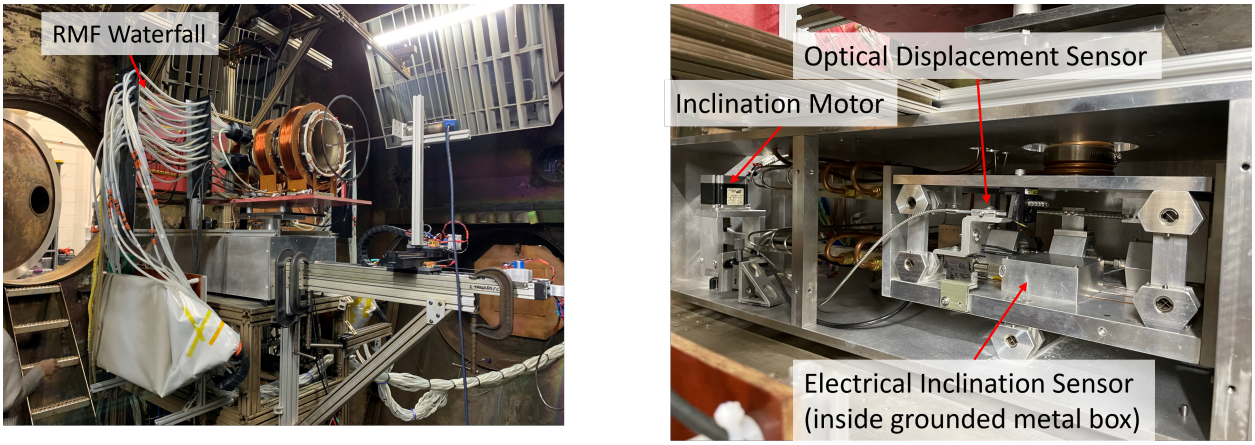


Figure 3.2: The RMFv2 thruster mounted on the thrust stand in LVTF. a) RMF transmission lines drape across a 'waterfall' where they are strain relived on either side to reduce rubbing effects and minimize impact on thrust stand overall spring constant. b) Close up view of thrust stand internals.

both the RMFv2 and RMFv3 were operated at pulse rates greater than 75 Hz, with the significantly higher frequency allowing for steady-state thrust measurement. The RMFv2 mounted on the thrust stand, as well as a photograph of thrust stand internals, are shown in Fig. 3.3.

With that said, as this thrust stand is intended primarily for characterizing steady-state devices, there were a number of technical challenges in adapting its operation to measuring our pulsed device. To illustrate this, we first describe the principle of operation of the system. Figure 3.3 shows the design of the thrust stand.

When the thruster is switched on, the thrust will apply a force to the thruster mounting plate in the positive x direction as per the coordinate in the figure. This stand is normally operated in null mode, in which current is passed through a magnet known as the null coil applies a force to counteract the thrust, while a separate current is passed through the damper coil to help dampen transients. The current required to maintain zero displacement is calibrated to the thrust using a series of known weights, and the displacement is measured using an optical displacement sensor, labelled ODS in Figure 3.3a. An inclinometer meanwhile measures the total inclination of the thrust stand, which is separately calibrated to the force required to maintain null signal. To arrive at the total thrust, the current to the null coil and inclination are both taken into account.

In the RMF's case, the electromagnetic interference from the pulsed currents through the antennas made active control impossible by disrupting the control signals. Therefore the stand was operated in a displacement mode, in which displacement and inclination were

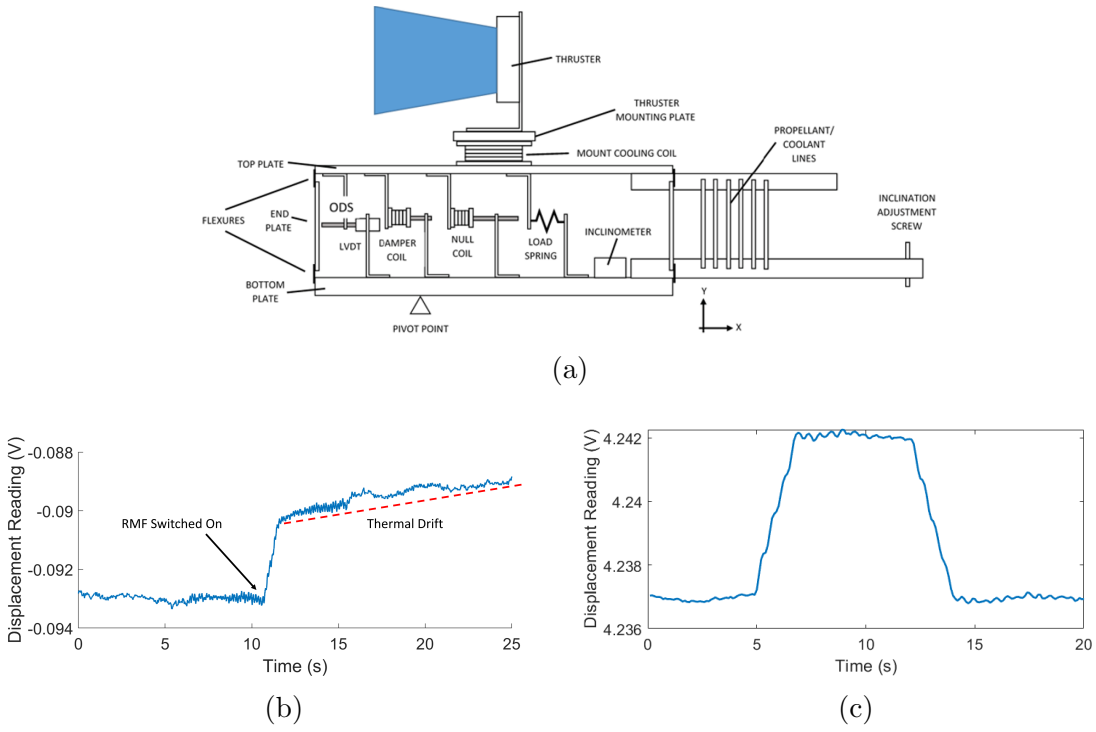


Figure 3.3: a) Schematic of the inverted pendulum thrust stand used, b) Typical displacement signal for RMFv2 thruster, c) Typical displacement signal for RMFv3 thruster operating in pulsed mode

measured but not controlled. Rather than correlate null coil current to thrust, the displacement itself was calibrated using known weights. Because the displacement is measured using an optical displacement sensor whose transducer is situated outside the vacuum chamber, the displacement measurement itself was unaffected by electrical noise. The inclination, meanwhile, exhibited increased noise, which is reflected in uncertainty in the thrust measurements.

### 3.3.2 Calibration

Calibration is crucial for accurate thrust stand measurements because of the vast number of non-ideal effects which can have dramatic impact on the result of a thrust measurement. Separate calibrations were performed for the pulsed-mode thrust measurements and the CW-mode measurements because the magnitude of the typical thrust value for the two modes varied by an order of magnitude, though the displacement-to-thrust conversion value for each was within uncertainty of the other. Calibration was accomplished in a two-step process because thruster inclination was not rigidly locked down during measurement. Because changes to thrust stand inclination can effect the displacement due to the weight of the thruster, we separate displacement into that due to thrust and that due to inclination:

$$d_0 = d_{inc} + d_{Th} \tag{3.1}$$

where $d_0$ is total measured displacement, $d_0$ is the displacement caused by the thruster weight acting upon a nonzero inclination, and $d_{Th}$ is the displacement caused by thrust. To determine $d_{inc}$, we created a calibration by using a stepper motor to drive the thruster inclination to 5 separate values while measuring both pitch and displacement. This was used to generate a least-squares fit of the form

$$d_{inc} = m_i I + d_{0,i} \tag{3.2}$$

where $m_i$ is the change in displacement per unit inclination change and $d_{0,i}$ is the displacement value without inclination change. After determining $m_i$ from the displacement versus inclination calibration, we were able to calibrate for displacement versus thrust. A series of known weights were applied to the thrust stand via a pulley while displacement and inclination were recorded. Pulsed-mode weights ranged from 4.21 to 15.78 mN, while CW-mode

weights ranged from 4.21 to 115.15 mN. By doing so, we again generate a least-squares fit:

$$F = m_{Th}\left(d_0 - (m_i I + d_{0,i})\right) + d_{0,Th} \tag{3.3}$$

$$= m_{Th}\left(d_0 - m_i I\right) + y_0 \tag{3.4}$$

where $m_{Th}$ is the slope of the fit between thrust $F$ and the inclination-corrected displacement. $d_{0,Th}$ is the intercept of that fit, and multiple constants have been combined into $y_0$. For both pulsed-mode and CW-mode, thrust was measured by comparing the force registered by the thrust stand with the thruster on to the force with the thruster off. Therefore

$$T = m_{Th}\left(\Delta_{d_0} - m_I \Delta_I\right) \tag{3.5}$$

where $\Delta$ refers to the difference between the thruster on and thruster off for the quantity in subscript.

### 3.3.3 Operation

Because the PPU was only capable of running at full power for 5-10 minute intervals due to cooling constraints, it was not possible to operate the thruster at full thermal steady-state. For the RMFv2 thruster, this caused thermal drift to become a concern, so displacement and inclination data were taken immediately before and after the thruster was switched on to eliminate the impact of this drift. An example displacement signal waveform is shown in Figure 3.3b to illustrate this. Finally, the influence of anomalous thrust due to inductive effects from the current pulse and from line whip to electromagnetic interference on data collection devices must be eliminated. To do so, displacement and inclination waveforms were collected using vacuum shots (no propellant flow), and a correlation was developed to relate the anomalous signal to the amplitude of the current pulse. An anomalous thrust was then determined for each measurement setpoint by using the current amplitude to anomalous thrust correlation, and the false signal was then subtracted.

This challenge is avoided entirely in the RMFv3 thruster, where design changes discussed in Chapter 7 eliminate these nonideal effects. Fig. 3.3c shows how the relative impact of thermal drift has been reduced to the point that it can be neglected. The RMFv3 thruster has an additional quirk in its CW-mode operation, however, in that the bias magnetic field must be energized after the rotating magnetic field has initiated the plasma discharge. Because energizing the bias magnets cause the thrust stand to move because of magnetic material in the thrust stand, CW-mode data is taken with the following procedure:

1. RMF on

2. Bias field on

3. RMF off (take displacement delta for thrust measurement)

4. Bias field off

We emphasize that all thrust measurements across devices were taken comparing the RMF energized versus de-energized states, with flow and seed plasma remaining unchanged. Therefore, any thrust which is measured can be attributed solely to the effect of the RMF rather than neutral gas flow or acceleration of the seed plasma via a magnetic nozzle effect. This is important to keep in mind as some thrust measurements are quite low (single milliNewtons) especially for the RMFv2 thruster.

## 3.4 RMF Current Measurement

As will be discussed in Chapter 4, RMF current waveform data is critical to understanding how power couples into the plasma. We captured RMF current for the RMFv2 thruster using a Pearson 110 current monitor on each antenna. As the RMFv3 is operated with a three-phase antenna, we added a Pearson 1025 current monitor to the third phase. A different model was used on the last antenna due to availability of equipment. Both units have the same measurement uncertainty of 1%, with their chief difference being their gain (output volts per measured amp). Current monitors were placed at the junction where the antenna meets its associated tuning capacitor bank for both thrusters. This was done to capture the actual current passed through the antennas and minimize false signal due to stray capacitance or reflected power which was present when measuring current directly at the PPU.

## 3.5 Inductive Probes

The magnetic field measurements presented in this work were acquired using a two-axis Bdot probe constructed according to electric propulsion community best practices [83]. This probe consists of two orthogonally-oriented 1.25 cm diameter by 0.64 cm long fiberglass bobbins, around which 24 AWG enameled copper wire is wound. A pyrex tube is fit over these copper bobbins to protect against damage from the plasma. The two bobbins are offset $\sim$0.3175 cm from each other both axially and radially. The final result is shown in Fig. 3.4.

The 2-axis probe was mounted on a 2-axis motion stage with one of the probe's windings normal to the thruster axis and the other normal to the radial direction. By translating the

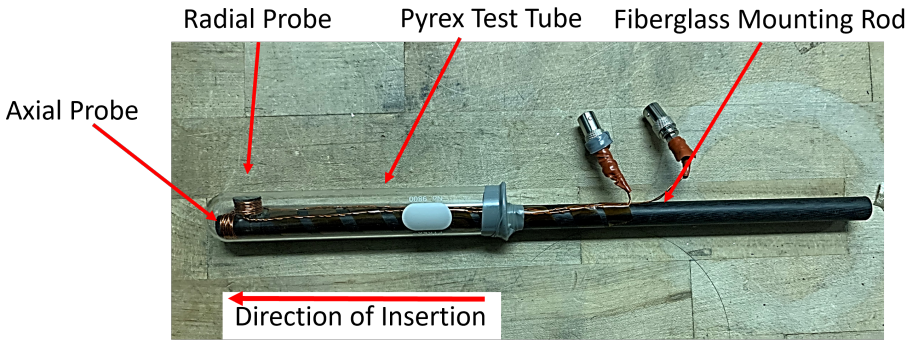


Figure 3.4: Bdot probe used in the inductive probe studies discussed in this work.

probe throughout the interior of the thruster and recording the signal at each location, a spatially and temporally resolved map of the induced magnetic field can be measured. Data points were taken at 2 cm intervals both axially and radially inside the cone. 25 thruster pulses were captured at each location for data averaging for the RMFv2, while 10 pulses were used for the RMFv3. We note that variability in the separate shots was low. For example, at the peak value of total integrated current, the standard deviation was approximately 0.75% of the mean for the RMFv2 data presented in Chapter 6.

These probes function according to Faraday's Law, by which a voltage is induced on each wire wrap according to the time rate of change of magnetic flux through the coil. We compute the average magnetic field enclosed by the probe by integrating this signal. In practice, the measured signal has contributions from both the quantity of interest, the driven azimuthal current, and the RMF itself. This poses a measurement difficulty because the latter is often 10-100 times stronger than the former. Therefore because the time scale for changes in the induced azimuthal current is an order of magnitude lower than the fundamental RMF frequency, we reduce the RMF signal by employing a fourth-order RC low-pass filter with a cutoff frequency of 100 kHz. This filtering also eliminates electrostatic coupling which could stem from the ≈10 kV voltage oscillation on the RMF antennas. This coupling would occur at the same frequency as the RMF itself.

The filter and the necessary length of BNC cabling introduced non-ideal circuit effects, requiring a frequency-dependent calibration for these probes to account for both amplitude and phase offset as a function of signal frequency. We followed Ref. [84] to accomplish this calibration by generating a transfer function determined by applying a current of known frequency and amplitude into a Helmholtz pair placed over the probe in-situ. The calibration

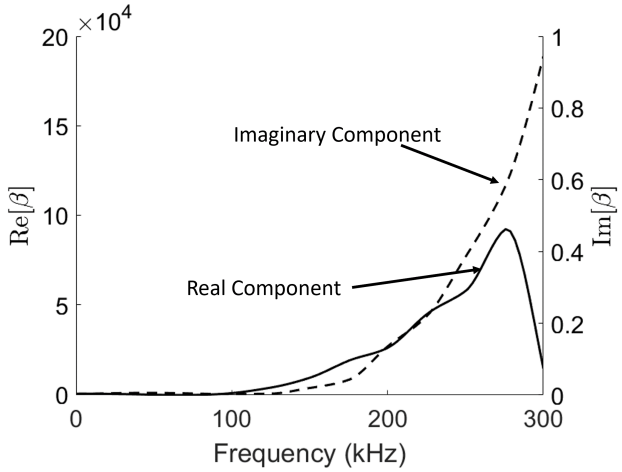


Figure 3.5: Example calibration transfer function for the axial Bdot probe employed in this study.

takes the form of a probe-specific, frequency-dependent transfer function $\beta(f)$ such that

$$\beta = \frac{\mathrm{FFT}\left(V_p\right)}{\mathrm{FFT}\left(\dot{B}_{cal}\right)} \tag{3.6}$$

$$= \frac{\mathrm{FFT}\left(V_p\right)}{\mathrm{FFT}\left(\alpha \dot{I}_{cal}\right)} \tag{3.7}$$

where $V_p$ is the voltage read from the probe and $\dot{B}_{cal}$ is the known externally applied magnetic field for calibration purposes, generated in our case by the Helmholtz pair. We have also made the further substitution that $B_{cal} = \alpha I_{cal}$ where $I_{cal}$ is the measured current injected into the calibration Helmholtz pair, and $\alpha$ is a constant which describes the magnetic field produced per amp at centerline. This produces a calibration transfer function such as the one depicted in Fig. 3.5.

Fig. 3.6a displays a representative signal output for a Bdot probe over the course of a thruster pulse. We note that the signal begins and ends close to zero voltage, consistent with no changing magnetic fields between pulses. The initial negative swing corresponds to current spinup and plasmoid formation generating magnetic flux in the negative direction, and the positive feature proceeding corresponds to the plasma ejection and relaxation of the plasma current. Additionally, the integral of the initial downward trend appears to be equal to that of the positive swing, a key feature of a correct Bdot probe trace. Despite this, it is common for integration error to become significant when integrating the pulse to generate the actual field measurement as Fig. 3.6b shows. While this error is relatively small at this location, its relative magnitude can vary across the device and contribute more

significantly to uncertainty in total aziumthal current and Lorentz force as we show in greater detail in Chapter 6. This effect was eliminated for the RMFv3 thruster, however, through more careful oscilloscope range setting. A further possibility for error in the inductive probe measurements may arise from induction to the probe leads. Although the wire quickly transitions from the bobbins to twisted pair and then to coaxial cable, it may be the case that these wire leads may pick up signal due to magnetic fields not purely aligned with the orientation of the bobbin in question. These stray pickup effects were not quantitatively investigated. We noted qualitatively during calibration however that signal on the probe not aligned with the Helmholtz pair picked up small signal ($\leq$1-2%) in comparison to the probe under calibration.

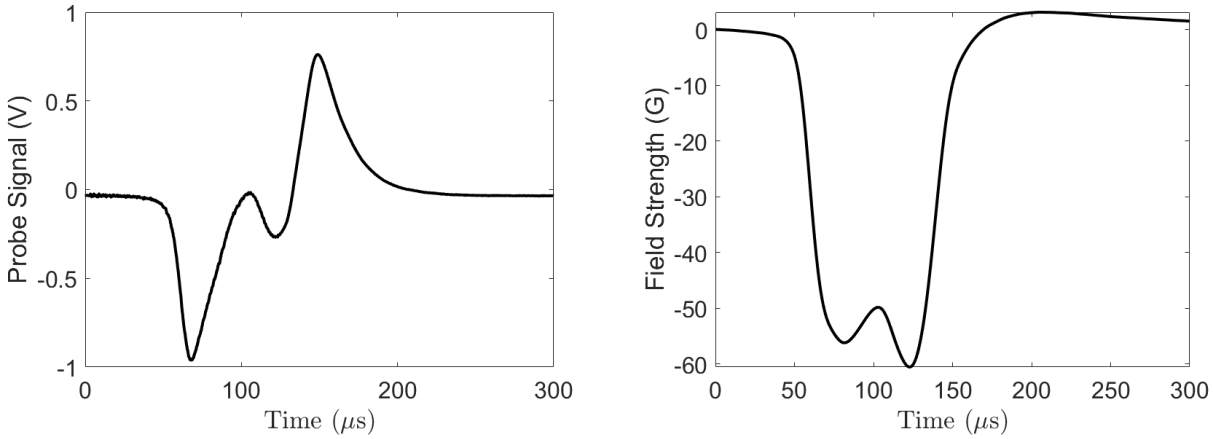


Figure 3.6: a) Example uncalibrated Bdot probe trace for the RMFv2 thruster b) Calibrated and integrated signal from a).

## 3.6 High Speed Photography

High speed video was used throughout the experimental campaigns which make up this work as an important qualitative indicator of thruster operation. The high speed camera used is a Photron FASTCAM SA5 which was mounted on the window situated to the thruster's right in Fig. 3.1. The majority of high speed video was recorded at 50 kHz frame rate and equal shutter speed. Although video of plasmoid ejection is useful, the high speed camera was invaluable in the initial setup of the RMFv2 thruster in particular. The antennas on that device could oscillate as much as 15 kV, and were positioned close to the (near-ground) plasma. Using video to locate electrical plasma/antenna shorts was critical to our

development of a robust connection insulation scheme. Data collection may not have been possible in some cases without the capability to locate on which of the 120 total connection points failure occurred. These challenges, like many others, were solved in the updated design of the RMFv3 thruster.

## 3.7 Summary

In this section we have detailed the experimental apparatus used to take the data presented and discussed later in this work. This included the facility as a whole as well as specific instruments. Descriptions and operation for the thrust stand, RMF current measurement devices, inductive probes, and high speed camera were provided. We show in the next chapter how the raw data from these instruments were processed to provide meaningful measurements of relevant quantities.

# CHAPTER 4

# Analysis Techniques

## 4.1 Introduction

In this section we discuss the analysis techniques used to process raw data from the instruments described in Chapter 3 into useful metrics to characterize and understand thruster effectiveness. We begin with a discussion of how key figures of merit can be adjusted to better suit pulsed propulsion devices. From there, we show how the RMF current waveforms can be used to calculate the power successfully deposited into the plasma as a fraction of total input power, a critical metric we refer to as coupling efficiency. Next we provide a description of how inductive probing results can be translated into plasma current and how the measured magnetic fields can be separated into their constituent sources. Finally we address how uncertainty is quantified for the results presented later.

## 4.2 Characterizing Pulsed Propulsion

In principle, the performance for a pulsed-mode propulsion device must be measured differently than that of a steady-state device because each pulse delivers a finite impulse $J$ rather than a steady thrust $T$. Fortunately for us, because the RMFv2 and v3 thrusters operate at significantly higher repetition rate than the natural frequency of the thrust stand, it is valid to make time-averaged thrust measurements. This allows us to use Eqns. 1.5 and 1.6 to calculate specific impulse and efficiency [81]. However, both of these thrusters rely on steady mass flow rate into the device regardless of pulse repetition rate. Therefore these expressions include the additional propellant mass which is lost between shots, thus reducing the specific impulse and efficiency relative to a more flight-like design. Such a device would likely employ a puff valve to release only the required propellant for a given shot rather than waste propellant during 'dead' time. As the goal of these test units are to analyze the physics behind RMF thruster operation, it can be helpful to modify Eqns. 1.5 and 1.6 to

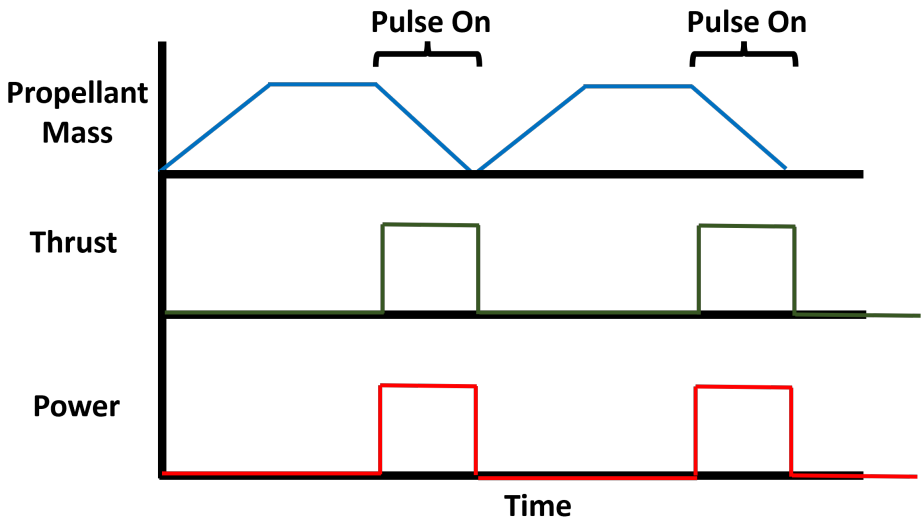


Figure 4.1: Timeline of pulsed-mode operation illustrating the fact that while power and thrust are proportional to duty cycle, the mass used by the thruster is not.

consider only the propellant mass which is present during an RMF pulse. This results in 'active' or 'per-pulse' quantities for specific impulse and efficiency. To do so, we consider the plasma ejected from a pulse as a slug of finite mass which produces an instantaneous impulse. Therefore we may write

$$I_{sp}^{*} = \frac{J^{*}}{gm^{*}} \tag{4.1}$$

$$\eta^{*} = \frac{J^{*2}}{2m^{*}E^{*}} \tag{4.2}$$

where $I_{sp}^{*}$ is the 'active' specific impulse, $\eta^{*}$ is the 'active' efficiency, $J^{*}$ is impulse, $m^{*}$ is slug mass, $E^{*}$ is input energy, and the asterisk superscript indicates that these are quantities associated with a single pulse rather than an steady quantity such that $P = E^{*}f$ and $T = J^{*}f$ where $f$ is the repetition rate of the thruster. However, because mass flow is steady during pulsed operation in these devices (we do not employ a puff valve/pulsed pre-ionizaiton scheme), $m^{*} \neq \frac{\dot{m}}{f}$ as additional propellant is 'wasted' between pulses as depicted in Fig. 4.1. The value for $m^{*}$ is difficult to determine experimentally without the use of fast puff valves in the thruster. Given our steady flow scheme both for neutral injection and seed plasma, we opt to make an estimate for $m^{*}$ with the caveat that while the resulting values for $\eta^{*}$ and $I_{sp}^{*}$ are valuable for examining trends in the data, any direct comparison to a CW-mode measurement or with another device should be done with the understanding that these are approximations without ground-truth data for the mass per pulse. To do so, we consider

thermal diffusion of a neutral gas through the a plane:

$$n = \frac{4\dot{m}}{\pi r^2 M c_{th}} \tag{4.3}$$

where $n$ is neutral density, $M$ is molecular mass, and $c_{th} = \sqrt{\frac{8kT}{\pi M}}$ is the thermal speed of the neutrals (approximately 213 m/s for the room-temperature Xenon used in this study). By assuming a straight-walled cone such that $r = z\tan(\alpha)$ where $\alpha$ is the cone half-angle and $z$ is position along the cone beginning at the narrowest upstream point, we can integrate $n$ throughout the volume of the cone and multiply by molecular mass to arrive at

$$m^* = \left(\frac{4l}{c_{th}}\right)\dot{m}. \tag{4.4}$$

where $l$ is total thruster length. Making this substitution, we find that

$$\eta^* = \frac{c_{th}}{4lf}\eta \tag{4.5}$$

$$I_{sp}^* = \frac{c_{th}}{4lf} I_{sp} \tag{4.6}$$

This analysis makes the assumption that the thruster has sufficient time to completely fill with neutrals between RMF pulses, which is met for both pulsed devices discussed in this work.

We note as well that the mass considered may be greater in reality due to neutral injection by the thruster of background gas, as is a significant effect in e.g. Hall effect thrusters [85]. This effect is likely small for the RMF thruster, however, as testing for the RMFv3 thruster was found not to depend on background neutral density within error between $10^-7$ and $10^-6$ Torr background, which was adjusted by selectively turning cryopumps on and off. We found both CW-mode and pulsed-mode to exhibit the same lack of dependency on background pressure.

## 4.3 Coupling Efficiency

Further insight into thruster performance may be gleaned by considering trends against the power successfully coupled into the plasma rather than lost to the PPU switches or to ohmic heating in the antennas. This allows us to differentiate between total efficiency, which considers the ratio of directed kinetic power in the plume to total input power, and the post-coupling efficiency, which considers only the power which has been coupled to the

plasma as its input and includes divergence, mass utilization, and plasma efficiency in the framework of Eq. 2.35. To determine coupling efficiency, we first split total power between transmission losses and coupled power:

$$P_0 = P_\Omega + P_p \tag{4.7}$$

where $P_0$ is the total power, $P_\Omega$ is transmission loss, and $P_p$ is power coupled to the plasma. We then consider that

$$\eta_c = \frac{P_p}{P_0} = \frac{P_0 - P_\Omega}{P_0} = 1 - \frac{P_\Omega}{P_0}. \tag{4.8}$$

Because $P_0$ is easily measured by monitoring current and voltage output of the main DC power supply, it remains to determine $P_\Omega$. Applying Ohm's law to the antenna current, we see that

$$P_\Omega = \sum_i^3 \int I_{\omega,i}^2 R_{eff} dt \tag{4.9}$$

where $I_{\omega,i}$ is the current passing through the $i$th antenna and $R_{eff}$ is the effective resistance of an antenna, a number which includes switching losses and ohmic losses in the transmission lines and antenna. We must sum over the three antennas to account for losses in each. Eq. 4.9 assumes that each antenna has a similar value for $R_{eff}$ because the nature of the PPU precludes individual measurement. With this said, because the return path for any given antenna is through the other two antennas, this is likely a good assumption. We determine $R_{eff}$ by operating the thruster without propellant flow to eliminate any plasma coupling and measuring power draw and current:

$$P_{0,V} = \sum_i^3 \int I_{\omega,V,i}^2 R_{eff} dt \tag{4.10}$$

where the subscript $V$ refers to quantities measured with no propellant flow, i.e. in vacuum. Because we assume $R_{eff}$ does not change significantly over time, we can substitute Eqns. 4.9 and 4.10 into Eq. 4.8:

$$\eta_c = 1 - \frac{P_{0,V} \sum_i^3 \int I_{\omega,i}^2 dt}{P_0 \sum_i^3 \int I_{\omega,V,i}^2 dt}. \tag{4.11}$$

Physically, Eq. 4.11 suggests that ideal power coupling is achieved when either vacuum shot RMF current is much higher than plasma shot RMF current or when vacuum shot power is

much lower than plasma shot power. In the pulsed-mode where the DC supply is voltage-limited, high coupling manifests as the former, while in CW-mode where the DC supply is current-limited high coupling manifests as the latter. Physically, both of these mechanisms agree with the concept that the plasma can be considered an effective resistance on the RMF circuit [72].

## 4.4 Plasma Current and Lorentz Force

The primary reason for taking measurements with inductive probes as discussed in Sec. 3.5 is to calculate current density and Lorentz force in the thruster. We calculate the current density as a function of time and location using Ampere's Law:

$$\vec{j} = \frac{1}{\mu_0}\vec{\nabla} \times \vec{B} \tag{4.12}$$

$$j_\phi = \frac{1}{\mu_0}\left(\frac{\partial B_r}{\partial z} - \frac{\partial B_z}{\partial r}\right), \tag{4.13}$$

where we have made the assumption that the induced plasma current runs only in the azimuthal direction, and where $B_r$ and $B_z$ refer to the results of our Bdot probing measurement. We assume in Eq. 4.12 that displacement currents are negligible in our device per Ref. [83]. This stems from the fact that displacement fluctuations are only expected at frequencies greater than the plasma frequency. The characteristic time scale for the RMF is orders of magnitude lower than this frequency (100 GHz). After interpolating the magnetic field measurements inside the thruster cone to allow for smoother derivatives, we calculate the spatially-resolved current density at each time step.

We then compute total current by integrating the current density over the interior of the thruster:

$$I_\phi(t) = \int_A j_\phi dr dz. \tag{4.14}$$

Finally, we arrive at the total force at any given time by volumetrically integrating the Lorentz force:

$$F_z = \int_V B_r j_\phi d^3r \tag{4.15}$$

$$F_r = \int_V B_z j_\phi d^3r, \tag{4.16}$$

where $F_r$ and $F_z$ denote the total Lorentz force on the plasma in the radial and axial directions

respectively. Once the force is known, we calculate the impulse per shot by integrating Eq. 4.15 with respect to time for the duration of the pulse:

$$J^* = \int F_z dt, \tag{4.17}$$

where $J^*$ is the impulse per shot.

## 4.5 Identifying Magnetic Field Sources

We identify three sources for magnetic field in this thruster: the bias field, which is due to the DC electromagnets surrounding the thruster; the self-field, which is due to the induced plasma currents; and the structure field, which is due to secondary induced currents in conductive structural elements due to the rapid rise of plasma currents. These currents may be induced in the bias electromagnets, in which case the structure field accounts for any deviation from the steady bias field, which is assumed to remain fixed throughout the pulse. Fig 4.2 depicts these three fields in cartoon form. We note that the expressions noted in the figure are of rough proportion only, and will be very sensitive to the distributions of currents in the thruster. The structure field in particular will depend not only on the plasma currents but their positioning relative to any structural elements as these distributions effect the mutual inductances present. This field will tend to repel the plasma from the structural element in question, which could result in a negative structure force if strong structure currents are generated in elements far downstream of the plasma.

Differentiating between the bias magnetic field and the other two sources is trivial as the bias field is not detected by the Bdot probes due to its steady nature. To separate the self-field and the structure field, we first calculate the current density in the plasma from the Bdot measurements using Eq. 4.13. Because the self-field is directly caused by the plasma current, it can be determined from the current density measurements via Biot-Savart's Law. Any magnetic fields not captured by applying Biot-Savart's law to the plasma current must be due to currents outside the plasma. We therefore arrive at the structure field by subtracting the self-field from the measurement:

$$\vec{B}_{struct} = \vec{B}_{meas} - \vec{B}_{self}. \tag{4.18}$$

Once $\vec{B}_{bias}$, $\vec{B}_{self}$, and $\vec{B}_{struct}$ have been identified, they can each be separately substituted into Eqns. 4.15 and 4.16 to determine individual contributions to impulse.

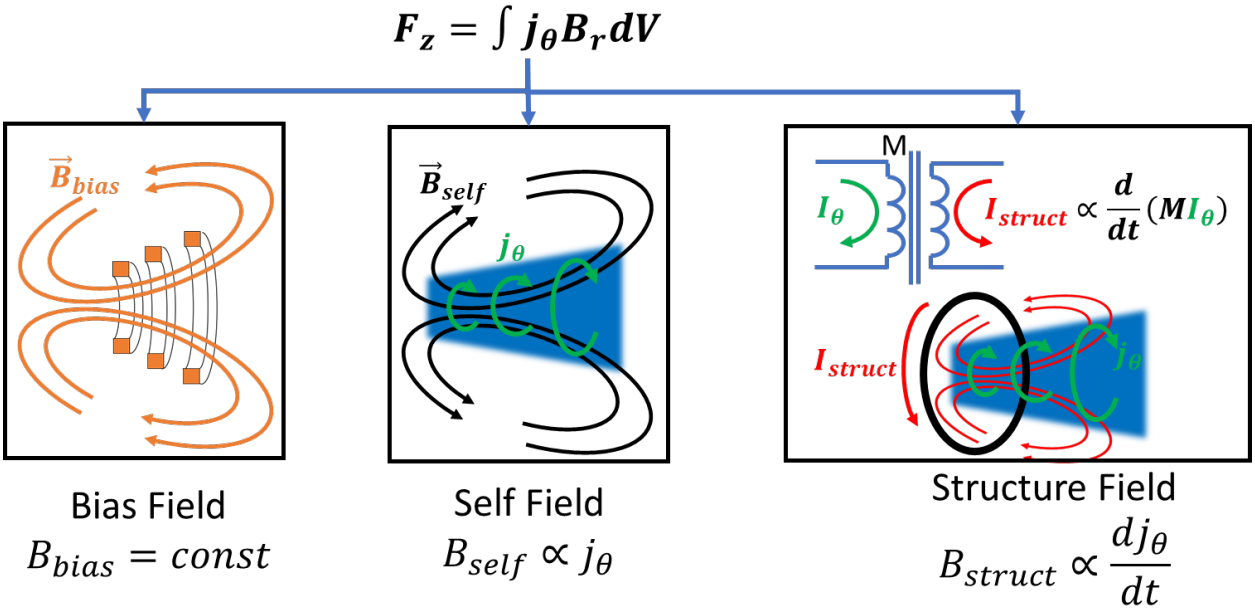


Figure 4.2: Magnetic fields present in the RMF thruster by source

## 4.6 Uncertainty Quantification

Uncertainty in the measurements presented in this work are propagated in quadrature according to standard practices. Sources of uncertainty considered for each measurement are as follows.

For thrust, each term in Eq. 3.5 has associated uncertainty. Uncertainty in $m_I$ is caused by error in the linear fit between inclination and resulting displacement. Uncertainty in $m_{Th}$ is due to that of the linear fit between inclination-calibrated displacement and calibration weights, which in turn have their own uncertainty. Finally uncertainty in the inclination-calibrated displacement delta, $\Delta_{d_0} - m_I\Delta_I$, is driven by noise in the signal. Overall uncertainty in thrust is dominated primarily that of $m_{Th}$ and $\Delta_{d_0} - m_I\Delta_I$, both of which are in turn driven by measurement noise which reduces our ability to know exactly the displacement of the thrust stand. Further, the impact of the $m_I\Delta_I$ term is negligible owing to the inclination correction's low (typically $\leq$2%) impact on the total displacement, causing its uncertainty to be dominated by that of $\Delta_{d_0}$ when propagated in quadrature. Total typical thrust uncertainty is approximately 5% for CW-mode measurements and 10% for pulsed-mode measurements. The higher pulsed-mode uncertainty is due to its lower total thrust; not only is the inclination-corrected measurement delta closer in magnitude to the noise floor, but the displacement calibration slope $m_{Th}$ is less certain because of the reduced range of the calibration weights.

Specific impulse uncertainty, as dictated by its calculation in Eq. 1.5, is caused by that

of thrust and mass flow rate, which is the greater between 0.6% of the mass flow or 0.1% of full scale for the mass flow controller used for that injection source. Efficiency, calculated via Eq. 1.6 uses the above values as well as uncertainty in total input power, which is determined by instrumentation-specific measurement error in the backing power supply's voltage and current. Coupling efficiency as shown in Eq. 4.11 relies on these same voltage and current measurements, as well as RMF antenna current waveform measurements, which have an uncertainty of +1/-0% caused by the Pearson 110 and 1025 coils used to acquire those data. Uncertainty for specific impulse and total efficiency are driven primarily by thrust stand while that of coupling efficiency is not strongly dominated either by power measurements or current waveform measurements.

## 4.7 Summary

In this section we have discussed the analysis techniques necessary to convert raw data from thruster instrumentation into the meaningful results which will be presented in the following chapters. First we discussed how we adjust efficiency and specific impulse measurements for pulsed-mode data to disregard propellant wasted while the RMF is not energized, a technique which better allows us to examine the per-pulse physics of the device. We then present how we calculate coupling efficiency, a key performance metric for an RMF thruster, before showing how induced magnetic field measurements can be used to determine plasma current and Lorentz force, and finally how that Lorentz force may be ascribed to a particular magnetic field contribution. We close by giving a description of how uncertainty is quantified throughout the results.

# CHAPTER 5

# The PEPL RMFv2 Thruster: Design and Baseline Performance

## 5.1 Introduction

In this chapter we focus on the RMFv2 thruster. We begin by motivating its construction in the context of prior efforts to investigate this thruster scheme. This is followed by a discussion of the design employed when creating the RMFv2. We note that the operating principles which motivated the design of the thruster do not reflect our current understanding, but a discussion of the physical motivation for our design choices is included for context. This leads into a description of the thruster itself as well as the power processing unit employed to generate the oscillating currents to produce the RMF. This is followed by qualitative observations of thruster operation, including high speed photography. Quantitative performance results are shown next, which motivate the inductive probing discussed afterwards. Finally, we discuss these results in the context of thruster design and lessons learned for the next iteration of the RMF thruster.

## 5.2 Design Motivation

The design and construction of the RMFv2 thruster was motivated in large part by the null performance measured on the RMFv1 thruster [1]. This thruster, pictured in Fig. 5.1a, was constructed with an aluminum discharge chamber which doubled as the bobbin structure for the bias field magnets. To produce the oscillating currents required to generate the rotating magnetic field, it employed a capacitor bank which discharged each shot and recharged between shots. By adding an additional inductor in line with the antenna, the discharge would ring down at the chosen RMF frequency resulting in a RMF current profile such as the one shown in Fig. 5.1b. The RMFv1 operated at a bias field strength of up

to 500 G, with an RMF frequency of either 20 kHz or 125 kHz depending on the in-line inductor used, which could be changed out to adjust the resonant frequency of the device. However, circuit limitations precluded operation above ∼300 W for the 125 kHz condition. Other groups had created test units which produced nonzero thrust in the past, and a lack

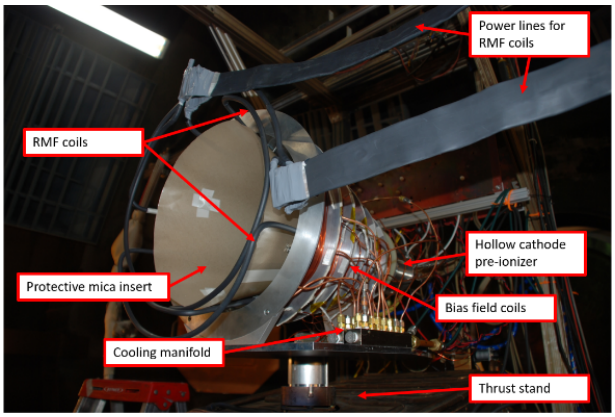


(a)

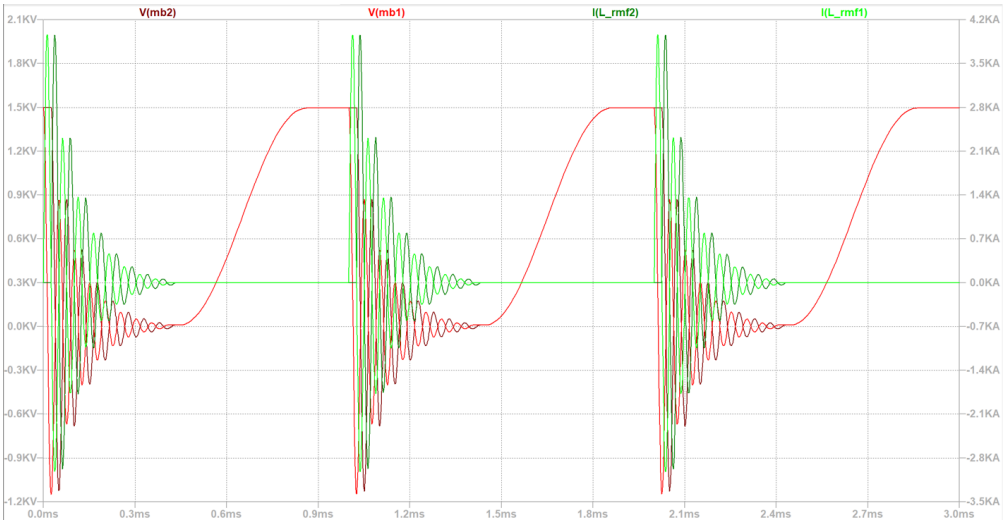


(b)

Figure 5.1: a) Photograph of RMFv1 thruster [1]. b) Example RMF current ringdown for RMFv1.

of significant illumination in the device was observed. Taken together along with the low ($\leq 2.25\%$) coupling efficiency observed, we reached the conclusion that the fault rested with this device's significant design flaws rather than the architecture as a whole. In light of this, the purpose of the RMFv2 thruster was to attempt to produce a test article which showed positive performance. Such a working test article is a prerequisite to investigate the physics behind the RMF thruster, which is the ultimate goal of this work.

## 5.3 Thruster Design

In this section we discuss the design of the RMFv2 thruster. This involved employing theoretical thruster scaling along with lessons learned from the RMFv1 to arrive at a mechanical design which we hoped would be more effective. The power processing unit, responsible for generating the currents to produce the RMF, was developed in partnership with Eagle Harbor Technologies as part of an SBIR grant. We therefore entered into the mechanical design process with an expectation for peak RMF amplitude, energy per pulse, and frequency possible with our supply.

### 5.3.1 Proposed Scaling Laws

Here we show the process by which scaling laws were applied to the design process of the RMFv2 thruster. We emphasize here that this section is included primarily for context rather than to show our present understanding of thruster operation.

#### 5.3.1.1 Penetration

A chief design consideration is the concept of RMF penetration, a concept explored by Jones and Hugrass [51] and discussed briefly in Chapter 2. To reiterate, the penetration condition is met when the RMF is strong enough that it cannot be effectively screened out at the axis of the thruster by the currents generated at the walls. It can be determined by comparing a few key parameters:

$$\left(\frac{\nu_{ei}}{\omega_{ce}}\right)^2 \left(\frac{R}{\delta}\right)^2 \ll 1, \tag{5.1}$$

where $\nu_{ei}$ is the electron-ion collision frequency, $\omega_{ce}$ is the electron cyclotron frequency about the RMF, $\delta$ is the classical AC skin depth, and $R$ is the total radius of the plasma. Physically, this expression can be broken into two intuitive requirements. The first, depending on the ratio of collision to cyclotron frequency, enforces that the electrons are sufficiently tied to field lines to be considered entrained. The second, depending on the ratio of classical skin depth to plasma radius, means the field will not be screened out by eddy currents. This condition can be used to ensure that a device has sufficient RMF magnitude to achieve penetration by the addition of thruster-specific information.

We assume the RMF is generated by a 2-phase antenna consisting of two Helmholtz pairs. The magnitude of the magnetic field generated by a Helmholtz pair near the center of the

loops is a well-known result, given by

$$B_\omega(z) = \left(\frac{4}{5}\right)^{\frac{2}{3}} \frac{\mu_0 I_\omega}{R_{antenna}(z)} = \sqrt{3}\left(\frac{4}{5}\right)^{\frac{2}{3}} \frac{\mu_0 I_\omega}{R(z)}, \tag{5.2}$$

where $R_{antenna}$ is the radius of each loop forming the pair, and due to the geometry of the thruster, the antenna loops are roughly a factor of $\sqrt{3}$ smaller than the radius of the cone structure. If this is the case, the electron cyclotron frequency can be written

$$\omega_{ce} = \sqrt{3}\left(\frac{4}{5}\right)^{\frac{2}{3}} \frac{e\mu_0 I_\omega}{m_e R(z)}. \tag{5.3}$$

Next we address the collision term. We recognize that collisions serving to reduce electron field line entrainment will come from neutrals as well as ions since we will not necessarily have a fully-ionized plasma at all times. Thus we use $\nu = \nu_{ei} + \nu_{en}$ in Equation 2.27, with $\nu_{en}$ being electron-neutral collisions. Therefore we have

$$\left(\frac{\nu_{ei} + \nu_{en}}{\omega_{ce}}\right)^2 \left(\frac{R}{\delta}\right)^2 \ll 1, \tag{5.4}$$

where we turn to Eqs. 2.4 and 2.5 for the values of $\nu_{en}$ and $\nu_{ei}$. Next, we address the skin-depth term. Classical AC skin depth is given by

$$\delta = \sqrt{\frac{2\eta}{\mu_0 \omega}}, \tag{5.5}$$

with $\eta$ being the resistivity of the conductive medium. Resistivity can be put in terms of collision frequency using

$$\eta = \frac{m_e \nu}{e^2 n_e}, \tag{5.6}$$

which gives us

$$\delta = \sqrt{\frac{2m_e\left(\nu_{ei} + \nu_{en}\right)}{\mu_0 e^2 n_e \omega}}. \tag{5.7}$$

To determine the densities needed by Equations 2.5, 2.4, and 5.7, we further assume a radially-uniform density profile whose axial distribution is dictated by thermal diffusion so

that the density is given by

$$n_e(z) = n_0 \alpha \frac{R^2(z)}{R_0^2} \tag{5.8}$$

$$n_n(z) = n_0 \left(1 - \alpha\right) \frac{R^2(z)}{R_0^2} \tag{5.9}$$

where $n_e(z)$ is the electron density at any given axial location in the cone, $n_0$ is the total density at the cone's throat, $\alpha$ is the ionization fraction of the plasma, $R_0$ is the radius at the cone's throat, and $R(z)$ is the cone's radius at the given axial location. We now substitute Equations 5.8 and 5.9 into Equations 2.5, 2.4, and 5.7 for final expressions for $\nu_{ei}$, $\nu_{en}$, and $\delta$. These are then substituted into Equation 5.4. After simplification and evaluation of constants, we find the expression

$$\dot{m} \ll \left(2.0 \times 10^8 \left(\frac{1}{\alpha} - 1\right) + 1.7 \times 10^9\right)^{-\frac{1}{2}} \frac{I_\omega}{\alpha\sqrt{\omega}}, \tag{5.10}$$

where we note that the radius of the cone has cancelled out, yielding a single relation valid for the entire cone. This relation gives a limit to the allowable mass flow rate of Xenon into a cone-shaped RMF thruster with Helmholtz-pair-style antennas to ensure penetration given an anticipated degree of ionization in the seed plasma. Equation 5.10 tells us that if the plasma is too dense, either eddy currents will screen out the field at the edge of the plasma, or collisions will prevent electron entrainment despite apparent penetration. For a worst case, $\alpha = 1$ can be taken, corresponding with an assumption of full ionization. Meanwhile, in the case of no ionization—$\alpha = 0$—mass flow can take any value since there is no conductive medium to screen out the RMF.

#### 5.3.1.2 Per-Pulse Energy Target

While Equation 5.10 gives information about the propellant flow given PPU limitations, some sense for thruster size is also necessary to design a test unit. To find a scaling law for roughly how large the thruster should be, we consider the plasma as an inductor. As such, the plasma will have some capacity to store energy owing to the driven azimuthal current. We require that the energy per pulse available from the PPU be commensurate to the energy required to drive the azimuthal current in the plasma. The condition we seek to match becomes

$$U_{pulse} = 2\eta_c U_{spinup} \tag{5.11}$$

where $U_{pulse}$ is the available energy from the PPU per pulse, $\eta_c$ is the coupling efficiency which describes the fraction of energy transferred from the antennas to the plasma, and $U_{spinup}$ is the inductive energy associated with the azimuthal current in the plasma for full electron entrainment by the RMF. We have added an additional arbitrary factor of 2 to our required energy per pulse because actual acceleration mechanisms are not clear; in the event that energy coupling to the plasma does not take the shape of a clean delta function, energy might continue to couple to the plasma throughout the acceleration process, thus allowing the addition of more than $U_{spinup}$ to the plasma.

Because we consider the plasma as an inductor in this rough analysis, we take

$$U_{spinup} = \frac{1}{2} L_p I_\theta^2 \tag{5.12}$$

where $L_p$ is the effective self-inductance of the plasma. For the sake of an order of magnitude estimate, we consider the plasma's self-inductance to take the form of a single-turn solenoid of length $l$ and radius $R$, where $l$ and $R_{avg}$ are the thruster's length and average radius, respectively. In this case,

$$L_p = \frac{\mu_0 \pi R_{avg}^2}{l}. \tag{5.13}$$

Next, we estimate the azimuthal current by considering the total number of electrons present in the cone before a pulse. Because of the relatively low duty cycle we operate the thruster at, neutral particles entering the cone have sufficient time to reach steady-state density between pulses. For reference, the characteristic fill time of neutrals throughout our thruster is approximately 1.3 ms, while the time between pulses is approximately 13 ms, which is limited by the PPU. Therefore, we assume thermal diffusive steady-state at the beginning of each pulse. In other words, the mass flux through the exit plane of the cone must equal the mass flow into the cone. Mass flux through a surface is given by

$$\dot{m} = \frac{1}{4} n A M \langle c \rangle \tag{5.14}$$

where $n$ is the density, $A = \pi R^2$ is the area, $M$ is atomic mass, and $\langle c \rangle$ is thermal speed, given by $\langle c \rangle = \sqrt{\frac{8kT}{\pi M}}$. The density is therefore given by

$$n = \frac{4\dot{m}}{\pi R^2 M \langle c \rangle}. \tag{5.15}$$

This density can be integrated throughout the volume of a cone of length $l$ to yield the

expression for the total number of particles in the cone before ringing the RMF:

$$N = \frac{4\dot{m}l}{M\langle c \rangle}, \tag{5.16}$$

where the cone angle has dropped out, yielding an expression dependent only on the final length (or alternatively, radius) of the cone. If each particle is ionized by the RMF and each electron is entrained, rotating at a frequency $\omega$, the azimuthal current will be given by

$$I_\theta = eN\omega = \frac{4e\omega\dot{m}l}{M\langle c \rangle}. \tag{5.17}$$

Plugging back into Equation 5.12, we have

$$U_{spinup} = \frac{16\mu_0\pi e^2 R_{avg}^2 l\dot{m}^2\omega^2}{\langle c \rangle^2 M^2}, \tag{5.18}$$

which can be compared to the available energy per pulse with Equation 5.11 to relate the thruster geometry to the PPU capabilities.

#### 5.3.1.3 Application of Scaling Laws to Design

The basic scaling laws for penetration and cone sizing outlined above were used to determine the operating conditions and rough thruster size for the PEPL RMFv2. Because both conditions hinge on the performance of the PPU, we first determined what range of operation was physically reasonable with the Eagle Harbor system. To this end, the RMF PPU can supply pulses with up to 2 kA current amplitude at approximately 400 kHz RMF frequency. These pulses can draw up to approximately 25 J per antenna for a total of 50 J per shot, operating up to 75 Hz repetition rate.

Figure 5.2 illustrates the design conditions set out in Equations 5.10 and 5.18, which we used to determine the thruster's design. To ensure penetration, maximum propellant flow must remain below the penetration limit curve associated with the antenna current magnitude employed. To ensure commensurate energy between inductive capacity of the plasma and the PPU's output, the thruster should be operated along the energy target curve associated with its size. To produce Figure 5.2, a safety factor of 10 was applied to ensure the inequality in Equation 5.10, and Equation 5.18 was used with an anticipated coupling efficiency of 20% and a per-pulse energy of 50 J. Additionally, a cone half-angle was set to 14° to roughly match previous efforts.

Given the PPU's limitation of 2 kA and anticipated RMF frequency of 400 kHz, we selected a thruster length of 30 cm, as the associated energy limit curve intersects the 2 kA

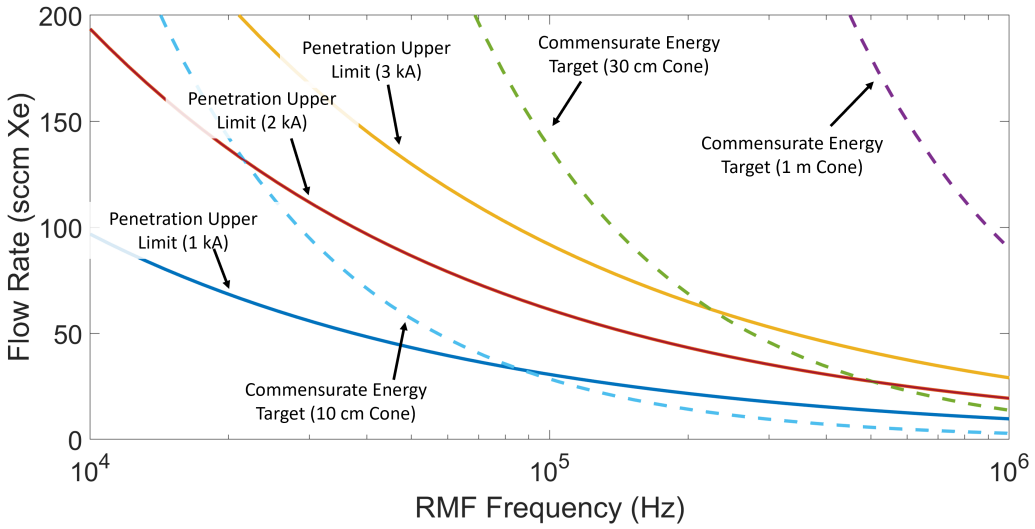


Figure 5.2: Upper limits on propellant flow as a functions of RMF frequency as put forth by Equations 5.10 and 5.18.

penetration limit curve at approximately 400 kHz. At this design condition we would then plan to operate using a maximum of approximately 50 sccm Xe propellant flow to ensure effective penetration and energy matching.

### 5.3.2 Thruster Mechanical Design

As the goal in our work is to establish the baseline operation of an RMF thruster, we first want to design a system that we have the highest confidence will produce measurable thrust and performance. To this end, we have applied the principles outlined in the above section, as well as insights from our previous work on the RMFv1 thruster [1] to design a new test article. We describe the key components in the following section, concluding by relating the design back to known scaling laws.

#### 5.3.2.1 Thruster body

As shown in Figure 5.3, the main body of the thruster, named the PEPL RMFv2, forms a truncated cone with a 14° half-angle. The opening at the downstream end measures approximately 8" in diameter, with an upstream (throat) opening of 3". This structure is lined with sheet mica to prevent the outward expansion of gas or plasma and built so that the RMF antennas can mount directly to it to minimize the distance from the antennas to the plasma itself for greatest coupling. The main structure and the magnet bobbins are made from a scaffold of G10 and FR4 pieces rather than machined from metal, which serves

to produce a very lightweight, inexpensive test device in addition to the primary effect of minimizing structural mutual inductance, which we believe to be advantageous based on circuit modelling analysis [86].

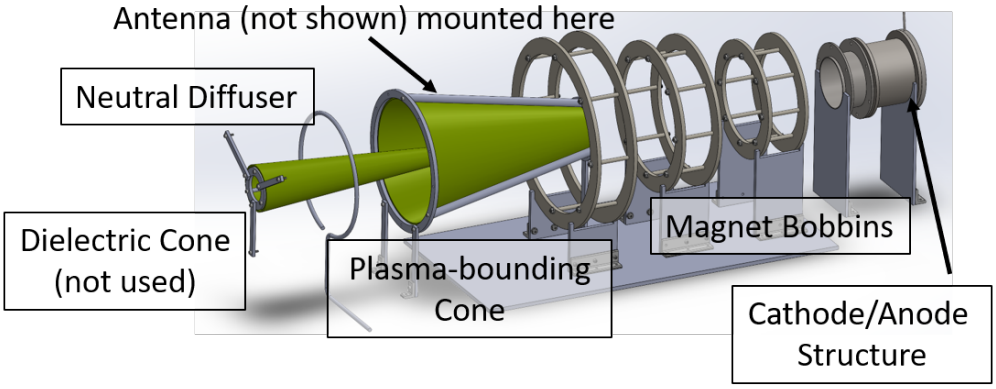


Figure 5.3: Exploded view of the PEPL RMFv2. Construction from G10 scaffold, with plasma-bounding surfaces made of mica sheets. Optional dielectric cone (not used in this study) can be mounted inside the mouth to convert the solid to an annular cone to alter flow properties.

#### 5.3.2.2 Bias Magnetic Field

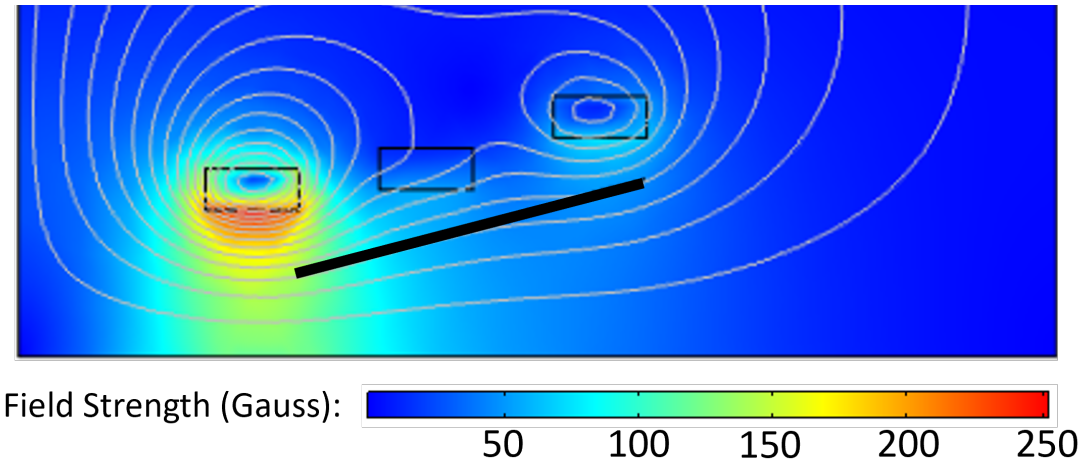


Figure 5.4: Map of bias field at 120 G centerline peak strength condition. Boxes indicate magnet locations. Solid line indicates thruster wall position.

The bias magnetic field is generated by three electromagnets situated about the body of the thruster. To find the desired current setpoints for each magnet, the magnetic fields

resulting from a nominal current through each was measured using a Hall effect probe. The fields were then superposed and scaled to produce a field shape which is tangent to the cone at its edge, as shown in Figure 5.4. There do not yet exist comprehensive scaling laws which take into account bias field shape. This tangent field line condition was chosen from the perspective of electron movement. It represents a middle ground between a too-strongly divergent magnetic field in which electrons tied to field lines would be forced into the walls, and a too weakly divergent field in which electrons remain on centerline where they will not contribute to the overall force on the plasma. This field shape has the effect of a rapidly diminishing field strength away from the throat of the thruster, a necessary side effect of the geometry.

Two settings were chosen: one at approximately 80 G centerline maximum strength, and one at 120 G. Field strengths were chosen so that, under conditions of full entrainment, the induced magnetic field at centerline would be approximately twice the bias field, forming a Field-Reversed Configuration (FRC) under ideal circumstances. While the FRC is not considered important to this particular study, it allows easier comparison to other RMF thrusters such as the ELF [57] which do claim field reversal.

#### 5.3.2.3 RMF antenna

Each RMF antenna is bent in the form of a saddle coil, with each loop on an opposite side of the cone. The antennas are bent such that each loop subtends an approximately 60° portion of the cone's cross section. The antennas themselves are formed from copper tubing to minimize their circuit resistance given skin depth considerations and allow for water cooling during operation. The two antennas are clocked 90° relative to each other so that, when fed oscillating currents which are offset 90°, a rotating magnetic field of relatively uniform magnitude is formed. An example field map of the RMF, measured at approximately 10 cm downstream of the cone's throat and scaled to reflect a peak current of 2 kA, is shown in Figure 5.5. We measured this by running DC current through each antenna individually, then generating a map using Hall effect probe measurements. The resulting fields were then superposed on each other to verify rotation.

#### 5.3.2.4 Pre-ionizer

A pre-ionization source is a necessary component to the operation of the RMF thruster. This provides the seed plasma necessary for facilitating the RMF spin up. For this design, we used a $LaB_6$ hollow cathode operating with Xenon as the propellant. We note that in a more mature device, an ionization scheme would be chosen which does not require a noble gas so

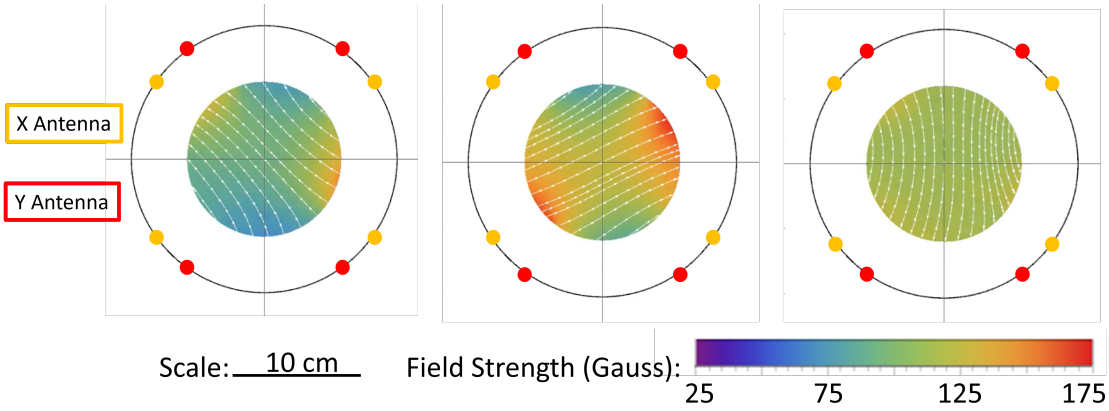


Figure 5.5: Map of RMF measured approximately 10 cm downstream of the cone's throat at three instants throughout a cycle to illustrate rotation. Maps correspond to peak antenna currents of 2 kA.

that the thruster can be tested on ISRU propellant options. However, lab design heritage and expertise made the choice of hollow cathode easiest to work with, and our research interest is in the acceleration mechanism rather than the design of an inductive pre-ionizer. The cathode is able to form a discharge of 20 A to the steel anode structure immediately surrounding it and operates with 15 sccm Xe of flow. For flow conditions requiring more than 15 sccm, a secondary neutral injection tube was used.

#### 5.3.2.5 Gas injection

The neutral injection tube, which can be seen around the rim of the thruster mouth in Figure 5.10, is formed from two concentric steel tubes bent into a circle. Propellant flows from the inner tube to the outer through small holes to ensure even pressure throughout the body of the outer layer. Holes in the outer tube direct flow upstream toward the thruster's throat to maximize residence time of neutral gas inside the cone and attempt to direct gas toward the cone's outer walls, where the effect of the RMF will be felt most strongly.

### 5.3.3 Power supply

To supply the necessary high current pulses to the RMF antennas, we collaborated with Eagle Harbor Technologies to develop a power-processing unit (PPU). Figure 5.6 shows a simplified circuit diagram of the PPU. Tuning capacitor banks were installed near the thruster in the vacuum chamber to create a series resonant LC circuit with the antenna as the inductor. This circuit is then pulsed at resonance using an H-bridge with dual-IGBT switches backed by a larger capacitor bank, which is in turn connected to a DC power supply.

This setup has the advantage of generating current pulses whose amplitude is limited only by the real resistance of the circuit, though a tuning procedure must be carried out to ensure the pulses are sent at the resonant frequency. This supply is able to deliver approximately 5 kW of power combined to both antennas for a duration of 5 minutes to avoid any risk of overheating.

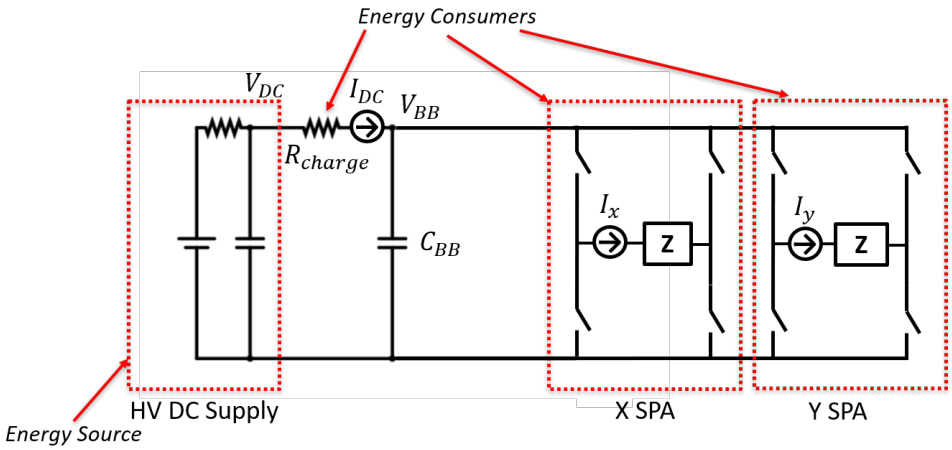


Figure 5.6: Simplified circuit diagram of the PPU. A DC supply provides power to a large backing capacitor bank, which is used along with an H brige to send pulses of energy into LC tanks formed from each antenna and an accompanying tuning capacitor bank.

## 5.4 Thruster Operation

In this section we present the qualitative observations made regarding RMFv2 thruster operation before moving on to quantitative measurements of performance and induced magnetic fields in the following two sections. We identity two main observations of interest: plume propagation and current waveform behavior.

### 5.4.1 Plume Propagation

Fig. 5.7 shows selected frames from high speed video depicting the evolution of RMF shots from the side of the thruster. The frame rate is at 50 kHz, and we depict three operating conditions shots to illustrate the similarities and differences in behavior between setpoints. All cases show the formation of some sort of pulsed plasma ball structure, which develops in the upstream region just outside the mouth of the thruster cone. The plasma structure moves away from the thruster, and in the moderate flow cases appears to detach and continue to move downstream. In the low flow cases, up to 30 sccm, a secondary shot begins to form

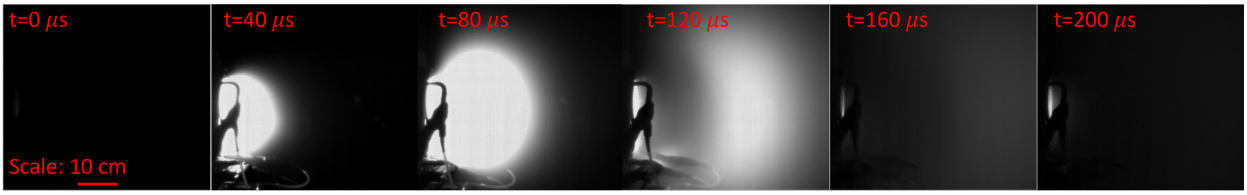


(a)

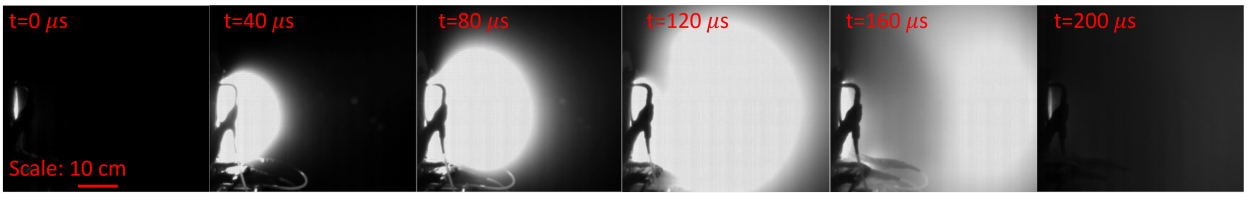


(b)

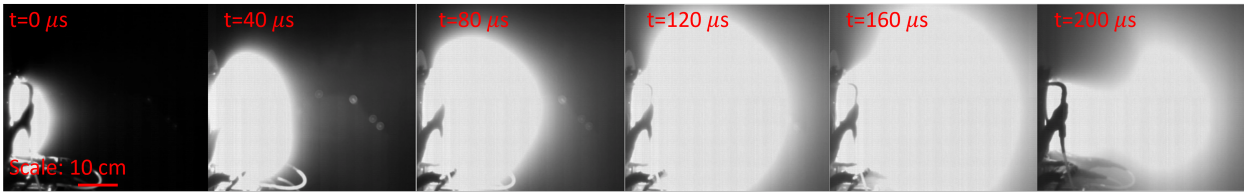


(c)

Figure 5.7: High speed video of three representative plasma shots: a) 30 sccm Xe, 80 G Bias, 1.9 kA Antenna current, b) 45 sccm Xe, 80 G Bias, 1.9 kA Antenna current, c) 200 sccm Xe, 120 G Bias, 1.9 kA Antenna current.

towards the end of the pulse after the first has been accelerated, as seen in the 200 $\mu$s timestamp in Figure 5.7a. At higher flow rates such as 45 and 60 sccm, no secondary slug can be seen. At the extreme 200 sccm case, no plasma structure detachment occurs, and the plasma has not finished ejection by the end of the pulse.

The formation and detachment of the plasma structure suggests that field reversal is occuring, in which the magnetic field induced by the RMF is strong enough in magnitude relative to the bias magnetic field to reverse the direction of the overall magnetic field near centerline. This has the effect of creating a plasma structure surrounded by a separatrix. If this is the case, then there are indeed azimuthal currents being driven in the plasma which are interacting with the bias field to produce acceleration.

Figure 5.8 shows a time-averaged image of the thruster firing. The image was acquired by setting the exposure on a DSLR camera to 10 seconds. Setting the exposure to this length shows distinct structures in the plume. The brightest region appears to be a time-averaged ball of plasma residing near the mouth of the thruster which shows good collimation. Outside it is a weaker region of illumination, likely caused by the expansion of the plasma slugs as

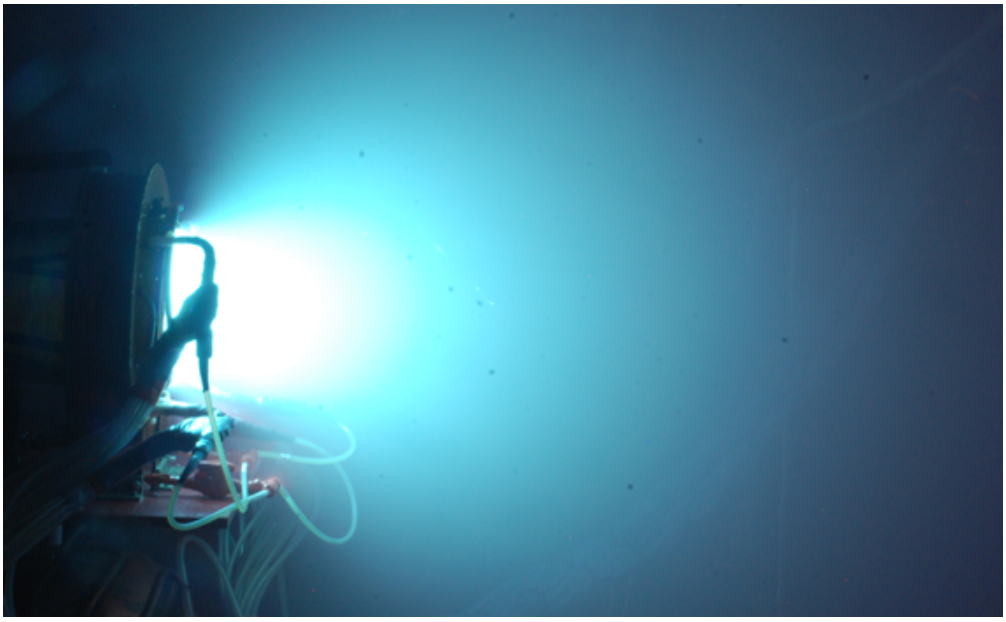

Figure 5.8: 10 s exposure image of RMFv2 thruster operating at the 45 sccm Xe flow, 1.95 kA peak antenna curent, 120 G centerline bias field condition at 75 Hz repetition rate.

they move downstream. Outside all of this is a much weaker region, probably caused by electrons not captured in the plasma structure which remain attached to the bias magnetic field lines.

### 5.4.2 Current Waveforms

Antenna current waveforms are critical for computing the coupling efficiency as separate from the total efficiency, as discussed in Chapter 4. Figure 5.9 shows an example vacuum and plasma waveform.

The blue trace, labelled as the Vacuum Shot, was taken with no plasma present. It can be seen to ramp up, then achieve some steady amplitude for the majority of the pulse. This shape is indicative of a series LC circuit being driven at its resonant frequency. In the case of a perfect match between the resonant frequency and the driving frequency, the amplitude is limited only by the real resistance in the circuit. To attempt to match the resonant frequency as best as possible, we employ a tuning procedure before thruster operation. Each antenna is driven at a range of frequencies with a range of phase delays between X and Y antenna driving signals to ensure the maximum equal amplitude on both antennas with a 90° phase delay between the current waveforms. As a result, each antenna is actually driven slightly off its resonance to ensure equal amplitude between the X and Y antennas.

In the plasma-loaded shot, the waveform amplitude can be seen to rise faster than the

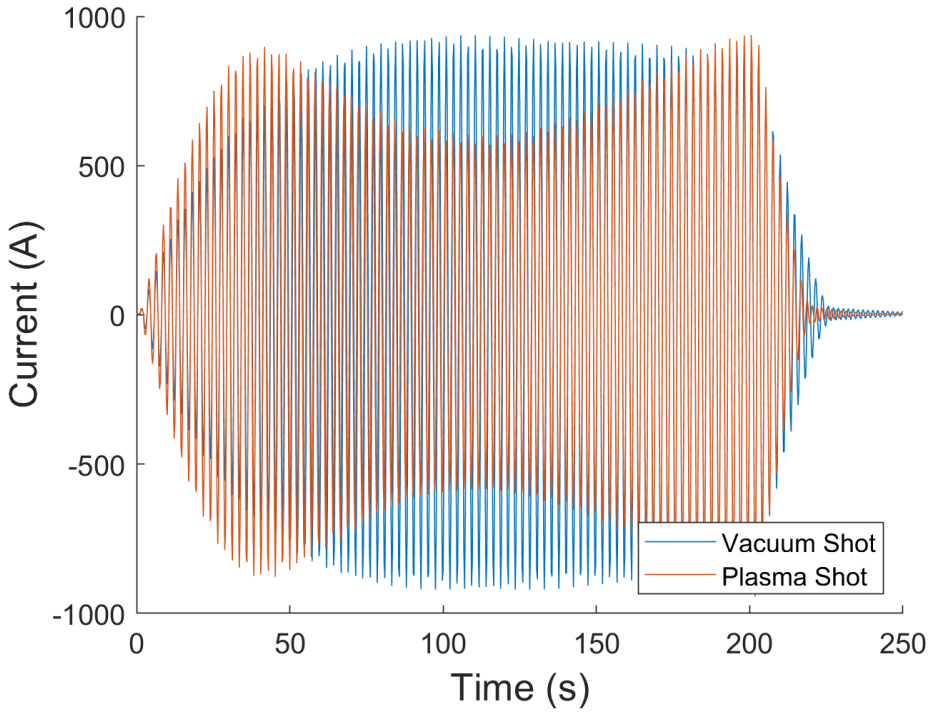


Figure 5.9: Example vacuum and antenna current traces for the 1.95 kA peak current setting. The plasma shot is taken at the 45 sccm Xe flow rate, 120 G centerline bias field condition.

vacuum shot. The primary reason for this is that, due to the plasma loading on the circuit, we must apply a higher voltage to achieve the same peak current as in the vacuum shot case. Further along in the pulse, the plasma loading becomes more apparent as the waveform takes on a "dogbone" shape. Because the amplitude of the pulse is limited by the difference between the pulse frequency and the resonant frequency of the antennas, the plasma's presence serves to dramatically reduce the current amplitude by changing the effective inductance of the antennas. While plasma is present and highly coupled to the antennas, amplitude is lowered. This can be illustrated by comparing the time steps in Figure 5.7b to the waveform in Figure 5.9, as they are both taken at the same operating conditions. It is seen that in the images where a large plasma discharge is present, the amplitude is less.

## 5.5 Thrust Stand Results

We show the results of our direct performance study here. This begins with a description of the operating conditions employed in the experimental campaign. We then present the coupling efficiencies observed across these conditions before moving on to those performance metrics which are measured by the thrust stand: thrust, specific impulse, and efficiency.

### 5.5.1 Operating Conditions

Keeping in mind the power limitations of the PPU and the thruster geometry, we operated the test article at a range of conditions, varying bias field magnitude (but not shape), propellant flow rate, and RMF magnitude. For all conditions, a repetition rate of 75 Hz with a pulse duration of 200 $\mu$s was chosen to maximize power to the thruster while avoiding thermal concerns in the PPU. We used bias fields of 80 G and 120G, flow rates of 15, 30, 45, and 60 sccm Xe, and peak antenna currents of 1.5, 1.7, and 1.95 kA. These flow rates were determined based on the penetration condition analysis presented in Section 5.3.1. The bias field strengths were chosen to approximately equal the fields anticipated to be induced by the azimuthal current in the plasma. Antenna currents were chosen with the maximum setpoint limited by the PPU constraints. We also added a 200 sccm Xe, 120 G, 1.7 kA setpoint to briefly explore the very high flow regime as time permitted.

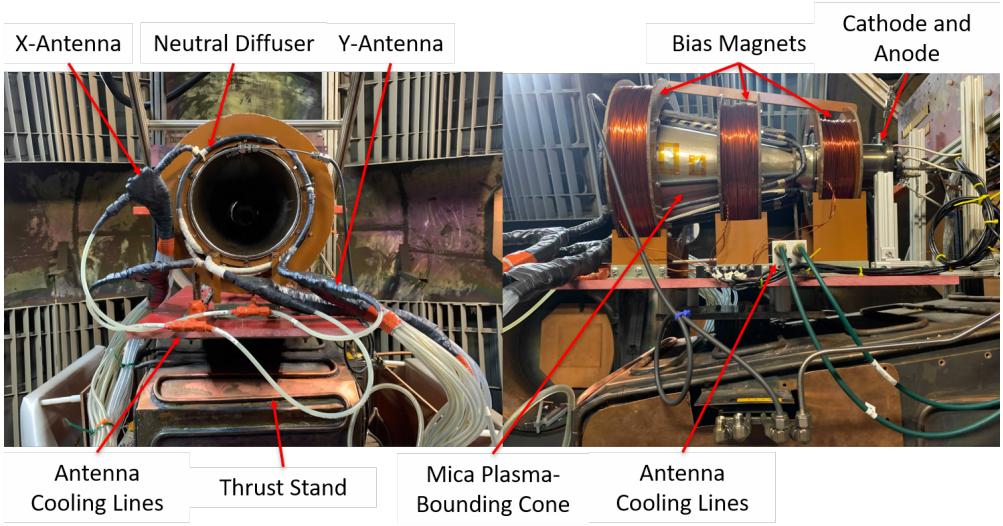


Figure 5.10: Close view of the RMFv2 mounted on the thrust stand inside LVTF. Salient features annotated.

### 5.5.2 Coupling Efficiencies

Figure 5.11a shows the coupling efficiency across all points plotted with respect to flow rate. While there exists a spread in coupling efficiency due to the range of operational parameters investigated, the trend with flow rate is by far the strongest. Recalling the analysis culminating in Equation 5.18, we should expect that increased flow rate will yield a higher coupling efficiency given a certain energy input and assuming penetration. With a higher energy required for current spin-up, more energy can be added to the plasma before

synchronous rotation between the electrons and the RMF is achieved, leading to reduced loading on the antennas. However, turning to Figure 5.11b, we find that the specific energy successfully coupled to the plasma appears to be roughly constant with the flow rate. This suggests that the argument that coupling is limited by the maximum spinup energy is likely not true, since such scaling should result in an increasing trend in Figure 5.11b.

Trends aside, the magnitude of the coupling efficiency peaks at approximately 50% for the conditions investigated. This is significantly higher than the 20% coupling efficiency estimated which was used to guide Figure 5.2. Such a difference would impact the design by allowing a larger cone size at a given propellant flow rate, since more energy can be available for the propellant. From the perspective of examining paths for future work, we can also be satisfied that we are at least coupling a significant amount of energy to the plasma that the acceleration mechanisms can be studied.

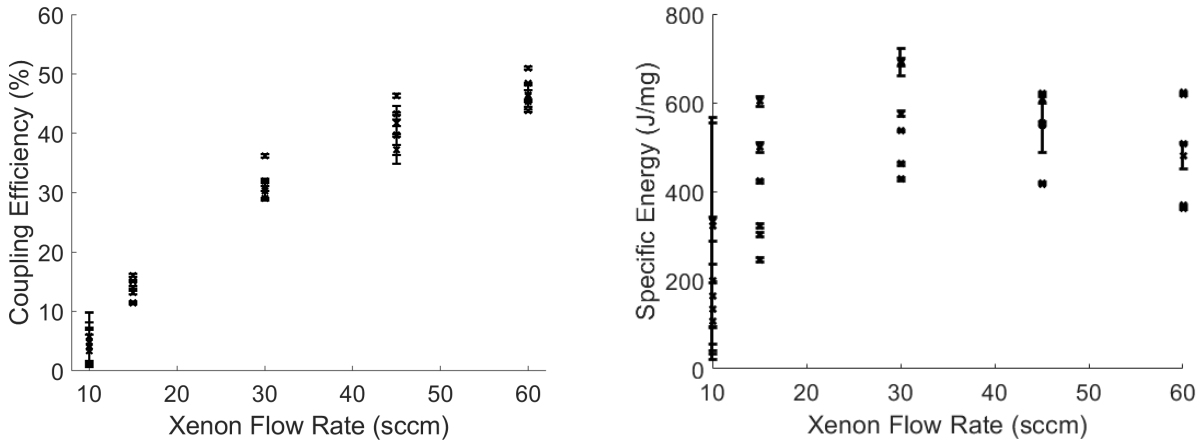


(a) (b)

Figure 5.11: a) Coupling efficiencies across all measurements. b) Successfully coupled specific energy versus flow rate across all measurements

### 5.5.3 Thrust Stand Measurements

For the rest of the data, we turn to thrust stand measurements, beginning with average thrust across the entire duty cycle, as depicted in Figure 5.12. Keeping in mind that the power levels used to generate these data were between approximately 3 and 4 kW, we recognize that the PEPL RMFv2 does not compete with state of the art electric propulsion at this point. That being said, we wish to highlight that these are the first measurements of their kind to be published to our knowledge. As such, they represent an important step forward in the research of the RMF thruster regardless of absolute performance.

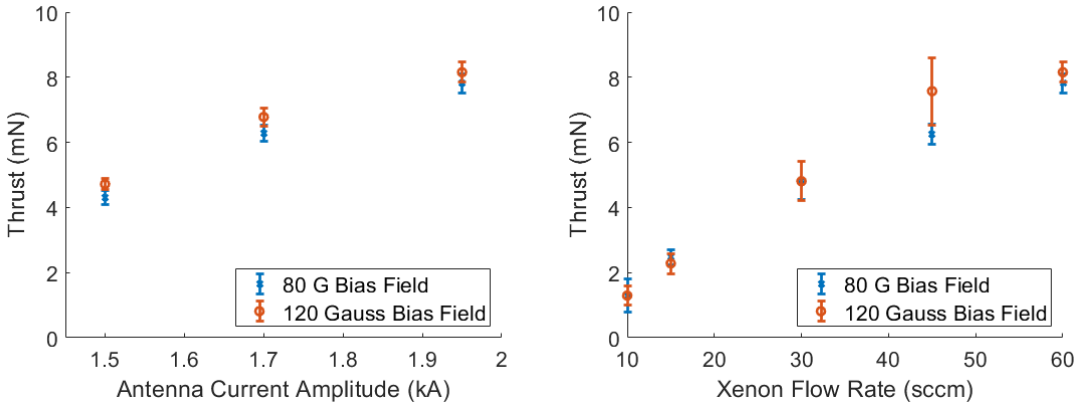


Figure 5.12: Average thrust values (including dead space in the 1.5% duty cycle) as measured from the thrust stand for 200$\mu$s pulses at a 75 Hz repetition rate: a) Flow rate fixed at 60 sccm Xe, b) Antenna current fixed at 1.95 kA

We can see several trends in the thrust measurements. First, increasing antenna current amplitude monotonically increases the thrust level from approximately 4.5 mN at the 1.5 kA condition to 8 mN at the full 1.95 kA condition. To first order, the increase in thrust with current is not expected using the Blevin and Thonemann current drive model which was employed in the design of this thruster. Indeed, we would expect these trends to be relatively flat since entrainment of electrons under those assumptions only depends on the frequency of the RMF, which is constant. However, this observed trend either suggests that other effects may be at play improving the acceleration process with current or that this current drive model does not properly apply in this regime. Unexpected effects might include improved penetration or improved ionization. We return to a discussion of the physical underpinnings of these trends in Section 5.6.

The magnetic field has a slight effect of increasing thrust across most flow rates and antenna currents. Eq. 2.34 does suggest that increasing magnetic field should increase thrust, but a much smaller increase is seen than what would be proportional to the increase in field strength. If Eq. 2.34 is indeed correct to describe this device, this would suggest that the self-field induced directly by the plasma currents is dominating and has thus effectively cancelled out the bias magnetic field. However, it is also possible that other undesirable effects such as heating are dominating the acceleration of the plasma over Lorentz force interaction. Such heating-based acceleration—specifically, the force associated with electron pressure at the walls of the thruster—would not depend on the bias field. Indeed, we might expect them to be enhanced if the self-field has overcome the bias field everywhere resulting in poor

confinement.

These averaged thrust measurements, while useful in that we can identify trends and scaling by comparing tests at the same repetition rate and pulse width, are in some sense artificially low due to the low duty cycle. In practice, a thruster will be operated at much higher repetition rates or employ puff valves to limit propellant waste between cycles. However, we can leverage the process discussed in Section 4.2 to produce 'per-pulse' measurements of efficiency and specific impulse.

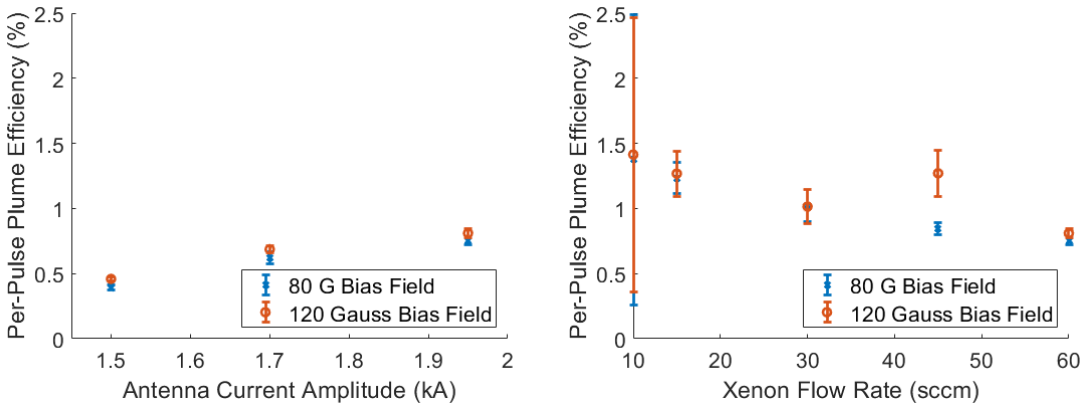


Figure 5.13: Per-pulse plume efficiencies: a) Flow rate fixed at 45 sccm Xe, b) Antenna current fixed at 1.95 kA

Figure 5.13 shows the 'per-pulse' plume efficiency, defined as $\eta_{plume} = \eta_m \eta_d \eta_p$ by the framework derived in Eq. 2.35 trends with both antenna current and flow rate. The maximum magnitude of the plume efficiency increases with antenna current, achieving a maximum value of 1.3%. In the framework of the established current drive theory by which this thruster was designed, the distinct upward trend with antenna current amplitude might be attributed to improvements in penetration depth. In turn, the low value of the maximum achieved efficiency indicates we are not achieving high penetration even at our maximum current. On the other hand, higher current amplitudes are also associated with higher energy per pulse because the backing capacitor bank must be charged to a higher voltage, and thus release more energy per driving pulse, to achieve the higher currents. The increase in energy per pulse could be obscuring the true trend in this case. At a fixed antenna current, increasing flow rate serves to slightly decrease the per-shot plume efficiency, as seen in Figure 5.13b. This could be related to the specific energy added to the plasma, which would decrease as flow is increased at a field antenna current. Another explanation is reduced penetration as the flow is increased. If instead the updated current drive model applies, these trends are not

unexpected. Increased antenna current amplitude would be associated with better electron entrainment and therefore better able to couple energy into the plasma.

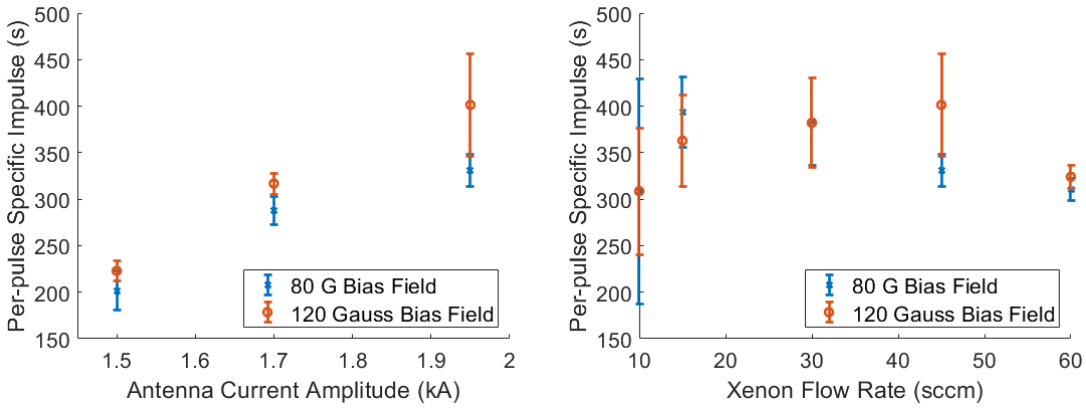


Figure 5.14: 'Per-pulse' specific impulse values referring to the per-shot specific impulse rather than a time-averaged value: a) Flow rate fixed at 45 sccm Xe, b) Antenna current fixed at 1.95 kA

Per-pulse specific impulse can also be extracted from the thrust data, which we present in Figure 5.14, again separated between trends with antenna current and flow rate. Per-shot specific impulse can be seen to reach a peak value of approximately 400 s at the 45 sccm, 1.95 kA antenna current, 120 G bias field condition. Figure 5.14a shows a clear monotonic increase in specific impulse with antenna current amplitude. This is likely due to the same arguments that contribute to the increased thrust with antenna current at fixed flow. Also similar to thrust trends, we see that the 120 G case yields higher specific impulse than the 80 G case at fixed flow, likely due to the Lorentz force increasing with the strength of the bias field, resulting in greater impulse per shot. However, the increase is again not proportional to the increase in field strength. Trends are less clear with the flow rate, however, although it appears that the specific impulse peaks at a certain flow rate given a fixed antenna current. This could be due to penetration concerns, where full penetration throughout the pulse is not achieved in the 60 sccm, 1.95 kA case.

Next we can examine briefly the effect of changing pulse length from 100 $\mu$s to 200 $\mu$s in Fig. 5.15. Fig. 5.15a shows the 'per-shot' efficiency discussed elsewhere in this Section, while Fig. 5.15b shows the efficiency including the wasted mass while the RMF is not energized. Opposite trends are seen for each plot. One explanation for improved per-shot efficiency with pulse length which is discussed in greater detail for the RMFv3 thruster in Chapter 7 is that the RMF is unable to fully ionize and couple to the propellant for the very short pulse

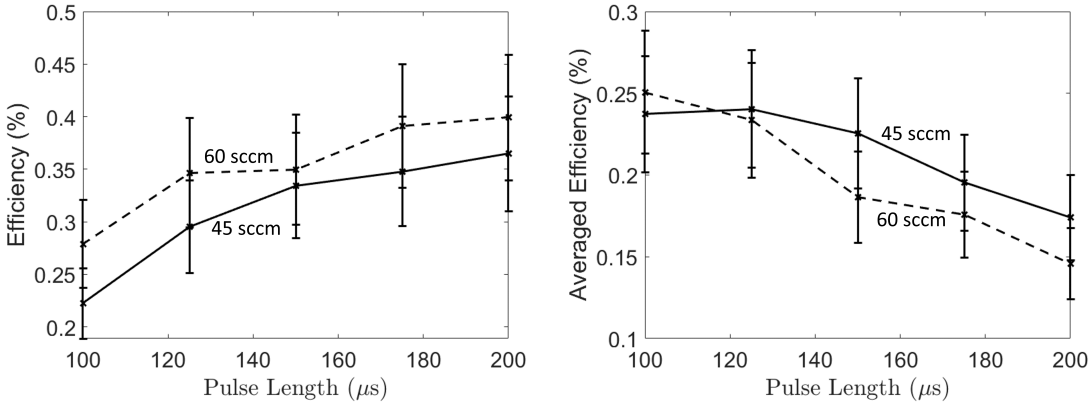


(a) (b)

Figure 5.15: Trends with pulse length for 45 and 60 sccm at 180 G bias strength. a) Per-shot efficiency as shown in the rest of the section. b) Averaged efficiency including wasted mass between shots

lengths. This is because it takes a certain amount of time for ionization to occur. If the dip in amplitude in the waveform shown in Fig. 5.9 is indicative of plasma coupling, then it took as much as $\sim 75\mu$s for coupling to occur for that case, for example. Meanwhile, because the power is fixed, shorter pulses are associated with higher repetition rate. This may correspond to less propellant being wasted as the repetition rate approaches the characteristic gas refill rate.

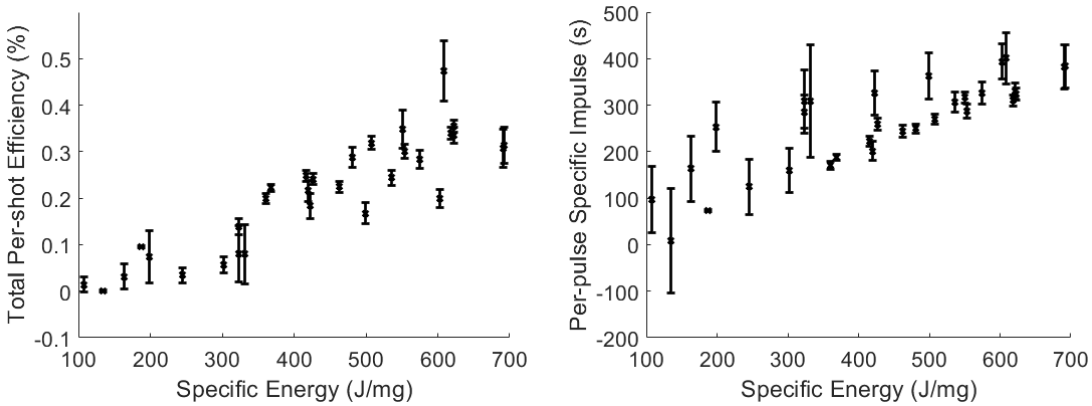


(a) (b)

Figure 5.16: Trends with specific energy across all data: a) Total efficiency, b) Specific impulse

Finally, normalizing by the propellant mass per shot, we can compute quantities as func-

tions of the specific energy across all test cases to produce the plots in Figure 5.16. While ultimately the total efficiency is low, the increasing trend with specific energy gives us optimism for the power scaling capabilities of this device. Indeed, both cases show positive trends, with higher specific energy leading to better performance. This is an important result because it demonstrates in-family behavior with other IPPTs [19], and thus shows that our design is on the right path.

## 5.6 Discussion

In this section, we discuss the results in the context of our present understanding of thruster behavior. We first connect the results back to presently understood scaling laws. Second, we discuss how these results could be used to improve thruster performance. Last, we consider the broader implications for the technology moving forward.

#### 5.6.0.1 Relating Trends in Data to Design Scaling Laws

One of the clearest trends seen in the data in Section 6.4.4 is an increase in performance with antenna current across every measurement. According to the analysis presented in Section 5.3, the RMF is well within the penetration regime for every case since a factor of 10 margin was applied to produce Figure 5.2. Therefore, the positive scaling with antenna current could be simply due to increased energy per pulse being added to the plasma; in the event that current spin-up is not instantaneous, additional energy could be required to achieve synchronous rotation, allowing for deposition of energy beyond the first order estimates. Alternatively, it is possible that increased penetration does indeed play a role here. Examining a typical antenna current waveform such as in Figure 5.9, we see that the plasma-loaded amplitude is nearly a factor of 2 lower than the nominal pulse amplitude. Considering the relatively loose condition enforced by the inequality of Equation 5.10, it is reasonable that penetration is lost mid-pulse during the part of the cycle in which it would be most desired, the heavily-loaded middle of the pulse. Further, the penetration condition used to design the thruster assumes a uniform radial density profile which may not be the case in reality and which may make penetration more difficult than expected.

Besides the penetration condition, the other scaling law used to develop the RMFv2's design was the commensurate energy condition, that the inductive energy capable of being stored in the plasma has a limit which depends on the plasma density distribution and the RMF frequency. If this scaling holds, we should observe a maximum specific energy which can be added to the plasma. At first glance, this is supported by the increasing coupling efficiency as more propellant is added to the thruster, as Figure 5.11a) shows. Equation 5.18, which

describes the scaling which motivates the spinup energy argument, shows that a quadratic scaling between spinup energy and mass flow rate should be expected, and thus a quadratic relationship between the specific energy and the mass flow rate as well. However, the data in Figure 5.11b) conflicts with this idea, showing roughly constant specific energy as mass flow rate is increased. Therefore, we expect that penetration is likely to be the driving factor behind the increase in coupling efficiency.

Given that both major scaling laws do not seem to be supported by the data, the mechanism of acceleration is called into question. The magnitudes of the specific impulses which Figure 5.14 shows also serve to call into question the scaling of this device because these low specific impulses are in the regime accessible to a thermal device. Without additional data to verify the azimuthal current drive mechanism is performing successfully, and in light of the disagreement with these putative scaling laws discussed above, we recognize the possibility that we are simply heating the plasma rather than driving acceleration via the Lorentz force. If this is the case, it also explains the relatively weak scaling seen with the bias magnetic field strength, which our scaling laws predict to be more significant.

#### 5.6.0.2 Implications for improving thruster performance

While the performance data gathered is valuable in that they represent the first measurements of their kind, overall performance remains low. By examining the trends presented by the data, we can draw conclusions regarding how to improve thruster performance even before a full performance model is developed and validated.

At the level of analysis afforded us by the data we have, our phenomenological efficiency model splits losses into coupling losses and plume losses, with coupling efficiency peaking around 50% and per-shot plume efficiency peaking at approximately 1.5%. Given the wide gap between these two numbers and the low value of the plume efficiency, immediate research towards improving thruster performance should focus on plume losses. While Figure 5.13b does not show clear trends with flow rate, 5.13a indicates improvement in plume efficiency with antenna current, and Figure 5.16a shows improvement with specific energy. This suggests that we may be operating at antenna currents that are dramatically too low. With these trends, we can conjecture that the penetration condition used to design the RMFv2 is perhaps too lax, especially in light of the reduced antenna current amplitude during the plasma-loaded portion of the pulse.

Unfortunately, exploration of this higher energy regime proves difficult given present PPU limitations. The chief limitation encountered during testing was the power which could be output from the PPU. These upper bounds on output power, which constrain energy per pulse, pulse rate, and total run time, made the collection of reliable data more difficult.

Pulse rate limits made thrust measurement more challenging, as the very low 1.5% duty cycle meant that the actual thrust signal is much smaller than it could be. Increasing the duty cycle to the approximate limits set forth by the assumption of steady-state diffusion throughout the cone would involve a dramatic increase in thrust signal, and therefore more confidence in the results. This would also eliminate the need for the average to per-pulse conversion process, which introduces error due to uncertainty in the true mass of a given plasma shot.

Energy per pulse limits meanwhile constrain our investigation into higher specific powers, which appear to be a promising area of further study based on the upward trends for per-pulse plume efficiency. Attempting to reach those regions of parameter space with the PPU as-is would require dropping the repetition rate more than commensurately due to the nature of the thermal limitations, resulting in even lower duty cycle and further challenges to thrust data resolution.

Challenges aside, further research into the causes of the low plume efficiency is warranted. An understanding of the physics behind why the performance is low could point to solutions besides increase in power level. To gain this understanding, we need more detailed data of the plasma behavior. This will include azimuthal current density levels, which will give information regarding penetration status, electron densities which will tell us if full ionization is being achieved, plasma temperature measurements to determine if power is being wasted heating the gas, and others.

#### 5.6.0.3 Broader Implications for the Technology

The most significant conclusion to be drawn from the results presented above is that the PEPL RMFv2 is indeed functional as a test unit which will allow us to study the acceleration mechanisms further in subsequent tests, and for which we now have a grasp on baseline performance. Additionally, the presence of these results demonstrates that the basic concepts used to produce the thruster's design are valid, or at least on the right track. We are consistently able to explain trends in the data by referencing the two main criteria used in the thruster's design, RMF penetration and plasma inductive energy storage. Because of the low overall performance relative to state of the art thrusters, it is likely the case that the values used in the RMFv2's design are not optimal, but trends agree with analysis.

The overall low performance of the RMFv2 allows us to conclude additionally that this thruster is not yet competitive with more mature technologies such as Hall thrusters, gridded ion thrusters, or even other (higher TRL) pulsed devices. However, inefficient thruster operation at this point should not lead to the conclusion that the RMF thruster is necessarily an ineffective technology, which owes to the device's relative infancy. At this point, we still

lack a validated comprehensive model of RMF thruster operation from which to extract convincing performance upper bounds. It was one of the goals of this work to establish a baseline for guiding development of such a model, which will then allow for such overarching conclusions regarding the technology.

With this in mind, these results constitute the first published nonzero direct measurements of thrust in an RMF thruster that we are aware of, and the existence of a working, freestanding test unit which will allow for further investigation of thruster physics. Additionally, the relatively high coupling efficiencies measured show that energy is successfully being transmitted into the plasma. This suggest that the goal of designing an RMF antenna which successfully transfers power to the plasma has been reached, allowing for future research to focus on areas of more acute weakness. The low plume efficiencies measured constitute this weakness, and efforts are warranted to investigate and address the cause.

## 5.7 Conclusions

In this chapter we have presented the design and baseline performance maesurements for the RMFv2 thruster. This began with a brief discussion for the motivation of the thruster with a description of the RMFv1, which followed with a first principles analysis of how the thruster ought to be designed assuming the established RMF current drive theory. After this, thruster qualitative behavior was described before leading into the results of the baseline performance measurements. The chief trend uncovered during this investigation was a positive efficiency scaling with the specific energy into the propellant, but that overall performance is very low, peaking at approximately 0.5%. This naturally begs the question of why efficiency is poor, which we will investigate in the next chapter.

# CHAPTER 6

# The PEPL RMFv2 Thruster: Understanding Performance Limitations

## 6.1 Introduction

In light of the poor performance measured for the RMFv2 thruster, an investigation is warranted to determine the root causes of the low efficiency. Specifically, desire to learn two aspects of thruster behavior. First, the dominant loss mechanisms must be determined in order to identify strategies to avoid losing power to non-thrust modes. Second, we must determine whether the RMF current drive is successful and whether we produce FRC plasmoids with the RMFv2 thruster as we would ideally expect. To that end, this Chapter is organized in the following way. We first discuss the results of the efficiency analysis whose methods are outside the realm of this work but whose conclusions are necessary to motivate subsequent efforts on this device. We then present the results of the inductive probing experiments which aimed to resolve the efficacy of the RMF current drive. Next, we present an analysis which seeks to extrapolate pulsed-mode results to the CW-mode (i.e. 100 % duty cycle RMF operation), which is one option identified to possibly increase efficiency. These results are then discussed within the context of improving thruster efficiency.

## 6.2 Efficiency Analysis

Further insight into thruster behavior can be gained by examining the plasma properties during a thruster pulse to identify the chief loss mechanisms. Much of the experimental technique and analysis lies outside the scope of this work and is discussed in detail in Ref. [77]. However, we briefly summarize the results here to help motivate the shift to CW-mode explored in the RMFv3 thruster.

Fig. 6.1a shows a breakdown of efficiency modes for a typical operating condition for the

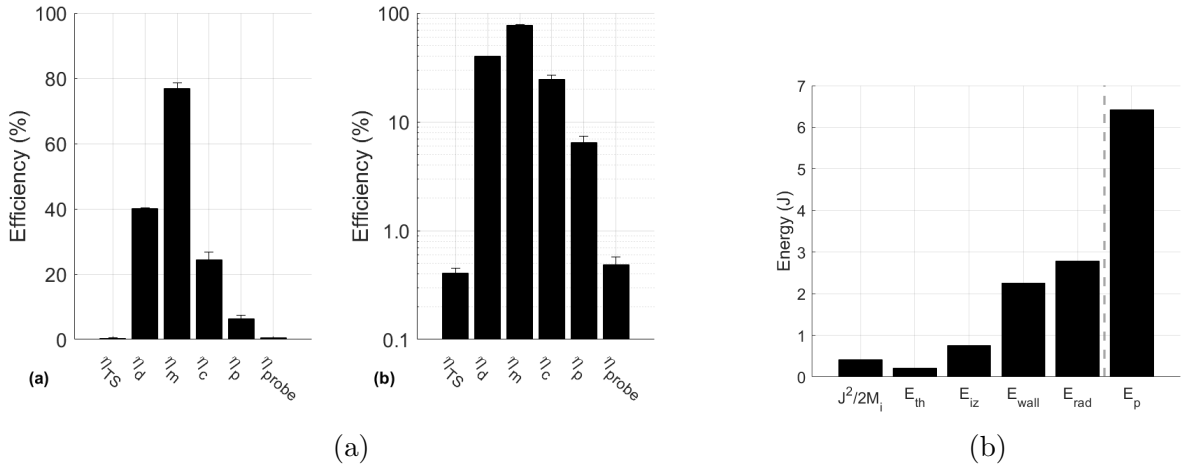


(a) (b)

Figure 6.1: a) Breakdown of efficiency modes for the RMFv2 thruster operating at 2 kA peak-to-peak RMF current, 180 sccm xe, and 125 $\mu$s pulse duration. Left plot is linear y-axis, right plot has a logarithmic y-axis to resolve greater detail. b) Energy distributed to various modes in the plasma for the same condition.

RMFv2. We wish to highlight two key takaways from this figure. First, we note that the probe-calculated efficiency by this phenomenological model presented in Chapter 2 correctly matches the thrust stand measured efficiency ($\eta_{TS}$ in Fig. 6.1a). This provides some evidence that these probe measurements are accurate. Second, the plasma efficiency $\eta_p$ has by far the greatest impact on the total efficiency of the thruster. It is seem to be a full order of magnitude lower than the coupling efficiency, the next lowest efficiency mode. Because the plasma efficiency represents how effectively the energy which has been coupled into the plasma is converted into kinetic energy, we must investigate individual loss mechanisms to determine where the power has been wasted.

Five channels for energy deposition are considered in the analysis leading to Fig. 6.1b. The first, $\frac{J^2}{2M_i}$ is the kinetic energy imparted to the plasma over the course of a pulse. $E_{th}$ refers to the thermal energy associated with ions in the plume. This energy mode and the ionization energy $E_{iz}$ can be thought of as a frozen flow loss. Next is wall loss $E_{wall}$ which refers to the power lost when electrons accelerate across the sheath potential to the wall of the discharge chamber. Finally $E_{rad}$ refers to excitation radiation losses. The power lost to the walls and to radiation is given later in this document in Eqs. 6.27 and 6.25. Significantly, we see that both these dominant loss mechanisms scale with density, with radiation increasing quadratically.

## 6.3 Inductive Probing

### 6.3.1 Operating Condition

The RMF thruster has several operational variables which can be adjusted parametrically to change thruster behavior without any physical reconfiguration. For the measurements presented in this work, we operated the thruster at a steady flow rate of 45 sccm Xe, while the RMF was pulsed at 700 A RMS (2000 A peak-to-peak) for 125 $\mu$s pulses at a repetition rate of 155 Hz. The pre-pulse neutral density is estimated to be in the $n \approx 1 \times 10^{19}$ range, and at its peak plasma density has been measured at $n_e \approx 1 \times 10^{19}$ 1/m$^3$ with electron temperature peaking at $T_e \approx 9$ eV [87].

Fig. 6.2 shows the magnetic field streamlines and intensity in the thruster at 35 $\mu$s intervals. These field lines result from the superposition of the transient induced fields as measured by the two-axis Bdot probe with the steady bias magnetic field. Before approximately 70 $\mu$s, no measurable magnetic field is induced. This stems physically from the time required for the RMF current to first reach peak amplitude, then ionize the propellant. At the 70 $\mu$s point, the magnetic field is rapidly induced and is strong enough to overcome the bias field near centerline. This results because the direction of RMF rotation was chosen to produce a downstream force when the azimuthal current interacts with the positive radial bias magnetic field. Because the magnitude of the induced field is strong enough to reverse the bias field at centerline but not at the thruster's edge, a separatrix forms. This provides evidence that a field-reversed configuration (FRC) plasmoid has been generated. Peak field strength for the induced magnetic field reaches ∼110 G at this 70 $\mu$s point. The FRC then translates downstream at a speed of ∼2000 m/s before exiting the cone and dispersing. We estimated this speed by tracking the center of the toroidal field structure where the field magnitude approaches zero.

### 6.3.2 Currents

Fig. 6.3 shows the RMF current and the evolution of the current density in the thruster over time, displayed at 35 $\mu$s intervals. Similar to the induced magnetic fields shown in Fig. 6.2, no current is induced until roughly the 70 $\mu$s mark, at which point the current rapidly rises and peaks at a value of ∼30 A/cm$^2$. After this time, the distribution in current density spreads axially and propagates downstream. We note that current is primarily driven at larger radial locations, which is consistent with our analysis from Chapter 2 suggesting that RMF electron entrainment should yield current linearly proportional to radius.

We show the total azimuthal current in Fig. 6.4 where we generated these plots by inte-

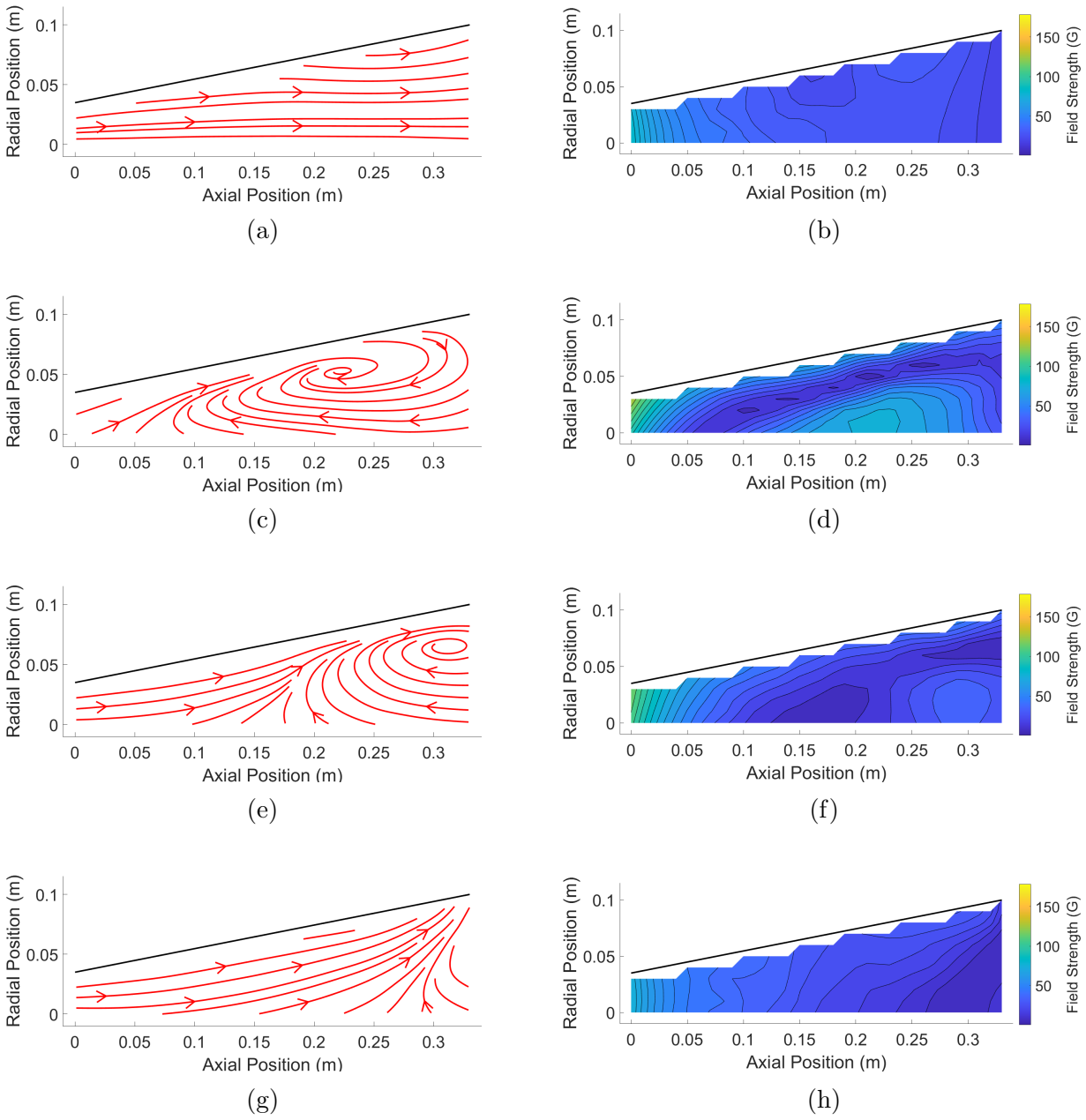


Figure 6.2: Magnetic field streamlines (left column) and magnitude (right column) at (a,b) 35 $\mu$s, (c,d) 70 $\mu$s, 105 (e,f) $\mu$s, and (g,h) 140 $\mu$s

grating over the current density in the volume following Eq. 4.14. For comparison, we also show the envelope of the RMF current extracted from the pulse waveform akin to that of Fig. 5.9. The uncertainty in the azimuthal current stems primarily from integration error from the Bdot measurement. In keeping with the technique discussed in Ref. [83], we estimated this uncertainty by assuming linear growth of integration error up to the maximum

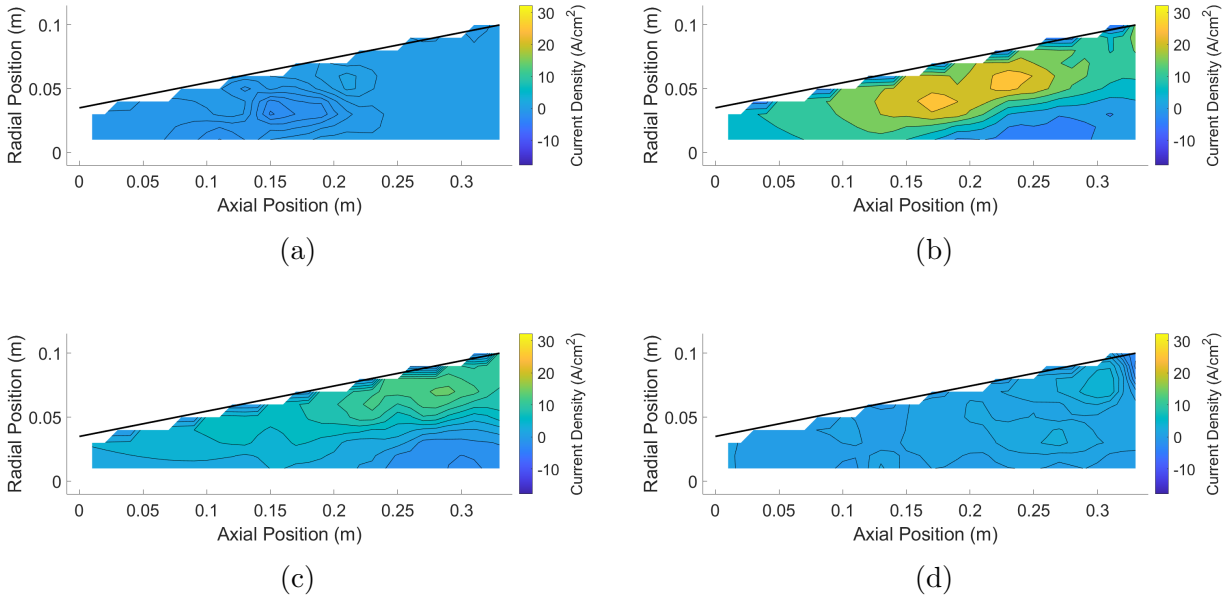


Figure 6.3: Induced current density in the RMF thruster at a) 35 $\mu$s, b) 70 $\mu$s, c) 105 $\mu$s, d) 140 $\mu$s into the 125 $\mu$s pulse.

value at the end of the pulse.

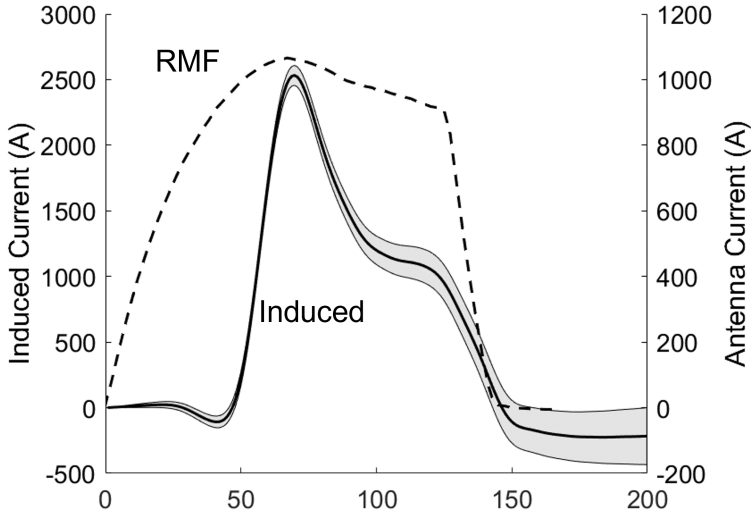


Figure 6.4: Total induced current in the RMF thruster as a function of time.

As can be seen, the induced current peaks at 2.5 kA at the 70 $\mu$s mark before decreasing to and remaining at 1.1 kA until the pulse ends at 125 $\mu$s. Comparing to the RMF antenna current envelope shown in the same plot, we see that the induced current does not begin to

rise until the RMF has ramped in amplitude for 70 $\mu$s. We believe this can be attributed to the fact that induced azimuthal current only onsets when the RMF has reached sufficient strength to cause a rapid ionization of the propellant. We note that both the RMF amplitude and induced current trend down after the peak in induced current. For the RMF, we attribute this trend to the presence of plasma altering the effective inductance and resistance of the antenna. For the azimuthal current, we explain this decrease by the reduction in plasma density in the thruster (Ref. [88]). We ascribe this loss of density to a combination of initial plasma ejection and recombination at the thruster walls.

We note here the total current decreases below zero at the end of the shot as well as just before the initial ionization event. We believe these events are caused by measurement error owing to the signal processing, interpolation, and integration involved in producing these plots rather than the existence of actual negative currents.

### 6.3.3 Forces

Figs. 6.5a and 6.5b display the forces resulting from the Lorentz interactions in the thruster. We estimate these from Eqns. 4.15 and 4.16 where we consider the different sources of magnetic field (self, bias, and structure) and the measured current densities (Fig. 6.3). Uncertainty in these plots stems from the integration error in both the current density and magnetic field measurements.

We first consider the individual contributions to force. For the self-field, $F_{self}$, we see the axial contribution is effectively zero at all times. This agrees with the physical intuition laid out in Chapter 2 that we expect that a system cannot accelerate its own center of mass. On the other hand, conservation of momentum does allow for the nonzero radial component observed. The positive sign indicates a tendency for the plasmoid to expand radially due to this interaction. The temporal profile of the bias force, $F_{bias}$, follows a qualitatively similar trend as the magnetic fields and currents (Figs. 6.2,6.4) in both axial and radial components. This force has near-zero magnitude until roughly 70 $\mu$s. At this point, which is coincident with enhanced ionization, current spin-up occurs, leading to enhanced bias force followed by a plateau until the pulse ends. As can be seen in Fig. 6.5a, the bias force is the primary acceleration mechanism in the first half of the pulse before its magnitude drops below that of the structure force. Meanwhile, Fig. 6.5b shows that the radial bias field causes the primary radial force throughout the duration of the pulse, providing strong compression.

The structure force, $F_{struct}$, exhibits its highest axial value after the bias force peaks at $\sim$ 125 $\mu$s when it then dominates the acceleration. We consider two possible explanations for the delay in the axial structure force as compared to the bias force. First, nonzero resistivity

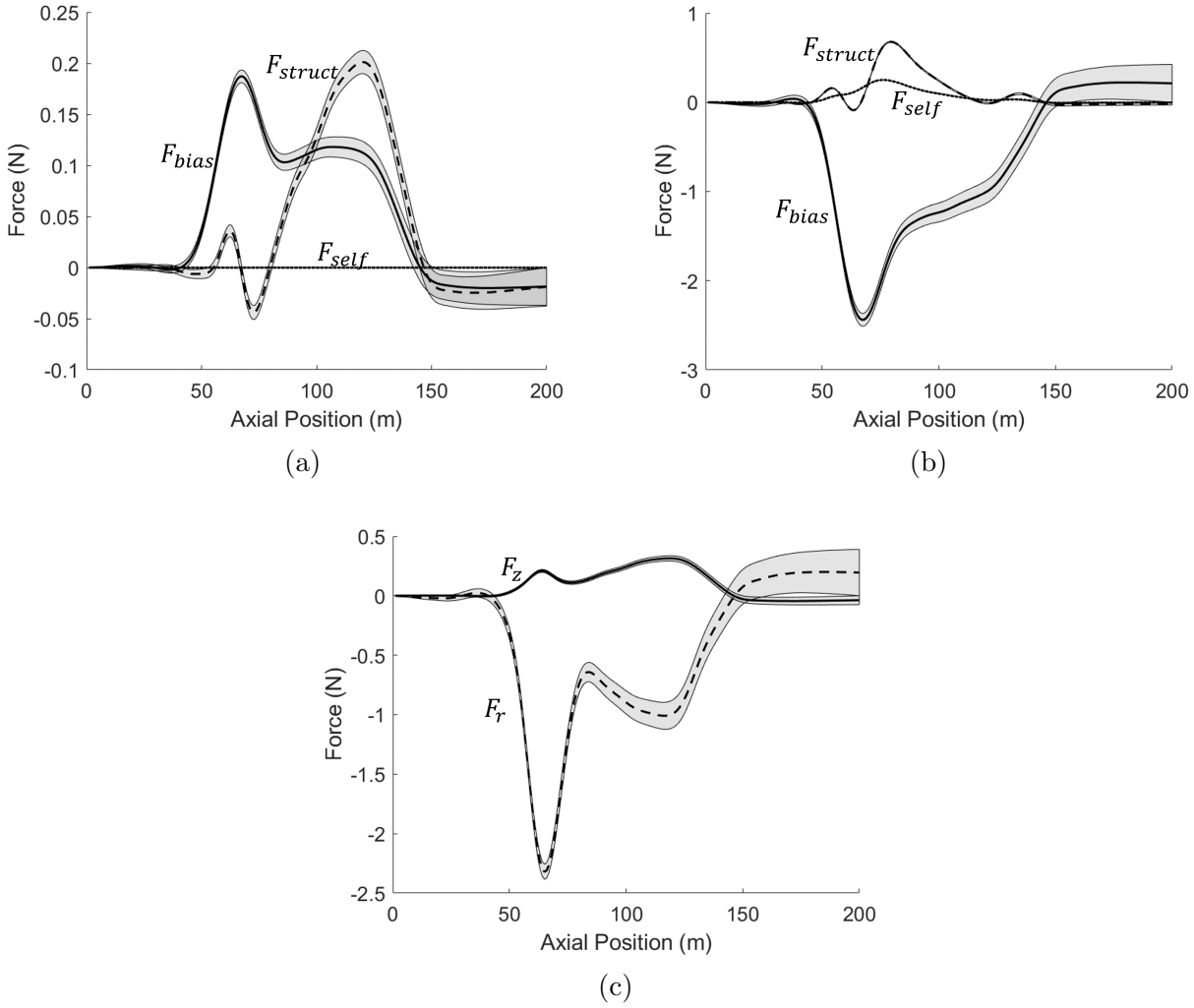


Figure 6.5: Lorentz force present throughout the RMF pulse broken down to a) axial contributions by magnetic field source, b) radial contributions by magnetic field source, and c) net axial versus net radial force.

in the structural elements could serve to add a time delay to the secondary induced currents and therefore the onset of the structure field. This time delay would be determined by the inductive time constant for each structure. Second, we note that the transient magnetic fields generated by coupled circuit elements are self-repelling. Thus, the force due to the structure field interaction would serve to push the plasma away from any coupled structure. In the case that the plasma current centroid initially forms upstream of a coupled structure, the resulting force would be directed upstream. The structure force subsequently would be balanced or even reversed by the summation of upstream and downstream interactions until the plasmoid could translate sufficiently downstream for the force to become net positive.

Indeed, this latter explanation may account for the initial negative structure force exhibited in Fig. 6.5a.

The highest radial value for structure acceleration peaks at ∼85 $\mu$s. Unlike the axial structure force, the radial component is primarily in the opposite direction of the radial force resulting from the interaction with the bias field. This is unexpected because the currents which induce the structure field should be in the same direction as those responsible for the bias field. This discrepancy may ultimately be a consequence of our limited experimental measurement domain. Because the structure field is calculated by subtracting the self field—itself calculated directly from measured plasma current—from the total field measurement, any currents in the plume outside the region of interrogation would be attributed to the structure rather than self field. We ultimately expect that if current measurements further downstream were taken, the radial self force would be greater, and the radial structure force would be primarily negative.

Fig. 6.5c shows the total radial and axial contributions to the force on the plasma in the thruster as a function of time. Because the two contributors to axial Lorentz force, the bias and structure forces, peak at different times, the total axial force remains relatively constant throughout the pulse. Meanwhile, the radial inward force is significantly stronger than the total axial thrust force, indicating high levels of compression in the plasma. This type of radial compression is anticipated in any FRC plasmoid and is a hallmark of this plasma structure [50]. Indeed, electron temperature and density measurements taken at the same operating conditions from Ref. [88] indicate electron thermal pressure to be of similar order of magnitude to the magnetic pressure. At the 100 $\mu$s timestep, for example, peak magnetic pressure, given by $P_{mag} = \frac{B^2}{2\mu_0}$, reaches ∼18 Pa, while thermal pressure at the same time and location is calculated to be $n_e k_B T_e = 12.8$ Pa. We note here that the various contributions to force do not return exactly to zero at the pulse end. This is a non-physical phenomenon which we ascribe to integration error brought about by the discrete nature of our measurements, both temporal and spatial. In reality, these forces will return to zero at pulse-end, and thus we use the discrepancy at the 200 $\mu$s point to determine the error owing to this effect.

Finally, we relate these Lorentz force thrust calculations to direct measurement. We calculated the total axial impulse per shot by time-integrating the force. This yielded 16.1±0.22 $\mu$N-s, approximately 42% of which is due to the structure force. Notably, this result underpredicts the 64.3 $\mu$N-s measured reported at the same operating conditions from thrust stand measurements. A key implication of this result is that the Lorentz force measured may not fully explain the thrust generation, indicating other acceleration mechanisms may be at play. Indeed, our recent modelling study suggests that a significant portion of thrust may be due

to electron pressure at the thruster walls [89].

While electron pressure at the thrust walls approximately explains the difference between calculated Lorentz force thrust and measured thrust, we expect that the estimates of Lorentz force thrust are likely underpredictions. Because our device–in particular the shape of the bias magnetic field–is qualitatively similar to a magnetic nozzle thruster, the bias field might produce additional thrust owing to the high electron densities ($n_e \geq 1 \times 10^{19}$) and temperatures ($T_e \geq 8$ eV) measured. However, as the diamagnetic drift and associated Lorentz force which cause magnetic nozzle thrust typically take place further downstream than what is interrogated by our probing techniques in this work [90], we do not expect to resolve these effects.

In summary, in this section we have experimentally characterized in detail the induced currents and magnetic fields in the RMF test article. We have have found that the device does in fact lead to FRC formation. Moreover, we have also shown that forces experienced by the plasma are primarily radial, and that the axial forces which do exist are driven by the bias field and the structure field in roughly equal proportion. However, this total force does not fully explain that which we measured via thrust stand, suggesting that non-Lorentz forces may also be key drivers for performance.

## 6.4 Extrapolation to CW-Mode

Because the frequency of excitation collisions, which represent the dominant thermal loss mechanism, scales quadratically with electron density [74], it stands that performance might be improved by operating at lowered density compared to pulsed-mode operation, where the neutral density in the thruster immediately pre-pulse is driven by thermal diffusion of the neutral Xe atoms out the exit of the cone. However, if the thruster were instead operated in a continuous wave (CW) -mode at the same mass flow rate of propellant, conservation of mass dictates that the higher velocity would cause lowered density in the cone relative to the pulsed mode. In this operating mode, we would expect the RMF thruster to behave more like an electrodeless applied-field MPD thruster. In this way, a CW-mode RMF thruster would retain its strengths as a high specific-power, ISRU-compatible device while shrugging off its main loss mechanism. In light of this potential tradeoff, the need is apparent for an investigation into the effectiveness of CW-mode operation for an RMF thruster. The goal of this section is to provide performance predictions for CW-mode operation using scaling arguments and pulsed-mode measurements.

### 6.4.1 Analysis Methodology

In this section, we outline scaling arguments for relating transient measurements from pulsed operation to predictions for plasma properties behavior during CW-mode operation. We then translate these relationships to estimates for performance.

#### 6.4.1.1 Mass Conservation

Figures 6.6a and 6.6b show the total current induced in the thruster as a function of time for the 45 sccm Xe, 2 kA pk-pk RMF current amplitude, 180 G peak centerline bias condition for 125 $\mu$s and 200 $\mu$s cases. These figures illustrate a key trend in all data taken. There first is a low signal followed by an ionization event when the entire volume of the thruster is ionized. High levels of current are then driven before electron density and current density fall off as plasma is ejected from the thruster.

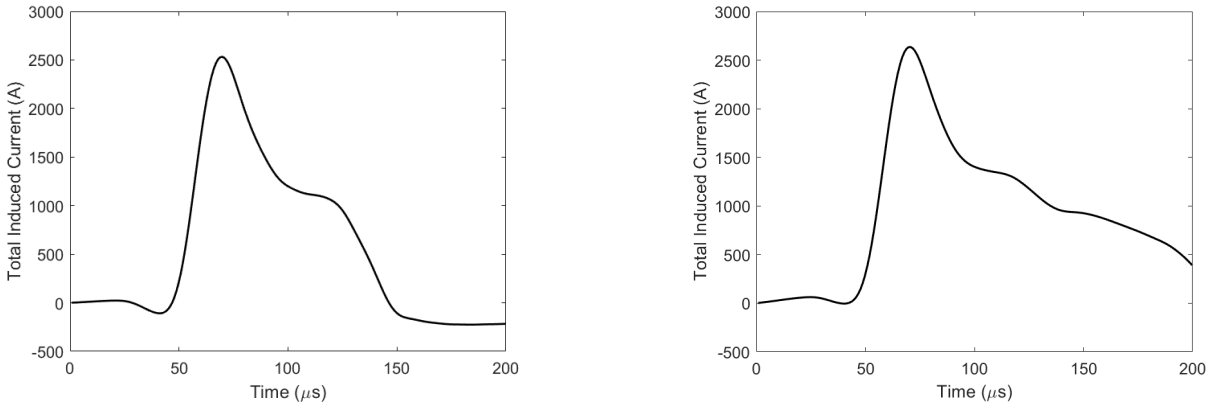


(a) (b)

Figure 6.6: Total current driven at the 45 sccm Xe, 2 kA pk-pk RMF current amplitude, 180 G peak bias field condition. a) 125 $\mu$s pulse duration. b) 200 $\mu$s pulse duration.

The high peak currents during the initial ionization event can be ascribed to the initial condition in the thruster immediately before the pulse. Because propellant flow rate is steady and the time between pulses long compared to the fill time, the pre-pulse neutral density in the thruster is dictated by the thermal speed of the neutrals according to mass continuity:

$$\dot{m} = M n_n(z) A_c(z) u_{th}, \tag{6.1}$$

where $M$ is the mass of a propellant atom, $u_{th} = \sqrt{\frac{8k_B T_n}{\pi M}}$, $A_c$ is the local cross section of the cone, and $n_n$ is the neutral density. Because of the plasma density scaling for induced

current density described in Eq. 2.12, this leads to the very high initial current peak.

As plasma is ejected from the cone and density drops from initial levels closer to steady-state levels, plasma current drops. However, although Figure 6.6b helps to show this trend, the pulse is not long enough to have measured the steady value of current as the value is still dropping at the end of the 200 $\mu$s pulse. To attempt to quantify the CW-mode density values, we make two major assumptions.

First, we assume that the electron distribution at the time corresponding to the peak of the driven current plot in Figure 6.6a is equal to the neutral density distribution pre-pulse. This is equivalent to stating that every neutral atom is singly ionized and the distribution does not change immediately as a result of that ionization process. In analytic form, this can be written

$$n_n(t < 0) = n_e(t = t_p). \tag{6.2}$$

where $t_p$ refers to the time at which the current peaks during the pulse, and the pulse begins at $t = 0$. Next, we make the further assumption that although the total number of electrons may change between the peak of the initial pulse and the CW-mode value, the shape of the distribution does not. Put mathematically, this says

$$\frac{n_e(t = t_p)}{\iiint_V n_e(t = t_p)dV} = \frac{n_e(t/ggt_p)}{\iiint_V n_e(t/ggt_p)dV} \tag{6.3}$$

Next we note that because we have assumed full single ionization, and taking into account quasi-neutrality which states that $n_e = n_i$ at any given time and location, where $n_i$ is the ion density, we define

$$n_p = n_e(t = t_p) = n_i(t = t_p) \tag{6.4}$$

$$n_{cw} = n_e(t \gg t_p) = n_i(t \gg t_p) \tag{6.5}$$

We can finally call upon conservation of mass, which states

$$\dot{m} = Mn_p(z)A_c(z)u_{th} = Mn_{cw}(z)A_c(z)u_{cw}(z) \tag{6.6}$$

$$u_{cw} = \frac{n_p(z)}{n_{cw}(z)}u_{th} \tag{6.7}$$

$$u_{cw} = R_n u_{th} \tag{6.8}$$

where $u_{cw}$ is the exit velocity of the ions in CW-mode operation and where we have defined $R_n = \frac{n_p(z)}{n_{cw}(z)}$ to be the density ratio between the peak of the pulse and CW-mode operation.

Eqn. 6.8 states two things. First, the lower the density due to CW-mode operation relative to that dicated by thermal diffusion, the higher the CW-mode exhaust velocity will be. Second, because $n_p$ and $n_{cw}$ are assumed to have the same profile, their quotient is a scalar constant, and thus $u_{cw}$ is assumed not to be a function of position in the cone.

#### 6.4.1.2 Momentum Conservation

While $u_{th}$ is a quantity easily calculated and $n_p$ is measured, Eqn. 6.8 is not closed. To remedy this, we add momentum conservation, which states that

$$\iint Mn\vec{u}(\vec{u}\cdot d\vec{A}) = F \tag{6.9}$$

where $F$ is the sum of all external forces on the fluid. In this case, we take the forces to include the Lorentz force owing to the bias field and thermal force owing to electron pressure on the thruster walls. We further assume that all velocity is directed axially. Eqn. 6.9 then simplifies to

$$Mn_{cw,exit}A_{exit}u_{cw}^2 - Mn_{th,in}A_{in}u_{th}^2 = F_{L,cw} + F_{th,cw} \tag{6.10}$$

$$\dot{m}\left(u_{cw} - u_{th}\right) = \iiint_V B_{0,r}j_{cw}d^3r + 2\pi\sin\left(\theta_c\right)\int n_e k_B T_e r d\vec{l} \tag{6.11}$$

$$\tag{6.12}$$

where we have recognized $\dot{m} = MnAu$ for both CW and pulsed values, and substituted the expressions for Lorentz and thermal force from Eqns. 2.34 and 2.32. To determine the induced current density $j_{cw}$, we consider that the ideal current density is given by $j = en_e\omega r$. Taking inspiration from standard analysis techniques for induction motors, which function on the same principles as the RMF current drive, we define a slip $s(\vec{r},t)$ to account for difference in rotational speeds between the electrons and the RMF caused by lack of full penetration. In this way,

$$s(\vec{r},t) = \frac{\omega - \omega_e(\vec{r},t)}{\omega} \tag{6.13}$$

where $\omega$ without a subscript again refers to the RMF frequency, and $\omega_e$ is the rotational frequency of the electrons residing at location $\vec{r}$ and time $t$. The next major assumption in this analysis is that we preserve the same slip between the peak pulse value and the CW-mode value. This would necessarily require the same degree of penetration. In other

words,

$$\frac{I_{RMF,p}}{I_{RMF,p,min}} = \frac{I_{RMF,cw}}{I_{RMF,cw,min}} \tag{6.14}$$

$$\Rightarrow I_{RMF,cw} \approx \frac{n_{cw}}{n_p}\left(\frac{T_{cw}}{T_p}\right)^{-\frac{3}{4}} I_{RMF,p} \tag{6.15}$$

where $I_{RMF,min}$ is calculated by considering Eqn. 2.27 as an equality, and the $\approx$ sign is used due to the influence of the Coulomb logarithm in Eqn. 2.27. However, as the Coulomb logarithm is highly insensitive to changes in density and temperature, the rough equality holds.

Given the introduction of the slip term, we therefore modify our expression for ideal RMF current to become

$$j = en_e s\omega r. \tag{6.16}$$

Given our assumption that CW-mode slip and pulse peak slip are equal, and leveraging Eq. 6.16, we find

$$\frac{j_{cw}}{j_p} = \frac{n_{cw}}{N_p} \tag{6.17}$$

$$\Rightarrow j_{cw} = R_n j_p. \tag{6.18}$$

Substituting Eqn. 6.18 into 6.11 and defining $R_T = \frac{T_{cw}}{T_p}$, we find

$$\dot{m}\left(u_{cw} - u_{th}\right) = R_n \iiint_V B_{0,r} j_p d^3r + R_n R_T \iint_A n_p k_B T_{e,p} \sin\theta_c dA. \tag{6.19}$$

This equation states that forces owing to Lorentz interaction and electron thermal pressure will directly lead to an increase in exit velocity for CW-mode operation relative to the input diffusion velocity. Further, it states that this effect will be reduced linearly with CW-mode density for both effects, and reduced with CW-mode temperature for the pressure force. However, we have introduced a new unknown variable $R_T$, which will require a third equation to close the system.

#### 6.4.1.3 Energy Conservation

The thermal force in Eqn. 6.19 introduces electron temperature, requiring the addition of an energy equation to close the system. In the CW-mode, the system must necessarily be at steady state, therefore $\frac{dE_{cw}}{dt} = 0$. Further, we assume that the sole heat generation

mechanism is ohmic heating due to classical collisions and that thermal energy is lost due to radiation from excitation collisions, electron wall losses, and the power associated with the thermal force defined in Eqn. 2.32. Therefore,

$$P_{ohm,cw} + P_{ind,cw} - P_{rad,cw} - P_{wall,cw} - P_{Fth,cw} - P_{FL,cw} = 0 \tag{6.20}$$

$$P_{ohm,cw} = P_{rad,cw} + P_{wall,cw} + P_{Fth,cw} \tag{6.21}$$

where $P_{ohm,cw}$ is thermal power gnerated through ohmic heating, $P_{ind,cw}$ is the inductive power introduced to the system by the RMF, $P_{rad,cw}$ is the radiated power lost via excitation collisions, $P_{wall,cw}$ is the power lost to electron-wall interactions, $P_{Fth,cw}$ is the power associated with accelerating propellant via electron pressure force, and $P_{FL,cw}$ is the power associated with accelerating propellant via the Lorentz force. We make the assumption that all inductive power introduced is used to accelerating propellant via the Lorentz force, so that $P_{ind,cw} = P_{FL,cw}$. We then seek functional forms for each of the remaining terms. Ohmic power will be given by the expression

$$P_{ohm} = \iiint_V \eta_{ei} j^2 dV \tag{6.22}$$

where plasma resistivity is $\eta_{ei} = \frac{m_e \nu_{ei}}{e^2 n_e}$ with $\nu_{ei}$ being given in Eq. 2.5. Substituting plasma resistivity into Eqn. 6.22, we find

$$P_{ohm} = \iiint_V \left(2.9 \times 10^{-12}\right) \frac{m_e}{e^2} \ln \Lambda T_{eV}^{-\frac{3}{2}} j^2 dV \tag{6.23}$$

$$\Rightarrow P_{ohm,cw} = R_n^2 R_T^{-\frac{3}{2}} \iiint_V \left(2.9 \times 10^{-12}\right) \frac{m_e}{e^2} \ln \Lambda_{cw} T_{eV,p}^{-\frac{3}{2}} j^2 dV \tag{6.24}$$

where electron-ion collision frequency is taken from Goebel and Katz [74], $\ln \Lambda$ is the Coulomb logarithm, given as $\ln \Lambda = 23 - \frac{1}{2} \ln \left(10^{-6} n_e T_{eV}^{-\frac{3}{2}}\right)$, and $T_{eV}$ refers to electron temperature in units of electron Volts. Radiated power is calculated using the expression

$$P_{rad} = \iiint_V n^2 \sigma^* v_e \epsilon^* dV \tag{6.25}$$

$$P_{rad,cw} = R_n^2 R_T^{\frac{1}{2}} \iiint_V n_p^2 \sigma^* \sqrt{\frac{8 k_B T_p}{\pi m_e}} \epsilon^* dV \tag{6.26}$$

where $< \sigma^* >$ is the electron-ion excitation collision cross section, taken from a numerical fit in Ref. [91], $v_e$ is mean electron velocity, and $\epsilon^*$ is the energy released per excitation collision, taken from Hayashi et al. to be 8.32 eV [92, 93].

Electron power loss to the walls of the device are taken from Goebel and Katz [74] and

simplified to

$$P_{wall} = \iint_A \sqrt{\frac{e^3}{2\pi m_e}} \left(2 + \sqrt{\frac{2M_i}{\pi m_e}}\right) \exp\left(-\sqrt{\frac{2M_i}{\pi m_e}}\right) n T_{eV}^{\frac{3}{2}} dA \tag{6.27}$$

$$P_{wall,cw} = R_n R_T^{\frac{3}{2}} \iint_A \sqrt{\frac{e^3}{2\pi m_e}} \left(2 + \sqrt{\frac{2M_i}{\pi m_e}}\right) \exp\left(-\sqrt{\frac{2M_i}{\pi m_e}}\right) n_p T_{eV,p}^{\frac{3}{2}} dA \tag{6.28}$$

Finally, power due to thermal acceleration by means of pressure at the thruster wall is given by

$$P_{Fth} = u F_{th} \tag{6.29}$$

$$P_{Fth} = u_{cw} R_n R_T \iint_A n_p k_B T_p \sin\theta_c dA \tag{6.30}$$

$$P_{Fth} = u_{th} R_n^2 R_T \iint_A n_p k_B T_p \sin\theta_c dA \tag{6.31}$$

Substituting Eqns. 6.24, 6.26, 6.28, and 6.31 into 6.21 and making the proper substitutions, we find

$$R_T^{-\frac{3}{2}} \iiint_V \left(2.9 \times 10^{-12}\right) \frac{m_e}{e^2} \ln\Lambda_{cw} T_{p,eV}^{-\frac{3}{2}} dV = R_n^2 R_T^{\frac{1}{2}} \iiint_V n_p^2 \sigma^* \sqrt{\frac{8eT_{eV,p}}{\pi m_e}} \epsilon^* dV + ...$$
$$... + R_n R_T^{\frac{3}{2}} \iint_A \sqrt{\frac{e^3}{2\pi m_e}} \left(2 + \sqrt{\frac{2M_i}{\pi m_e}}\right) \exp\left(-\sqrt{\frac{2M_i}{\pi m_e}}\right) n_p T_{eV,p}^{\frac{3}{2}} dA + u_{th} R_n^2 R_T \iint_A n_p k_B T_p \sin\theta_c dA \tag{6.32}$$

where $\ln\Lambda_{cw}$ refers to the Coulomb logarithm evaluated with $T_{cw} = R_T T_p$ and $n_{cw} = R_n n_p$. Finally, $u_{cw}$, $R_n$, and $R_T$ can be calculated by solving the system of equations comprised of Eqns. 6.8, 6.19, and 6.32.

### 6.4.2 Performance Estimation

Once $u_{cw}$, $R_n$, and $R_T$ are known, force can be calculated using Eq. 6.19, and useful jet power with

$$P_{j,cw} = \frac{F_{cw}^2}{2\dot{m}}. \tag{6.33}$$

Using the framework set forth in Gill et al., 2022 [87], we can approximate the efficiency of the RMF thruster as

$$\eta_T = \eta_c \eta_d \eta_m \eta_p \tag{6.34}$$

where $\eta_c$ refers to the coupling efficiency, the fraction of energy coupled from the RMF antennas into the plasma, and $\eta_a$ and $\eta_p$ are the acceleration and plasma efficiencies whose product describes the ratio of coupled energy to useful directed kinetic energy. In this way, we can write

$$\eta_d \eta_m \eta_p = \frac{P_{j,cw}}{P_{j,cw} + P_{rad,cw} + P_{wall,cw}}, \tag{6.35}$$

all quantities other than $P_{j,cw}$ are calculated in Eqn. 6.32. Meanwhile, the coupling efficiency will be given by

$$\eta_c = \frac{P_{j,cw} + P_{rad,cw} + P_{wall,cw}}{P_{in}} \tag{6.36}$$

$$\eta_c = \frac{P_{j,cw} + P_{rad,cw} + P_{wall,cw}}{P_{LL} + P_{j,cw} + P_{rad,cw} + P_{wall,cw}} \tag{6.37}$$

where $P_{in}$ is the total power injected and is equal to the sum of power coupled into the plasma and $P_{LL}$, power lost in the RMF transmission lines. To estimate $P_{LL}$, we consider that we have already made the assumption that we have the same degree of penetration in the CW-mode as the pulsed mode which gives an estimate for the required RMF current via Eqn. 6.15. We calculate an effective RMF line resistance by comparing energy expended in a so-called 'vacuum shot' in which the RMF is pulsed at representative amplitude with no plasma present. The energy input from the main power supply can then be compared to the energy expended in the switching circuitry and RMF lines according to

$$\Omega_{eff} = \frac{I_s V_s}{f_{rep}\left(\int I_{RMF,x}^2 dt + \int I_{RMF,y}^2 dt\right)} \tag{6.38}$$

where we have used $\Omega_{eff}$ for the effective line resistance to avoid confusion with $R_n$ and $R_T$, $I_s$ and $V_s$ are the voltage and current output of the feed supply, $f_{rep}$ is the pulse repetition rate, and $I_{RMF,x}$ and $I_{RMF,y}$ are the current through the x and y RMF antennas, respectively.

Once $\Omega_{eff,cw}$ is known, we can calculate line loss by considering that the RMF current

forms a sine wave. Because the average of $\sin^2(x)$ is $\frac{1}{2}$, then

$$P_{LL} = 2\left(\frac{1}{2}\Omega_{eff,cw} I^2_{RMF,cw}\right) \tag{6.39}$$

where the factor of 2 comes from having two separate and equal current paths comprising the x and y antennas. We note that in the event $E_s$ is indeed linear with $I_{RMF}$, $P_{LL}$ can then be substituted into Eqn. 6.37 to close the last unknown term in the performance analysis.

### 6.4.3 Pulse-End Measurements

In addition to the above analysis to predict CW-mode performance, we can employ measurements from the end of the pulse of the 200 $\mu$s pulse duration condition to prove sanity checks.

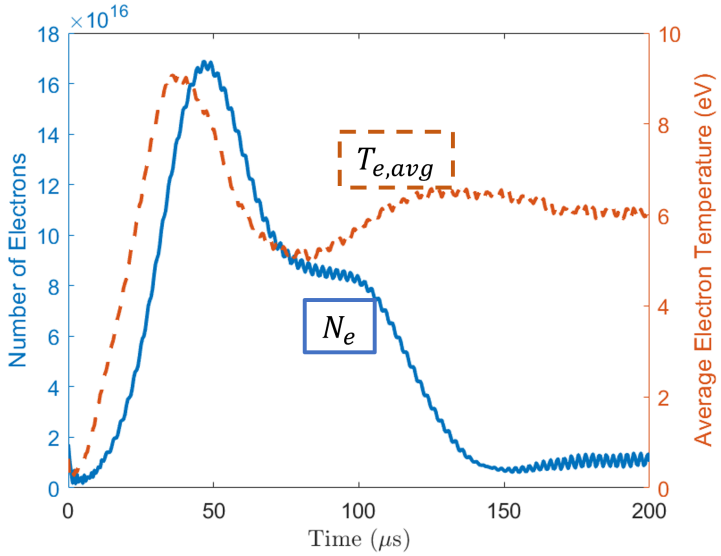


Figure 6.7: Total integrated electron number $N_e$ and averaged electron temperature $T_{e,avg}$ for the 45 sccm, 2000 A pk-pk RMF current, 180 G centerline, 200 $\mu$s pulse duration condition

Figure 6.7 shows the total integrated electron number and average electron temperature over time using electron density measured with the triple Langmuir probe for a 200 $\mu$s pulse duration case. It can be seen that both plots reach a high peak, similar to the total current shown in Figure 6.6b which corresponds to the same operating condition. Unlike the current, however, these quantities appear to find steady values at the end of the pulse while the current is still dropping at that time step. Recognizing that because the current is still dropping, this does not truly correspond to CW-mode operation, we can use the data at the

| Flow (sccm Xe) | Peak Bias Field (G) | $T_{cw}$ (mN) | $I_{sp,cw}$ (s) | $P_{in}$ (kW) | $\eta_m\eta_d\eta_p$ | $\eta_c$ | $\eta_T$ |
|---|---|---|---|---|---|---|---|
| 60 | 180 | 21.3 | 390 | 2.75 | .042 | .356 | .015 |
| 45 | 120 | 19.6 | 474 | 2.46 | .051 | .351 | .018 |
| 45 | 180 | 19.0 | 460 | 2.70 | .060 | .255 | .015 |
| 45** | 180** | 35.7 | 824 | 2.35 | .082 | .751 | .061 |

Table 6.1: Summary of results of CW-mode prediction analysis. All estimates are based on data taken from thruster operation using 2 kA pk-pk RMF current rotating at 415 kHz. The final case (set off with asterisks) is a direct measurement taken at the end of a 200 $\mu$s pulse.

200 $\mu$s point as a proxy for the true measurement as a means of rough validation for this analysis.

Taking the data for $n_e$, $T_e$, and $j$ for $t = 200$ $\mu$s, we calculate the Lorentz and thermal forces using Eq. 2.34 (neglecting $B_{struct}$ and the diamagnetic current). Loss mechanisms are calculated in the same manner as for the CW analysis but using the directly-measured values rather than predicted CW-mode values for $n_e$, $T_e$, $F_L$, $u$, and $F_{th}$.

### 6.4.4 Results

In this section we present the results of the analysis detailed in above. For each operating point, the anticipated thrust, $I_{sp}$, total input power, and efficiency are displayed in Table 6.1.

For each operating condition, CW-mode efficiency is seen to more than triple over direct measurement made in pulsed mode at the same operating conditions, where the highest measured overall efficiency is ~0.5% corresponding to the 45 sccm, 2 kA $I_{RMF}$, 180 G centerline, 125 $\mu$s pulse condition whose CW-mode equivalent is the second entry in Table 6.1. However, despite this relative uplift, overall efficiency remains low (<2%) with the $\eta_a\eta_p$ term dominating in all three conditions.

Examining the 200 $\mu$s pulse-end measurement shown as the last entry in Table 6.1, thrust and specific impulse are both roughly double the corresponding values for the CW-mode prediction of the same operating condition while using ~13% less power. Additionally, while $\eta_d\eta_m\eta_p$ is only ~30% higher than the CW-mode prediction, $\eta_c$ is increased by a factor of 3. This result is likely erroneous, as the predicted $I_{RMF}$ for this condition is only ~7 A, a number which appears unrealistically low.

To examine how the efficiency trades between pulsed-mode operation, CW-mode operation, and the pulse-end measurements which appear to lie somewhere in the transition region, we plot the relative radiation and wall losses for each case in Figure 6.8a. The trend exhibited agrees with the initial goal of CW-mode operation: to lower radiation losses by reducing plasma density. The calculations which refer to the peak of the pulse show radiation

vastly dominating over wall losses, while the CW-mode prediction shows radiation losses to now be insignificant when compared to wall losses. The 200 $\mu$s pulse-end condition appears to correspond to a case in which the density has yet to fully reach the CW-mode state as the portion of losses relating to radiation lies between the pulse peak and CW-mode conditions.

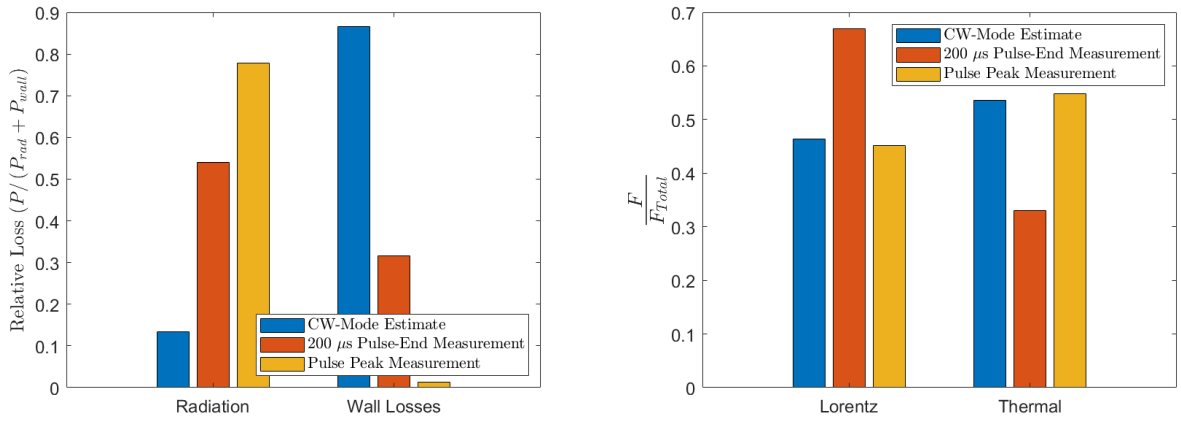


(a) (b)

Figure 6.8: Comparison of predicted a) loss mechanisms and b) force mechanisms for the 45 sccm, 180 G bias field condition. Pulsed-mode operation for which the data was taken used 2000 A pk-pk RMF current.

With this being said, the issue of low efficiency is clearly not solved by the switch to CW-mode operation, as the wall losses have become significant where they were not during pulsed operation. To consider why this might be the case, we can refer to the relative scaling for jet power, radiated power, and wall losses. We observe that jet power will scale quadratically with electron density, as will radiation losses. Wall losses, meanwhile, only scale linearly. Therefore the radiation losses are reduced commensurately with jet power, while wall losses are mitigated to a significantly lesser degree.

To contextualize the power loss terms with respect to the forces, we look to Figure 6.8b, where we can see that thermal forces are commensurate with Lorentz forces, and are larger for both the pulse peak and CW-mode prediction. The thruster in its present state is therefore behaving as a mostly thermal device, despite all design work geared toward the Lorentz force being the chief driver of momentum transfer to the propellant. In light of the fact that this thermal thrust is due to electron thermal pressure on the physical walls of the device, it is not surprising that electron wall losses are dominant.

## 6.5 Discussion

### 6.5.1 Efficacy of RMF Current Drive

As discussed in Chapter 1, a major benefit from the RMF thruster is its ability to divorce the magnitude of current driven in the plasma from the amplitude of the current in the driving circuit. This contrasts with a more traditional theta-pinch inductive current drive, where large driver current (and therefore voltage) transients are required to drive the internal currents. This poses major challenges to design and robust construction. Our data shows that the RMF current drive as implemented here is successful at producing high plasma currents—driving currents of 2500 A while only requiring RMF current of ∼700 A RMS (2000 A peak-to-peak). Further, current densities measured are on similar order to those predicted in Fig. 2.2b, which is an encouraging indication that current drive is functioning properly. Leaving aside the poor thrust efficiency measured in this device, it is an encouraging result that the current drive mechanism, which forms the basis of this technology, is effective.

As a direct result of these high levels of driven current, we observed the formation of an FRC plasmoid (Fig. 6.2). This was not unexpected given the RMF current drive mechanism was first implemented to drive field reversal for fusion containment applications [50]. From the perspective of thruster performance, the existence of this self-contained structure in principle offers key benefits including increased plasma density [39], reduction in wall losses, and benefits for thrust generation [57]. With this being said, we see the outer separatrix intersects the outer wall of the thruster cone in our thruster configuration, which may ultimately have negated key benefits arising from the FRC's containment. This may have been a chief contributing factor to the high degree of wall losses previously reported for this device [88]. In practice, adjusting the applied field or reducing the driven current may help to pull the separatrix inside the thruster walls, reducing these wall losses.

### 6.5.2 Contributions of Lorentz Force to RMF Plasmoid Acceleration

One of the key goals of the inductive probing study presented in this chapter was to assess the degree to which the Lorentz force contributed to thrust in the RMF device. In practice, when comparing the Lorentz force impulse to performance measurements at the same operating conditions, we found that the Lorentz force only accounts for ∼25% of the total impulse generated per shot [76]. This is notable because it undermines a conventional understanding of this device as an electromagnetic accelerator.

This invites the question as to what drives most of the acceleration in the thruster. As

briefly discussed in Sec. 6.4.4, thermal contributions arising from compression of the plasma explain the difference. Inspecting the relative magnitudes of the axial versus radial forces in Fig. 6.5c, it is clear that the majority of the Lorentz forces point inwards in this device, with the inward radial force over five times greater in magnitude than the axial. Given the relative lack of plasmoid radial acceleration over the course of the pulse, as evidenced by Fig. 6.2, we can conclude that there is approximate radial pressure balance in the plasmoid. It is possible then that a high electron thermal pressure, driven primarily by high electron densities in the $10^{19}$ $1/\mathrm{m}^3$ range, is in turn driven by this strong radial compression. This pressure would result in a force equal to $\int_A (nT_{eV} \sin\theta_c)\, dA$ where $A$ refers to the internal area of the thruster and $\theta_c$ is the thruster cone half-angle. Indeed, calculations using electron temperature and density measured with a triple Langmuir probe from Ref. [88] suggest that this electron pressure force approximately explains the discrepancy between measured impulse and calculated Lorentz force [89]. We remark here that previous interpretations have also suggested that thermal contributions could be major drivers for thruster operation [57].

In practice, however, we suspect the ideal thrust mechanism for the RMF thruster is the Lorentz force. The thermal force is correlated with high electron temperatures and densities. The high densities carry with them enhanced radiation losses, while both density and temperature increase electron wall losses. Therefore the force associated with electron pressure at the walls of the thruster rather than due to the diamagnetic drift or direct RMF current drive is a necessarily inefficient thrust mechanism and should be avoided. In light of this interpretation, a different bias field that reduces radial force may lead to lower compression, trading thermal heating for improved Lorentz acceleration, which may be advantageous.

### 6.5.3 Strategies for Improving Performance

One of the major conclusions of our previous work [94] is that performance for the RMF thruster is not competitive compared to state of the art electric propulsion devices. Indeed, efficiencies are over an order of magnitude lower than other inductive devices such as RF magnetic nozzles [95]. Ohmic losses in the RMF antennas and power conditioning circuity, radiation losses, and thermal flux to the walls all have been identified as major loss processes [88]. Sec. 6.4.4 shows that the FRC separatrix intersects the thruster walls, providing a direct thermal short to the thruster boundaries. Moreover, as discussed in the previous section, we have found that thrust generation by Lorentz acceleration is not as dominant as theoretically anticipated.

Given this poor performance, a key question is whether there are paths to improving

the performance of RMF thruster. The motivation for this when drawing a contrast to steady-state inductive devices (which already have exhibited higher levels of efficiency than our device) is the potential for improved flexibility in throttling and power density. Leaving aside adjustments to the power conditioning—which may afford marked improvements in performance—our findings about the internal dynamics of the device suggest two possible strategies for improving thruster operation. The first is to amplify the Lorentz acceleration. For the applied field force, we could improve this contribution by adjusting the shape to increase the radial components of the applied field while also increasing magnetic field strength. With that said, while we may be able to optimize geometry by adjusting solenoid position, increasing magnetic field requires more power and stronger magnetics which can become prohibitive in mass and power.

As a second strategy, we could attempt to enhance the structure field by introducing additional flux conserving elements and optimizing their placement and inductances. This has the additional benefit that the self-field interaction scales quadratically with the RMF driven current, providing nonlinear gains in thrust generation for only moderate adjustments in design and geometry. This would also have the benefit of moving the separatrix radius inward, potentially solving the problem of the separatrix intersecting the thruster walls. FRC compression using flux conservers is a standard practice in the fusion community, and indeed flux conserver conductivity is a key figure of merit in that field [42]. With this being said, we anticipate structure field amplification to be a suboptimal method of increasing performance. Idealized circuit analysis suggests that it could be difficult to fully utilize the inductive energy coupled into the flux conservers as part of this process [86].

With all this being said, however, the most compelling strategy at this point in time toward increasing performance for the RMF thruster is to employ CW-mode operation. The analysis presented in this chapter suggests that we might see between a three to six times improvement in efficiency. While such a jump would still not make the RMF thruster competitive with state-of-the-art immediately, it permits additional optimization after CW-mode thruster behavior is better understood. A like operating condition may allow us to make direct comparison between operating modes, but in the event that CW-mode scales differently from pulsed-mode, the true optimum may be in a very different regime than is explored in this analysis.

### 6.5.4 Scaling consequences of CW-Mode Extrapolation

The point to the conclusion that CW-mode operation of the RMFv2 thruster, while anticipated to be significantly more performant than pulsed operation, is still not an effective

method of thrust generation due to high power losses. While in pulsed operation, radiation losses dominate with electron wall losses accounting for a small fraction of power lost, the situation is expected to reverse for CW-mode operation. Additionally, the CW-mode RMF thruster in its present configuration is predicted to behave fundamentally as a thermal thrust device, but without the design optimization for such behavior.

According to the equations set forth the established current drive model in Chapter 2, increasing the power level of the device ought to be possible by increasing the mass flow rate and maintaining similar penetration. Jet power will increase quadratically with density, as both Lorentz force and electron pressure increase linearly with density. Radiation losses, while insignificant at the densities associated with CW-operation at the mass flow rates considered in this study, also increase quadratically with density. Wall losses, the dominant loss mechanism for the cases considered, increase only linearly as density increases. Therefore, we may expect an optimum mass flow rate for CW-mode operation of the RMF thruster in which radiation and wall losses are balanced. The $\sim$4 times higher performance calculated for the 200 $\mu$s pulse-end condition, in which the two plasma losses are much closer to each other in magnitude, provides some evidence for this claim.

### 6.5.5 CW-Mode Loss Mitigation Strategies

Due to the scaling relations set forth, few parameters exist which appear to significantly change performance. As a result, fundamental changes should be made to the device if we wish to improve the efficiency by means of loss mechanism reduction. While the coupling efficiency $\eta_c$ was is significantly greater than the plasma and acceleration efficiency $\eta_d\eta_m\eta_p$, it still accounts for a large amount of power lost. Indeed, the line losses $P_{LL}$ represent the single largest loss mechanism in terms of raw magnitude. Therefore a re-examination of the switching circuitry used in the RMFv2 thruster is warranted before attempting CW-mode operation. Larger conductors and more efficient switches could serve to significantly reduce this loss mechanism. The line losses could also be reduced by further reduction in RMF current. In this analysis we make the assumption that the penetration condition remains the same between the pulsed and CW-mode operation. However, we do not presently have a clear understanding on when penetration is truly lost owing to the 'much greater than' condition present in Eq. 2.27. Therefore, it may be possible to reduce the RMF current without causing significant reduction in jet power, enabling a reduction in $P_{LL}$ quadratic with the reduction in input current.

To reduce the losses which happen in the plasma itself, a re-examination of the bias magnetic field is warranted. In particular any change in magnetic field which might reduce

electron-wall interaction could reduce the electron wall loss term. A study into the shape of the bias magnetic field could prove valuable in this respect. While such a change would also reduce the thermal component of force as calculated in this analysis, we posit that a more effective magnetic field would translate the electron energy into current via the diamagnetic drift, which would then appear in the Lorentz force term as additional current.

### 6.5.6 CW-Mode Extrapolation Analysis Shortcomings

This analysis requires several large assumptions which must be kept in mind when discussing its conclusions. First among these is the stipulation that neutral density, electron density, current density, and electron temperature profiles are conserved between the pulsed and CW-mode operation. Because of the nature of the two conditions, this assumption is likely inaccurate. The density profile in the pulsed case is measured shortly after the ionization of neutrals whose distribution will be determined by thermal diffusion at a constant thermal velocity. In contrast, the velocity of ions in CW-mode can realistically be expected to vary throughout the cone as it is accelerated, likely through some finite acceleration region. This would lead to very different shape of the density profile. Evidence for this being the case can be found by comparing the shape of the total integrated electron number found in Figure 6.7 to the total current for the 200 $\mu$s pulse. While the shapes of the two curves match remarkably well until the $\sim$150 $\mu$s point, they deviate significantly after, invalidating the assumption that the current density and electron density share the same profile at all times. Additionally, because several terms depend on the density profile (in particular the wall losses and thermal force which depend on the density along the thruster wall and the current density, which in the ideal case is proportional to $nr$) the shape of this profile could have a large impact on the results. However, intuiting whether this effect would cause this analysis to over- or under-predict performance is not straightforward.

The next critical assumption is that the effective line resistance $R_{eff}$ is constant between the vacuum shots and the lower CW-mode RMF currents. Because switching losses due to the IGBT switches employed in our power processing unit are not linear with current, the $R_{eff}$ used in this analysis may be higher than the true value, which would serve to reduce the line losses. Proper characterization would require measurement in a representative test setup.

Finally, this analysis depends on quantities with non-negligible uncertainty – in particular the triple Langmuir probe analysis process, which is described in greater detail in Gill et al., 2022 [88]. As a result, while this analysis is useful for examining trends, data should not be expected to reproduce thruster behavior exactly.

## 6.6 Conclusions

In this chapter we have presented plasma probing results to investigate the shortcomings of the RMFv2 thruster. We begin by showing the results of triple Langmuir probing which measure plasma density and temperature toward estimating the two highest loss mechanisms present in the RMFv2 thruster: electron wall losses and excitation radiation losses. This is followed with inductive probe measurements of the induced magnetic field and plasma currents. It is found that while we indeed see FRC formation in the thruster, indicating nominal current drive operation, the separatrix of that plasmoid intersects the thruster wall. This could contribute significantly to the high wall loses by providing enhanced electron mobility to the wall. By increasing the bias field, it is hypothesized that this separatrix/wall intersection may be avoided and thus the wall losses mitigated. Next, an analytic study is presented to attempt to extrapolate pulsed-mode performance to the CW-mode with the goal of reducing excitation radiation losses via the lower densities associated with that mode. A performance increase between three and six times is predicted. Taken together, this evidence points toward the conclusion that a new test unit is warranted which can enable both CW-mode operation and greater variability in bias field strength and shape.

# CHAPTER 7

# The PEPL RMFv3 Thruster: Design and Baseline Performance

## 7.1 Introduction

In this chapter we present the design and baseline performance meaurements for the RMFv3 thruster. We begin by discussing the primary motivations for constructing an entirely new test unit. We follow this with a description of the thruster design, including both the thruster mechanical setup and the power supply. Next we present the performance baseline measurements for this thruster, which is made up of a wide surrogate optimization campaign to identify general performance trends as well as a focussed study on bias field strength. We conclude with a discussion of the information gathered by the performance campaign and next steps to understand the reasons behind the results.

## 7.2 Design Motivation

To motivate the design and construction of an entirely new thruster, we begin by recalling our phenomenological performance model presented in Chapter 2:

$$\eta = \eta_d \eta_m \eta_c \eta_p \tag{7.1}$$

where $\eta_d$ refers to the divergence efficiency, $\eta_m$ is the mass utilization efficiency, $\eta_c$ is the coupling efficiency, and $\eta_p$ is the plasma efficiency. We recall that we found for the RMFv2 thruster that low plasma efficiency had the greatest impact on the overall low thruster efficiency. In particular, nearly all the energy coupled into the thruster was lost to heat via electron wall losses and excitation radiation losses. This behavior was found to be consistent with inductive probing on the same device, which showed that the Lorentz force accounted for only $\sim$25% of measured thrust, implying that the majority of the thrust was attributable

to electron pressure at the thruster wall. Further, the inductive probe measurements showed that the FRC separatrix intersected with the discharge chamber walls, which would naturally lead to enhanced electron/wall contact which may be in part responsible for the high wall losses in particular. The second greatest impact was due to coupling efficiency, with typical values of ∼30%. We expect that this is likely due to a combination of plasma density, pulse length, and RMF strength requiring optimization. Higher plasma densities effectively increase the mutual inductance between the plasma and antenna, resulting in better coupling. Meanwhile, based on the penetration conditions used to determine RMF amplitude, those increased densities would also require stronger RMF fields and therefore increased ohmic losses in power switching and transmission lines.

One strategy to reduce these losses is to employ CW-mode operation to reduce the plasma density in the thruster. A zero-D model was applied to the various loss mechanisms present in the RMFv2 thruster, invoking mass, momentum, and energy continuity to extrapolate pulsed-mode measurements to the CW-mode in Sec. 6.4. We found that for like operating conditions we can expect as much as a two to five times improvement to overall efficiency. While this still would not result in a thruster competitive with state-of-the-art, it indicates that CW-mode may be superior to pulsed-mode for this device and therefore worthy of study. Indeed, if performance is seen to increase substantially for a naive first attempt at CW-mode operation, it may be the case that future optimization may bring the thruster into the realm of competitition with state-of-the-art devices owing to the RMF thruster's unique advantages.

## 7.3 Thruster Design

In this section we present the design of the test article used in this study, the RMFv3 thruster. Our goal in constructing this device was to produce a highly modular device capable of exploring a wide variety of operating conditions in both pulsed-mode and CW-mode in an effort to address the dominant contributions to efficiency loss outlined in the previous section. Fig. 7.1 shows an annotated image of the resulting system. The main discharge chamber is composed of a flared pyrex cone which provides a bounding wall for plasma and neutral gas. This wall is surrounded by three RMF antenna pairs, spaced at 120 degree intervals. Two solenoids concentric to the RMF antenna provide the bias magnetic field in the system. These elements are all mounted to an aluminum backplate that is fastened to a G10 fiberglass base board. Behind the backplate, three capacitor banks—one for each antenna—are mounted and connected via low inductance lines to a driven three-phase power processing unit. During operation, xenon gas flows into the channel via two

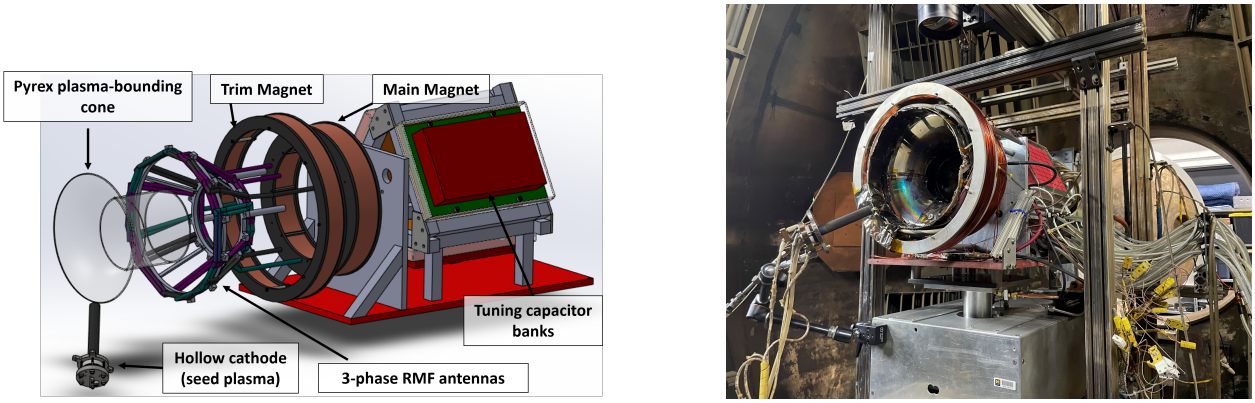


(a) (b)

Figure 7.1: RMF thruster build, shown a) as an exploded CAD rendering and b) as a photograph of the RMFv3 thruster mounted in the test facility.

neutral diffusers located at the inlet and exits of the pyrex cone. A hollow cathode located downstream of the thruster with its exit pointed toward the thruster exit plane provides the seed plasma for the device. With this general overview in mind, we describe in the following in detail each of the key elements of the thruster. We also remark on the motivation of our design decisions, relating these to the previous version of the thruster we built, the RMFv2.

### 7.3.1 Discharge Chamber

The pyrex cone which forms the discharge chamber has a 4.3 cm straight section which then flares from a radius of 6.5 cm to 12.5 cm over a length of 7.2 cm. This yields a total propellant-filled length of 11.5 cm. This chamber is relatively wide and short compared to the RMFv2. This decision was motivated by the previous experimental observation that high electron wall losses can account for over 30% of the efficiency loss of the system [88]. The short length and comparatively higher volume to area ratio in the updated design can help reduce these losses. The curved flare of the discharge chamber was selected to be approximately conformal with the bias magnetic field shape. This in principle further mitigates wall losses by requiring electrons to cross field lines to reach the wall. Pyrex was selected as the wall material because it could be shaped into a cone, it allows visual access to the plasma, and it is non-conductive, which avoids screening the RMF from reaching the plasma.

.

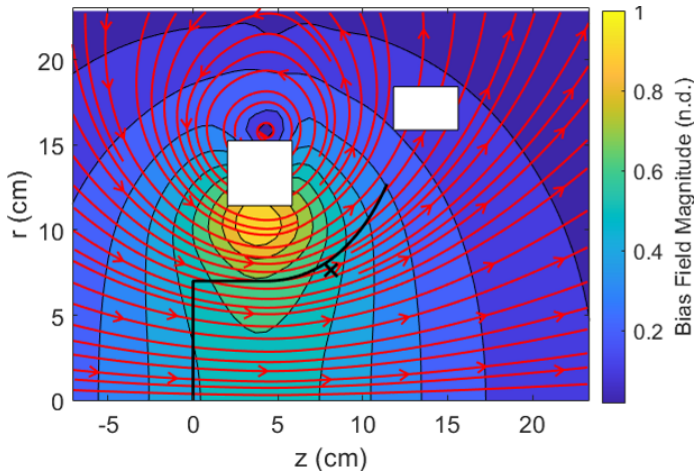


Figure 7.2: Bias magnetic field in the RMFv3 thruster. The solid black line depicts the location of the pyrex thruster wall, while the white squares represent the locations of the magnets themselves. The black 'X' indicates the position at which both the bias field and the RMF magnitudes are sampled for data analysis.

### 7.3.2 Bias Magnetic Field

The bias magnetic field is used in the RMF thruster to provide both plasma confinement from the walls through its axial component and Lorentz acceleration with the induced current through its radial component. A key weakness of the RMFv2 thruster was its relatively weak and highly axial bias field, a result of the thruster geometry. We therefore constructed the RMFv3 thruster with two solenoids to provide the bias field, referred to as the 'main' and 'trim' magnets. By adjusting the relative strength and polarity of the two magnets, the field strength and shape could be adjusted with the expectation that conforming the bias field to the profile of the discharge chamber wall would serve to reduce electron wall losses as shown in Fig. 7.2. In practice, the trim magnet was only weakly energized throughout the operating conditions considered in this study, resulting in the magnetic field structure depicted in Fig. 7.2.

We selected a single point marked approximately 7.5 cm upstream from the downstream face of the trim magnet and 7.5 cm radially out from center by the black 'X' in Fig. 7.2 to ascribe a strength to the bias magnetic field and the rotating magnetic field as discussed below. This allows us to describe relative strengths for these fields which are in reality dissimilar shapes. The comparison point was chosen arbitrarily in the region in which we anticipate current drive to occur based on experiment with the RMFv2 thruster.

### 7.3.3 RMF Antennas

In contrast to the RMFv2 two-phase system, we elected to use in this device a three-phase antenna architecture to produce the rotating magnetic field. This consists of three Helmholtz pairs of doubly-wound 4 AWG wire, each with an impedance of $L \approx 3.6$ $\mu$H. The axes of the antenna pairs are aligned transverse to the thruster central axis and spaced at 120 degree angles around the thruster circumference, each subtending 90 degrees. When energized, each pair produces a magnetic field transverse to the axis of the thruster. During operation, current is pulsed through each antenna with 120 degree offsets, leading to a rotating transverse magnetic field. Fig. 7.3 shows a map of the RMF streamlines at three points throughout an RMF period measured in the same plane as the bias field measurement location discussed previously. This demonstrates the capability of the system to provide a relatively uniform rotating field across the discharge chamber throughout a cycle.

We note here that this three-phase architecture is a departure from the two-phase approach employed in the RMFv2 thruster. The three phase approach has the benefit of more uniform transverse field during an RMF cycle and reduced antenna/cable heating (a previous problem for thrust stand measurements). Three-phase antenna design reduces thermal loading on the antenna because the return current from a given leg passes through the other two, causing their magnetic fields to constructively combine for a 33% increase to field strength. We further increase the RMF strength-to-current ratio in the RMFv3 thruster by double-wrapping the antennas. As a result the currents used in the RMFv3 to produce the same RMF field strength are approximately 41% of the previous version of the thruster, effectively eliminating cable heating as a source of measurement error.

### 7.3.4 RMF Current Generation

Fig. 7.4 shows a simplified circuit diagram of the RMF power circuitry. In this system (which is described in more detail in the planned Ref. [96]), we represent each RMF antenna L as an inductor paired with an associated tuning capacitor bank $C_T$ to form an LC resonator. Each of these resonators, labeled A, B, and C, forms one leg of a three-phase configuration with the antennas all terminating at a common neutral point. Currents are generated by pulsing a square wave at the resonant frequency of the antenna/capacitor resonators, in this case $\omega \approx 2.58 \times 10^6$ rad/s (413 kHz). In turn, this square wave is produced by applying voltage $V_{DC}$ from a DC power supply to a pair of backing capacitor banks $C_B$ to symmetrically float the two main power rails about ground. Therefore alternately closing switches Ch1 and Ch2 sends a square wave to antenna A whose amplitude equals the DC supply voltage centered about zero. This process is executed for each phase, offset 120 degrees from the others.

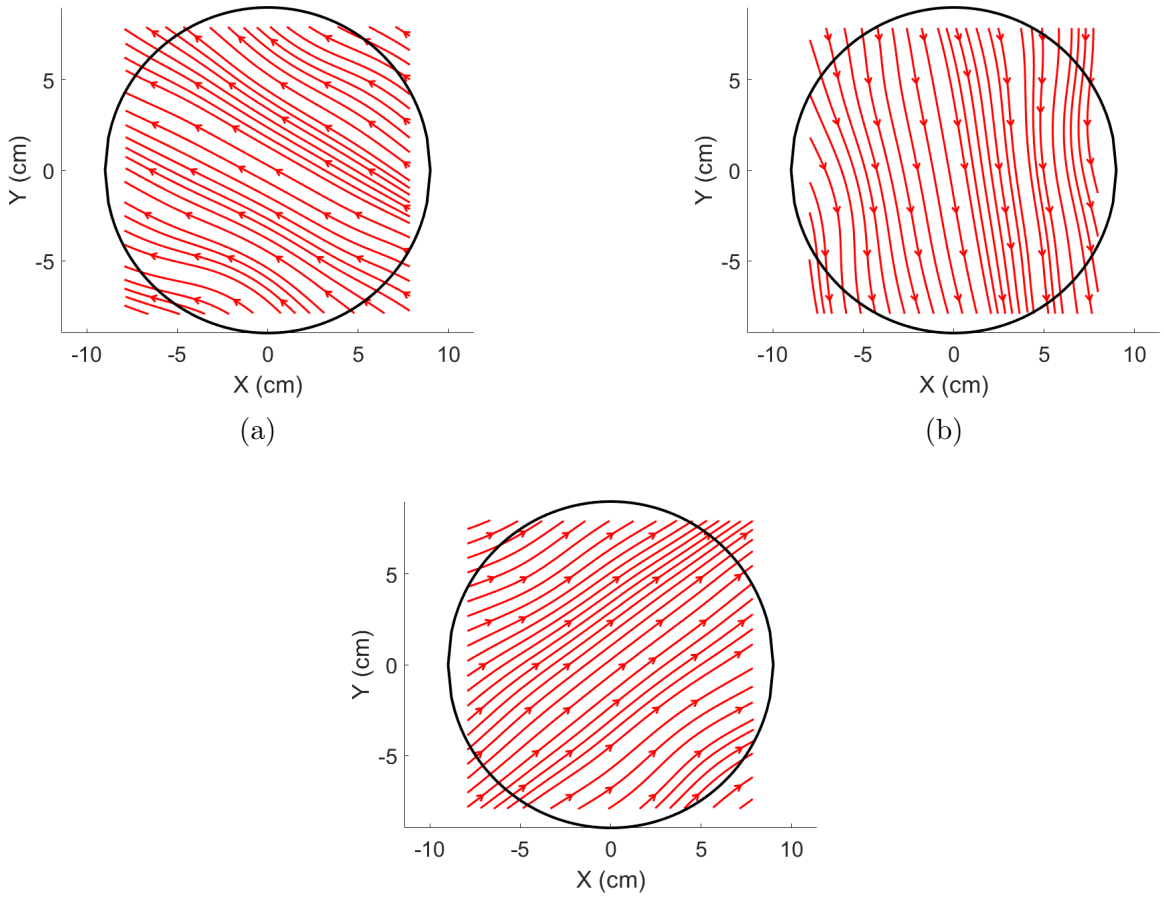


Figure 7.3: Rotating magnetic field streamlines at a) 0, b) 120, and c) 240 degrees throughout a cycle in the plane of the magnetic field reference point shown in Fig. 7.2. Black circle represents discharge chamber wall.

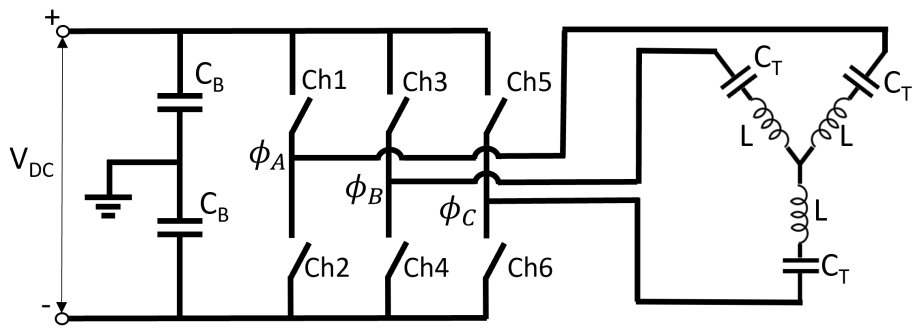


Figure 7.4: Simplified electrical diagram of the RMF generation scheme.

Ideally, the amplitude of the current delivered to each phase of the antenna is limited by real resistance and the voltage applied by the DC power supply. Power was delivered to the antennas by braiding the transmission lines in triplets to minimize total impedance and keep the stray capacitance of each line as similar as possible. However, small differences lead to different loading on each leg of the wye, which caused slightly different current amplitudes through each antenna. This contributes to the RMF strength's deviation in magnitude over a phase as shown in Fig. 7.3.

The choice of 413 kHz as the RMF frequency was made based on design limitations for the switching circuitry available. The switches used in the construction of the circuit shown in Fig. 7.4 are large steady-state devices known as IGBTs. As a general rule of thumb, an IGBT which can withstand greater electrical current also switches slower. As it is, the switches employed in this PPU were intended for operation in the 10 kHz regime. Operating at a factor of 40 beyond nominal capacity was only possible with driver circuitry heavily modified in-house. Ideally, as scaling suggest performance should improve with RMF frequency, the switching speed could be increased to allow a study on that effect. Doing so would require parallelization of smaller switches. While not unreasonable in general (and indeed, the RMFv2 PPU employed many switches in parallel) doing so requires a more complex switch activation scheme and was outside the scope of what could be accomplished in the timeframe of this campaign.

### 7.3.5 Tuning Capacitor Banks

Each tuning capacitor bank consists of a nine by five array of pulse capacitors, which combine to a capacitance of $C \approx 40$ nF, a voltage rating of 20 kV, and a CW-mode current rating of 90 A at the targeted 41e kHz RMF frequency. These capacitors are soldered to a custom high-power PCB, with the whole assembly including transmission cable pigtails potted in

hard epoxy to prevent conduction to the plasma. Power is delivered to each capacitor bank via nine parallel transmission cables (to reduce stray inductance).

### 7.3.6 Seed Ionization

Seed ionization is provided by a $LaB_6$ hollow cathode mounted downstream of the thruster exit plane, oriented backward toward the thruster. This configuration differs from the RMFv2 thruster, which employed a centrally mounted cathode at the rear of the device. This cathode was operated at 5 A discharge current with 15 sccm Xe propellant flow, typically consuming ∼100 W power. We do not include this power consumption in our efficiency calculations. The RMF antennas near the exit plane of the thruster are protected from the cathode's radiant heat via a layer of aluminum foil.

### 7.3.7 Neutral Flow

There are two neutral propellant injectors in the RMFv3. A rear wall injector is situated at the back wall of the plasma-bounding cone with downstream-facing injection holes while two side wall injectors are located along the length of the cone with azimuthal injection holes. Both injectors consist of 1/8" stainless steel tubing nested inside 1/4" stainless steel tubing. Holes are drilled in the opposite side walls of both tubes and the end is capped. This nested design serves to enhance flow uniformity by functioning as a baffle.

## 7.4 Thruster Operation

In this section we emphasize the more qualitative aspects of thruster operation to give a sense for how the test unit behaves. We begin with a discussion of how the precise RMF frequency is chosen, then discuss plume imaging for both pulsed-mode and CW-mode before finishing with a description of the RMF waveforms.

### 7.4.1 RMF Frequency Tuning

The properties of the square wave used to drive the antennas and tuning capacitors to resonance must be tuned to deliver optimal performance. While PPU design necessitates that each leg of the wye configuration described in Sec. 7.3.4 receive an input voltage of the same magnitude, the frequency and width of the pulses can be varied, both of which were useful parameters to adjust when tuning for the PEPL RMFv2 thruster. However, likely due to the three-phase operation of the RMFv3 and the tightly coupled nature of the

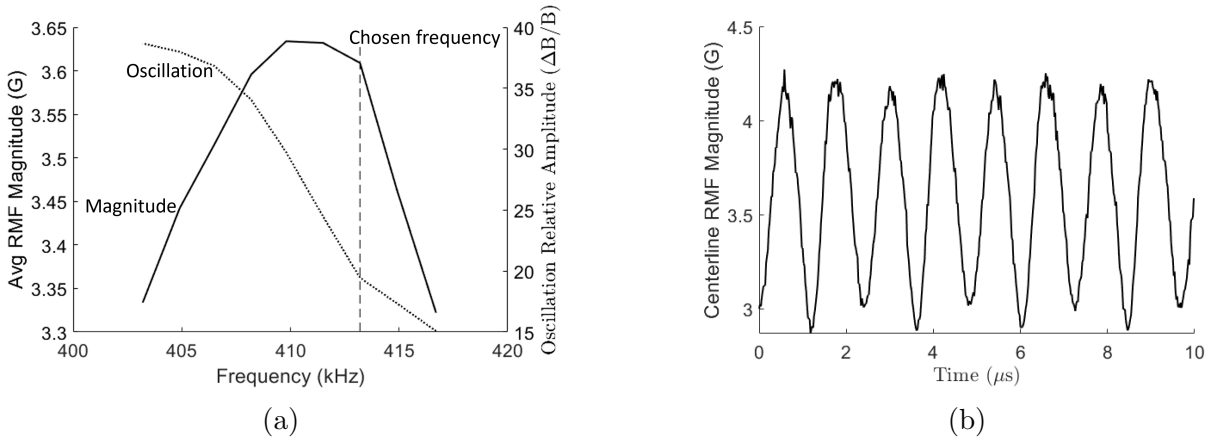


(a) (b)

Figure 7.5: RMF frequency tuning process, represented by a) the tuning parameter plot used to determine best possible frequency and b) resulting centerline RMF magnitude over time taken in the plane of field measurement shown in Fig. 7.2. Tuning process was done with 25 V from the DC supply using single shot bursts of 150 $\mu$s length.

antennas—both inductively though shared flux surfaces and electrostatically through their common neutral—adjusting the pulse width for a given antenna had little effect on relative antenna amplitudes. This left frequency as the only tuning parameter.

To perform the tuning process, current waveforms for each antenna were captured across a range of frequencies close to the anticipated resonance using a nominal backing voltage. For each frequency, these waveforms were used to superpose magnetic field maps of each antenna to create a time-resolved map of the RMF throughout a period such as those depicted in Fig. 7.3. The average strength of the RMF and relative variation across a period was then calculated at thruster centerline. Performing this process at several frequencies results in a plot such as the one in Fig. 7.5a. While RMF strength for a given backing voltage (which helps dictate total power to the plasma) is valuable, ensuring a field which rotates smoothly is also critical. Fig. 7.5a shows that while the average magnitude of the RMF is maximized at 410 kHz, the field shows nearly 60% variation at this value. Instead, the 413 kHz frequency was chosen to balance field uniformity and strength.

### 7.4.2 Plume Imaging

As this is a new device, we wish to qualitatively establish thruster operation. Fig. 7.6 shows photography of the thruster running in both pulsed-mode and CW-mode. Pulsed mode operation is established in Fig. 7.6a through a series of frames from high speed photography video taken at 150 kHz shutter speed. The formation and ejection of a mass of luminous plasma is qualitatively similar to the process captured for the RMFv2 thruster. After a

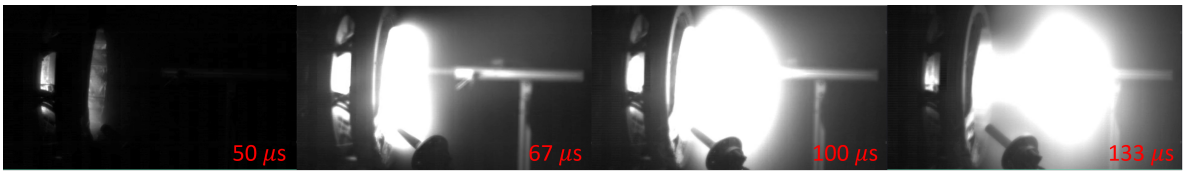


(a)

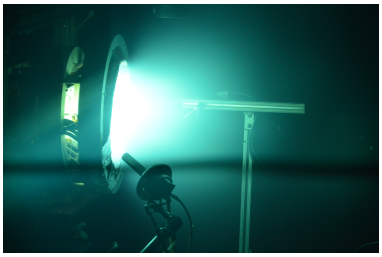

(b)

Figure 7.6: a) High speed photography taken at 150 kHz shutter speed for 275 V DC supply voltage, 200 $\mu$s pulse duration, 257 sccm rear injector flow, and bias field strength and angle of 77.3 G at 17 degrees from axis. b) Photograph of operation in CW-mode at 14 G RMF strength, 257 sccm rear injector flow, and bias field strength and angle of 77.3 G at 17 degrees from axis.

delay whose length depends on the operating parameters employed, ionization occurs and the plasma is illuminated. A mass of radiating plasma emerges from the thruster before separating from residual plasma remaining inside the thruster cone. For long pulse lengths or CW-mode operation, the RMF continues coupling to the residual plasma as neutral gas replaces the ejected mass. The photograph of CW-mode in Fig. 7.6b shows a jet of plasma emerging from the center of the thruster while less bright plasma diverges radially. When viewed with the eye, pulsed-mode and CW-mode appear qualitatively similar.

### 7.4.3 RMF Waveforms

As further evidence for energy coupling into the plasma, we can examine RMF current waveforms. Typical waveforms for both pulsed-mode and CW-mode are presented in Fig. 7.7, with all three antenna phases shown in each subfigure. We identify several important features of these waveforms beginning with the pulsed-mode waveform in Fig. 7.7a. As the RMF current is first generated by pulsing the voltage square wave in the manner discussed in Sec. 7.3.4, the amplitude rises in a smooth fashion as could be expected in a resonant circuit with some real resistance. Roughy 20 $\mu$s after the amplitude has reached its maximum, however, we note a sudden reduction in amplitude as well as the relative disparity

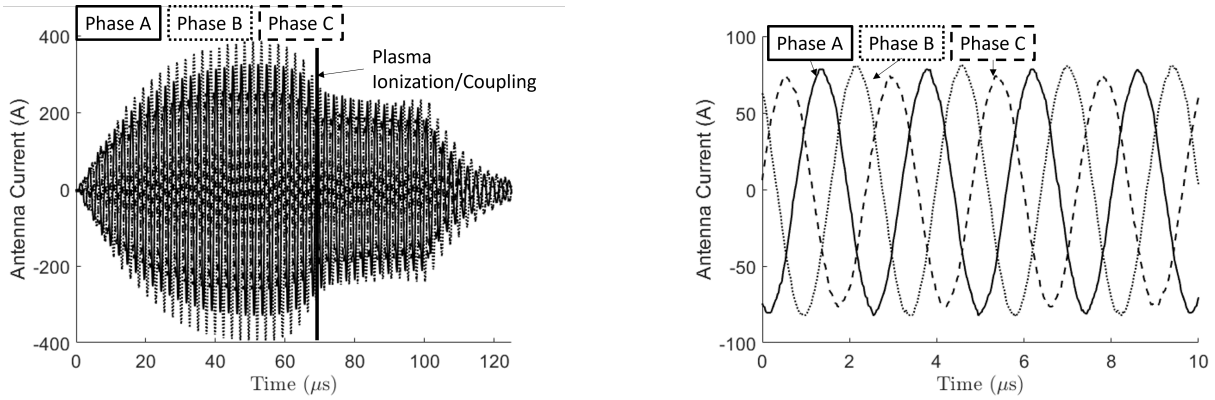


Figure 7.7: Typical RMF current waveforms for a) CW-mode and b) Pulsed-mode. CW-mode waveform captured at 100 A DC supply current, 240 sccm rear injector flow, 4.25 A main magnet current. Pulsed-mode waveform captured at 275 V DC supply voltage, 100$\mu$s pulse length, 180 sccm Xe wall injector flow, and 6 A main magnet current.

of amplitude between antenna phases. This sudden amplitude reduction coincides with the ionization of the neutral gas as viewed with high-speed photography and is caused by the enhanced coupling between the antennas and plasma. This serves to increase the effective resistance of the circuit as well as provide an additional inductive coupling mechanism between each phase of the antenna. Fig. 7.7b, which shows the CW-mode waveform, contains a factor of 10 higher time resolution to better examine the relative amplitudes of the three phases when the antenna is coupled to a plasma. After exhibiting similar start-up behavior to pulsed mode during which an initial slug of plasma is ejected, the CW-mode waveforms exhibit no large scale features of note.

## 7.5 Performance Baseline

### 7.5.1 Operating Conditions

The design of the RMFv3 thruster allows significant variation in operating conditions through the number of operating parameters. In CW-mode, this includes main bias magnet current, trim bias magnet current, neutral flow through the rear injector, neutral flow through the wall injector, and the current limit on the backing DC supply for a total of five parameters. In pulsed-mode, pulse duration and repetition rate also can be varied, leading to a total of seven free parameters. We note that the backing DC power supply is operated in voltage-limited mode in pulsed mode rather than DC current mode. This variable thus replaces

current in this parameter list.

The high dimensionality of the parameter space is problematic for fully characterizing the response of the thruster to operating condition. We therefore employed a surrogate optimization technique with operating parameters bounded as described in Tables 7.1a and 7.1b to explore and simultaneously operate performance over parameter space along with manually selected seed points from the same range. We ultimately found that thruster performance is insensitive to the relative split of flow between the upstream and downstream injectors for the CW-mode, while the pulsed-mode performs better with all neutral flow from the rear injector. Efficiency is also insensitive to the trim coil current provided the magnetic field inside the thruster is conformally similar to the distribution shown in Fig. 3.

| Parameter | Minimum | Maximum |
|---|---|---|
| DC Supply Voltage (V) | 175 | 275 |
| Pulse Length ($\mu$s) | 75 | 500 |
| Rear Injector Flow (sccm Xe) | 0 | 200 |
| Wall Injector Flow (sccm Xe) | 0 | 200 |
| Main Magnet Current (A) | 0 | 10 |
| Trim Magnet Current (A) | -10 | 10 |

(a) Pulsed-mode

| Parameter | Minimum | Maximum |
|---|---|---|
| DC Supply Current (A) | 25 | 110 |
| Rear Injector Flow (sccm Xe) | 0 | 300 |
| Wall Injector Flow (sccm Xe) | 0 | 300 |
| Main Magnet Current (A) | 0 | 10 |
| Trim Magnet Current (A) | -10 | 10 |

(b) CW-mode

Table 7.1: Operating parameters and bounds for surrogate optimization

In addition to these algorithmically-chosen operating conditions, we also tested the RMFv3 in pulsed-mode to provide seed data for the surrogate optimizer. Such seed data was necessary due to the wide combination of operating conditions which produce zero thrust. These data points were acquired in several series of tests. As a baseline exploratory study, flow rate from the wall injector was swept between 30, 60, 120, and 180 sccm Xe. At each flow condition, all combinations of pulse length between 100, 200, and 400 $\mu$s with bias magnet strength at 0, 3, 6, and 9 A main magnet current were tested for a total of 48 points. This study held in place the DC supply voltage at 275 V, the trim magnet current at no current, and the rear injector at no flow while varying repetition rate to maintain approximately 3 kW total power. Further data was taken in similar fashion to provide information for a range

of bias field shapes, DC supply voltages, and duty cycles.

For the CW-mode, seed data was acquired by sweeping the DC supply current limit from 70 A to 100 A while varying magnetic bias field strength and flow rate. It was observed that after a given field strength, the RMF would fail to achieve ionization. At this point the flow and RMF amplitude would be increased until ionization occurred, then the magnetic field increased again. This process was repeated at intervals of 15 A DC current limit up to a maximum of 240 sccm Xe flowed through the wall injector and 5 A main magnet current to provide a wide array of seed points for the surrogate optimizer. After performing the surrogate optimization for the CW-mode, supplemental operating points were manually selected at higher power than the surrogate optimizer was allowed to submit. For these points, we held constant DC backing current at 150 A, rear injector flow at 257 sccm Xe, and wall injector flow at 0 sccm Xe, while increasing magnet strength from 4.02 A main/0.63 A trim to 8.04 A main/1.26 A trim.

To produce the figures shown in Sec. 6.4.4, points were selected from this larger set of performance measurements to form data series with varying bias field strengths with all other parameters held constant. For the pulsed mode, we identified four flow conditions (30, 60, 120, and 180 sccm Xe) and three pulse lengths (100, 200, and 400 $\mu$s) which meet this criterion. All of these points share an identical magnetic field shape as shown in Fig. 7.2 and neutral flow location with all flow originating from the rear injector. Because antenna-plasma coupling manifests as effective resistance in the RMF antenna circuit, the varying densities and magnetic fields represented across these points preclude exact prescription of RMF strength. However, all pulsed-mode performance measurements shown here use a DC backing voltage of 275 V which approximately corresponds to an RMF strength of $\sim$45 G.

For the CW-mode, two series were identified to isolate the effect of changing bias field strength: one with 240 sccm Xe and 13.6 G RMF strength, and another with 257 sccm Xe and 20.5 G RMF strength. Both these series of points exclusively use the wall neutral injector. Unlike the pulsed-mode, the current-limited nature of CW-mode operation allowed the RMF strength to be constant across each data series.

### 7.5.2 Surrogate Optimization

In this section we address the efficacy of the surrogate optimization procedure used to supplement our manual exploration of operating parameter space. Fig. 7.8 shows the efficiency measured against the trial number for both pulsed-mode and CW-mode. Fewer total algorithmically-chosen data points exist for the pulsed-mode rather than the CW-mode due to campaign time constraints and the relatively larger number of manual points taken in the

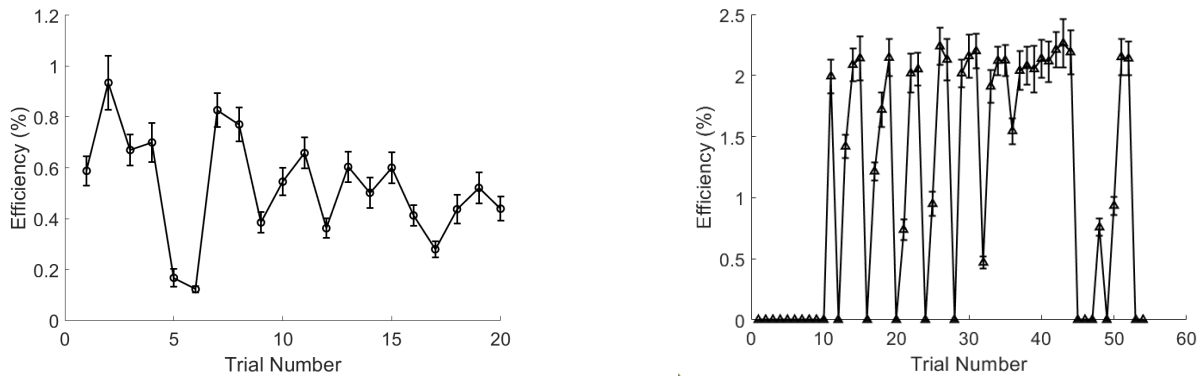


(a) (b)

Figure 7.8: Summary of surrogate optimization results for a) pulsed-mode and b) CW-mode operation.

pulsed-mode.

The pulsed-mode surrogate optimizer was not able to locate substantially improved performance conditions over the manually chosen points which were used to seed it. Many of the requested conditions sought to further explore the effect of changing the bias field's shape by strongly reversing the trim coil or to employ only the trim coil. The relatively few number of points which we were able to allow the surrogate optimizer to examine may have adversely impacted its ability to locate an optimum, or it could be that there is no easy correlation between operating parameters and efficiency for this device in the pulsed-mode in contrast to the CW-mode.

The CW-mode surrogate optimization, meanwhile, struggled due to the bias field's plasma quenching effect discussed in the previous subsection. After the first 10 points of exploration and moving to an adaptive mode, the algorithm would request points with increasing bias field strength until the RMF could not support ionization, then reset to similar starting parameters and begin again. This process repeated many times, as can be seen from the sawtooth-like pattern in the trial number versus efficiency plot in Fig. 7.8b. We hypothesize that the highly non-smooth behavior associated with the plasma quenching is difficult for the adaptive modeling algorithm to learn. With this being said, the surrogate optimizer was able to achieve higher efficiencies than we had by manually adjusting the operating conditions. The highest efficiency points resulted from our extrapolation of the same trends explored by the optimizer to higher RMF amplitudes than we had allowed it due to power supply limitations.

### 7.5.3 Global Performance Trends

For the pulsed mode, efficiency peaks at a value of $\eta = 1.04 \pm 0.11\%$ with $T = 10.26 \pm 0.74$ mN thrust and a specific impulse of $I_{sp} = 528.53 \pm 41.71$ s. This corresponds to a DC supply voltage of 275 V, with 400$\mu$s pulses at 75 Hz repetition rate. Neutral flow was partially through the wall injector at 90 sccm and partially through the rear injector at 30 sccm, and the magnetic field magnitude was 162 G at an angle of 19.4 degrees from the horizontal. For the CW-mode, efficiency peaks at a value of $\eta = 2.56 \pm 0.28\%$ with $T = 139.36 \pm 10.53$ mN thrust and a specific impulse of $I_{sp} = 575.1 \pm 43.89$ s. This setpoint corresponds to 150 A DC supply current, 257 sccm Xe rear injector flow, and a magnet strength and angle of 135.4 G at 17.31 degrees from the axis. This point is a relative outlier as it required the PPU to be pushed above its rated limits, drawing approximately 15.3 kW. As such it is outside the bounds of the surrogate optimizer. The highest performance case within bounds of the surrogate optimizer is $\eta = 2.26 \pm 0.20\%$ with $T = 105.15 \pm 6.33$ mN thrust and a specific impulse of $I_{sp} = 426.07 \pm 26.05$ s. This setpoint corresponds to 109 A DC supply current, 262 sccm Xe rear injector flow, and a magnet strength and angle of 74.56 G at 18.26 degrees from the axis. From these data we see that efficiency is improved by roughly a factor of five by changing to CW-mode from pulsed-mode with no reduction in thrust-to-power.

Because these results take into account the coupling efficiency, which includes losses inside the PPU and antennas, it can be helpful to instead eliminate coupling efficiency by using the post-coupling or plume efficiency $\eta_{plume} = \frac{\eta}{\eta_c} = \eta_d \eta_m \eta_p$. While the plasma properties and antenna design are certainly important characteristics to the thruster, the PPU was designed and assembled in-house, and many of its losses have little to do with RMF thruster physics. For example, much of the power lost to coupling efficiency is believed to be converted to heat in the switches which produce the voltage square wave delivered to the antennas. The switches used were intended for the 10 kHz range, while we drive them at 413 kHz to produce the RMF signal, a feat made possible using house-made driver boards. Operating so far out of spec increases the lossiness of the switches and therefore reduces overall thruster performance. The post-coupling efficiency of the same best performance pulsed-mode condition mentioned above is $\eta_p = 4.12 \pm 0.49\%$, while the post-coupling efficiency of the highest performing CW-mode condition is $\eta_p = 13.02 \pm 1.50\%$. For these cases, then, the performance uplift associated with CW-mode operation is due to post-coupling loss reduction rather than enhanced coupling.

These most performant points mentioned above occur at different operating conditions, making direct comparison difficult. Pulsed-mode and CW-mode data were therefore taken at the same flow rates and magnetic field strength with maximum RMF amplitude allowable by our PPU for each. These points were taken with 257 sccm Xe rear injector flow and

with a bias field strength of 78 G at an angle of 17.1 degrees from the horizontal. Pulsed-mode RMF strength was 55 G, while CW-mode RMF strength was 20.4 G. This resulted in pulsed-mode efficiency of 0.55±0.08% while CW-mode efficiency was 2.01±0.16%. We thus see a ∼3.6 times increase in efficiency between like operating conditions when transitioning from pulsed-mode to CW-mode.

Fig. 7.9 displays the performance data gathered across all 200 operating conditions tested between pulsed-mode and CW-mode. The data, which include efficiency, post-coupling efficiency, thrust, and specific impulse, are plotted versus specific energy (or coupled specific energy in the case of post-coupling efficiency). Specific energy is calculated for the pulsed-mode by dividing the energy per-pulse by the slug mass per-pulse, while it is calculated for the CW-mode by dividing total power by mass flow rate. Coupled specific energy is calculated by multiplying specific energy by the coupling efficiency to arrive at the amount of energy which the plasma actually receives. The performance data is plotted in this fashion because a positive correlation between specific energy and performance was the primary trend observed for the RMFv2 thruster [94]. This trend is also observed for the CW-mode cases here, where efficiency, thrust, and specific impulse all show an approximately linear correlation with specific energy. However, the pulsed-mode does not appear to share this effect. Instead, thrust appears to trade with specific energy as could be expected for a device whose efficiency does not depend on specific energy. Overall, performance for the CW-mode operating conditions tends to be superior to that of the pulsed-mode conditions across all points excepting those zero-thrust points for which the CW-mode is prone. The highest performing pulsed-mode points are roughly on par with the lowest performing CW-mode points across all four quantities shown in Fig. 7.9.

### 7.5.4 Pulsed-Mode Bias Trends

Fig. 7.10 shows performance trends for the pulsed-mode with pulse length, flow rate, and bias field. Performance for these points is seen to peak at 0.96±0.14% at the 180 sccm xe, 400 $\mu$s, 162 G bias field condition. While this is a significant improvement over the previously published maximum efficiency for the RMFv2 thruster of 0.47±0.08%, it is still very low. Apart from noting this peak value, we identify three key trends for this data we wish to emphasize.

Most significantly, we do not see the expected trend of monotonic improved performance with bias field strength that would be predicted by established theory from Sec. 7.3.4. Instead we find that for the shortest pulse length conditions, increasing the bias field causes monotonic reduction in performance. Indeed, after a threshold field strength which depends

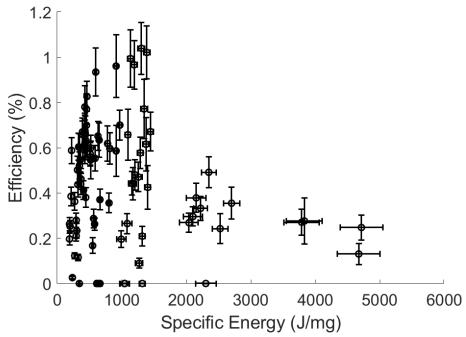


(a)

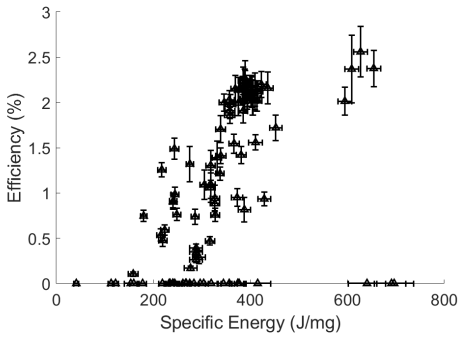


(b)

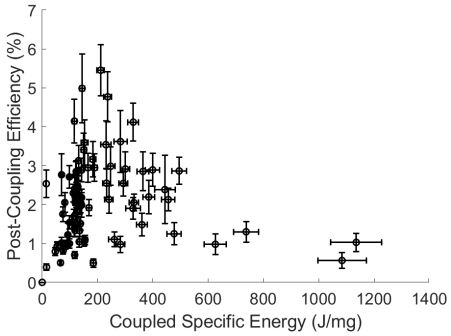


(c)

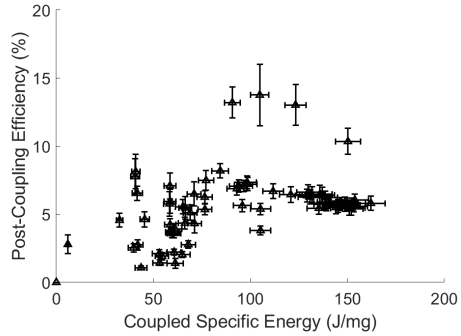


(d)

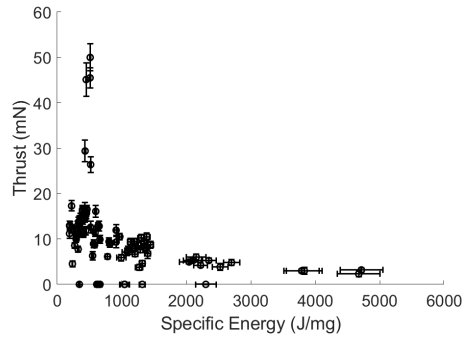


(e)

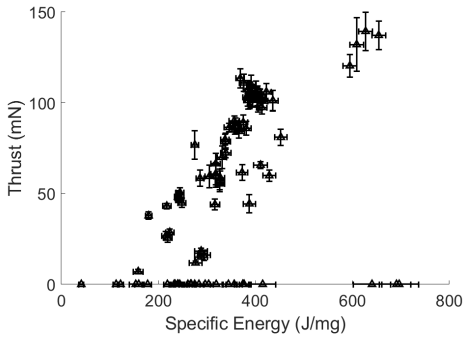


(f)

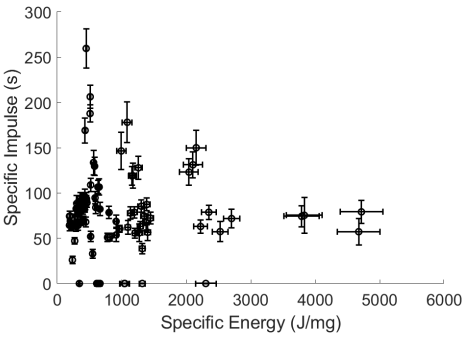


(g)

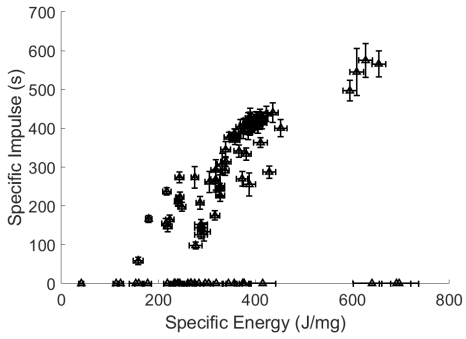


(h)

Figure 7.9: Performance data across all thruster setpoints, including a) and b): total device efficiency versus specific energy; c) and d): post-coupling efficiency versus coupled specific energy; e) and f): thrust versus specific energy; and g) and h) specific impulse versus specific energy. Left column plots (a,c,e,g) refer to pulsed-mode data while right column plots (b,d,f,h) are for the CW-mode.

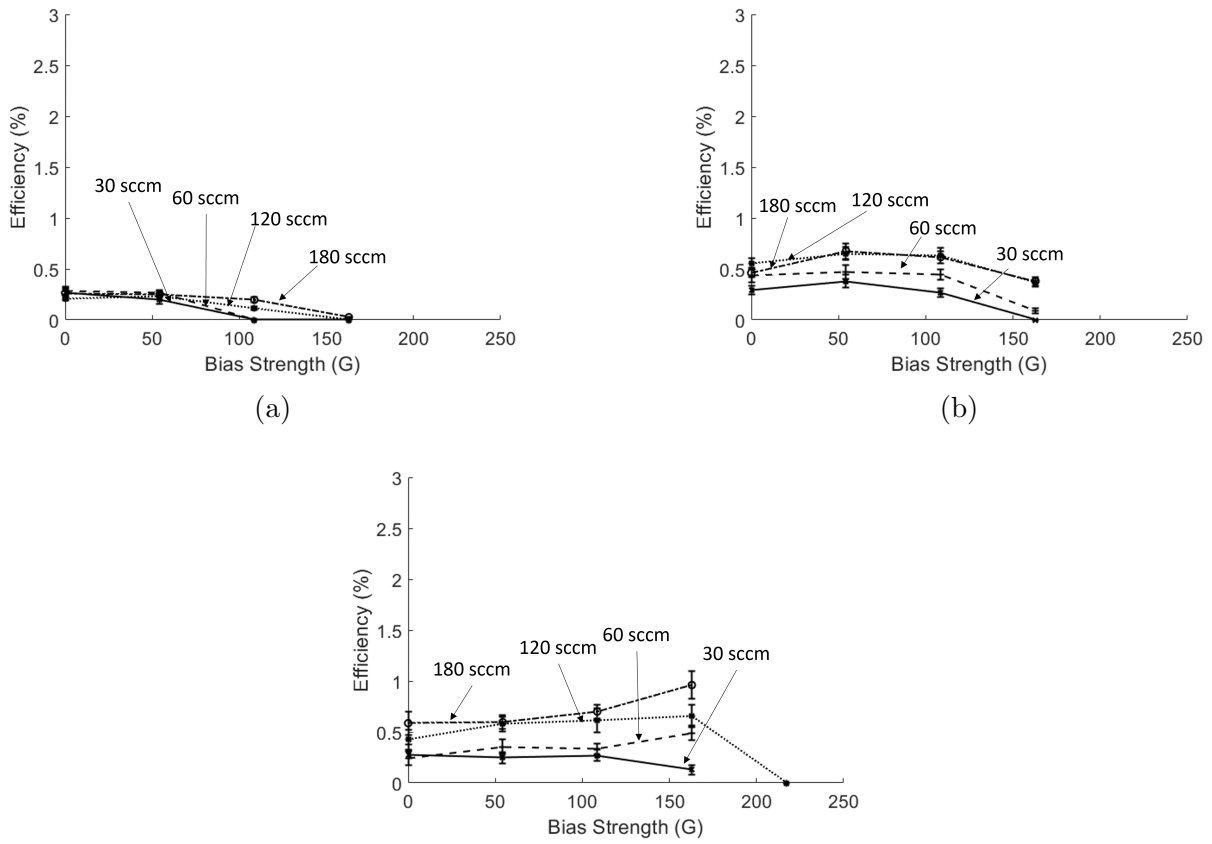


Figure 7.10: Trends across bias strength and flow rate for a) 100 $\mu$s pulse length, b) 200 $\mu$s pulse length, c) 400 $\mu$s pulse length. All pulsed mode data taken at 275 V DC supply voltage and all flow through the rear injector

on the flow rate, zero thrust is measured as the RMF entirely fails to ionize the propellant, with lower flow rates experiencing this effect more readily. All flow rates experience this phenomenon, which we will refer to as 'discharge quenching' for the rest of this work, by the 162 G condition, while the 30 and 60 sccm cases show discharge quenching at 108 G. At the 200 $\mu$s pulse length, a clear performance maximum is observed with bias field strength before we again observe discharge quenching. The effect is reduced here relative to the 100 $\mu$s conditions, with only the 30 sccm series exhibiting the effect and not until 162 G bias strength. Performance for the 400 $\mu$s cases is significantly flatter with bias field, and no flow rates experience discharge quenching by the 162 G condition. However, an additional, stronger bias field point was taken for the 120 sccm flow rate which does show quenching at 217 G. We conjecture based on this pattern, then, that the other flow rates would show similar behavior with bias quenching occurring at this higher field strength.

The second trend we wish to highlight is a general improvement with pulse duration. Globally, performance is observed to increase as the pulse length increases. While this could be due in large part to the discharge quenching effect, we also speculate that the coupling time discussed in Sec. 7.4.3 may play a role. This is because any time during which the RMF is energized but the plasma is unionized represents a period of inefficiency as power is lost to Ohmic heating in the power circuitry and transmission lines, but no power is delivered to the plasma. Therefore, for efficient operation the coupling time must be small as a fraction of the total pulse length. This effect is not endemic to the RMF thruster, and indeed is a challenge shared by all pulsed electromagnetic thruster concepts [78]. In light of this, the longer pulses may simply have fractionally less power wasted while no plasma is present.

Finally we identify trends with flow rate. Across all pulse lengths and bias field strengths, increasing flow rate tends to increase performance up to a point. This effect is most significant going from 30 sccm to 60 sccm and from there to 120 sccm, but 120 and 180 sccm show very similar efficiencies. We note that although the data is not pictured here and is outside the scope of this paper's focus on bias field trends, increasing flow rate above 120 sccm was not found to significantly improve performance. Indeed, the highest pulsed-mode efficiency point measured on this device occurred at 120 sccm split 3/4 through the rear injector and 1/4 through the wall injector which achieved an efficiency of $\eta = 1.04 \pm 0.11\%$. Further, a data point taken at the same conditions as the best CW-mode condition discussed below achieved an efficiency of $0.55 \pm 0.08\%$. A reduction in performance with increased flow rate is not altogether unexpected given the motivation for CW-mode operation. Excitation radiation, the highest loss mechanism calculated for the RMFv2 thruster, scales quadratically with electron density. Taken together, we draw the conclusion that a certain plasma density is required for effective coupling and ionization, but too much flow enhances losses prohibitively.

### 7.5.5 CW-Mode Bias Trends

Fig. 7.11 shows the result of increasing bias field strength on efficiency for the CW-mode. As with our discussion of the pulsed-mode data, we wish to highlight the chief takeaways from this figure.

Immediately, we note the much higher performance enjoyed by these CW-mode points than the pulsed-mode data shown above, with peak efficiency of $\eta = 2.56 \pm 0.28\%$, nearly a factor of 3 greater than what is displayed in Fig. 7.10. Indeed, a direct comparison not shown in this figure was made with 257 sccm Xe rear injector flow and with a bias field strength of 78 G. Pulsed-mode RMF strength was 55 G, while CW-mode RMF strength was 20.4 G. This resulted in pulsed-mode efficiency of $0.55 \pm 0.08\%$ while CW-mode efficiency was

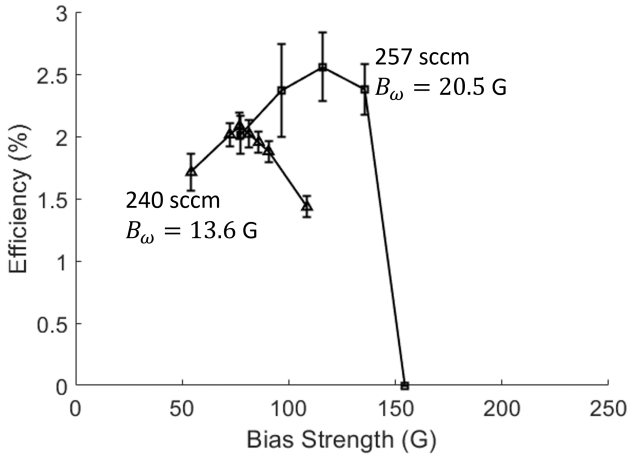


Figure 7.11: Trends across bias strength and flow rate for the CW-mode with all neutral flow through wall injector.

2.01±0.16%. We thus see a ∼3.6 times increase in efficiency between like operating conditions when transitioning from pulsed-mode to CW-mode. However, the different conditions used throughout the vast majority of this study prevent us from making a definitive and rigorous statement as to the superiority of CW-mode via direct comparison.

Next, we again see the phenomenon that an optimum bias field occurs for both data series represented along with discharge quenching at the highest field considered. However, the optima for CW-mode appear much more sharply peaked than those for the pulsed-mode. In addition, where the pulsed-mode peaks were seen to occur at roughly the same value of bias field strength across all flow rates for a given pulse length, these two curves show bias strength optima separated by nearly a factor of two. Significantly, however, both optima here occur at the same ratio of bias strength to RMF strength $\frac{B_0}{B_\omega} \approx 6$. We speculate that if pulsed-mode data were to be taken at varying RMF strengths as well, we might find a similar shift in ideal bias field. As an aside, we note that throughout thruster characterization the CW-mode as a whole was found to be far more susceptible to discharge quenching than the pulsed mode. We might attribute this phenomenon either to the typically lower RMF magnitudes associated with operating at steady state, or to the lower predicted densities at a given flow rate caused by the steady acceleration of ions and electrons from birth. Without an updated theory to account for this behavior, however, we cannot definitively state the cause.

Last, these points also occur at much higher flow rates than were seen to be effective for the pulsed-mode. Attempts to operate the thruster at the lower flow rates which were ideal for pulsed operation resulted in discharge quenching at the CW-mode. This may be

due to the lower particle density available for ionization which is an exponential process. In other words, it is a combination of RMF strength and density which is required for initial ionization and coupling to occur. The two data series for CW-mode in Fig. 7.11 show very different performance, with the 257 sccm peak roughly 25% greater than the 240 sccm peak. Because the fractional difference in flow rates is much less than this performance gap, we might expect that the RMF strength is primarily responsible for the enhanced performance of the latter data series.

## 7.6 Discussion

In the following section, we discuss the results from Sec. 6.4.4 in the context of the questions which motivated this study. We will address the performance differences between pulsed-mode and CW-mode, the role of the bias field in improving performance, and strategies to improve the device further.

### 7.6.1 Discharge Quenching by Bias Field

One of the most significant results from this campaign is the impact of the bias field strength on thrust. In particular, the behavior that increasing the bias field too far beyond the relative strength of the RMF causes zero thrust is an unexpected result for the established theory. Further, that applying the bias field after the RMF discharge has been activated in CW-mode still causes quenching for sufficient bias field strengths implies that this effect is related to the steady-state current drive mechanism in the thruster, rather than simply a startup effect. Given the dramatic increase to magnetic field strength allowed before quenching occurs in Fig. 7.11 when the RMF is increased, we expect that for either the pulsed-mode or the CW-mode, the RMF must be commensurately increased with the bias field to access enhanced performance. In light of this non-ideal effect, increasing the Lorentz force experienced by the plasma is not as simple as 'turning a knob' by increasing the bias field strength. Rather, it is likely that a combination of parameters must be adjusted to reduce wall losses and increase thrust so that greater bias field strengths can be achieved without losing the discharge.

One explanation for this behavior is that the bias field is able to retard azimuthal electron velocity via some mechanism not considered in the Blevin and Thonemann analysis. This is supported by examining the plasma coupling time, which we define as the time for which the RMF is active but ionization and current drive have yet to occur in the plasma, indicated for example in Fig. 7.7 by the solid vertical line. To determine the coupling time for each pulsed-mode condition, we examine the RMF antenna current waveforms. In each case,

an instant can be identified when the amplitude necks down due to antenna/plasma mutual inductance effectively increasing RMF circuit resistance. We show this coupling time plotted against the empirical parameter $\frac{B_0}{\dot{m}}$ in Fig. 7.12. We note that such behavior is supported by our updated model for RMF current drive (Eq. 2.22) in which azimuthal electron velocity is retarded by the bias field. A lower electron velocity would inhibit the energy deposited into the free electrons in the seed plasma, eventually preventing them from gaining enough energy to achieve mass ionization altogether.

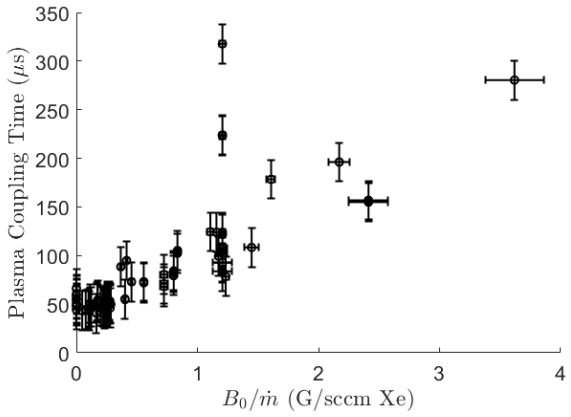


Figure 7.12: Empirical correlation between bias field strength, mass flow rate, and coupling time.

We motivate the use of the parameter $\frac{B_0}{\dot{m}}$ in this analysis by referring back to our conjecture that this behavior is dictated by the bias field's ability to retard electron motion. $\frac{B_0}{\dot{m}}$ can be considered a proxy for the bias field Hall parameter $\Omega = \frac{eB}{m_e \nu}$, a quantity which describes the degree to which electrons are tied to a magnetic field. As the bias field is strengthened, therefore, we might expect that they are less able to follow the rotating magnetic field for the same reason we might expect enhanced radial confinement. Thus azimuthal current and therefore ionization is slowed. Significantly, this effect is not predicted by the derivation for expected plasma current in the established model in Sec. 2.3.2, in which the bias magnetic field strength has no bearing on the azimuthal drift speed of the electrons, only on their density distribution.

The positive relationship between coupling time and bias field strength can help explain the phenomenon observed in Fig. 7.10 that higher pulse lengths are better able to tolerate increased bias strengths. For coupling to occur within a shorter pulse duration, the bias field strength must also be low. As the pulse length is increased, the bias field may be increased while maintaining a reasonable coupling time as a fraction of pulse duration. Meanwhile, we might expect an ideal magnitude for RMF magnitude based on Eq. 2.25: once $B_\omega$ is high

enough relative to the density for the denominator to approach unity, any additional amplitude only results in Ohmic heating in the transmission lines and power switching circuitry. Therefore what we observe can be explained as the allowable ratio of $\frac{B_0}{\dot{m}}$ increasing with pulse length while $\frac{B_\omega}{\dot{m}}$ remains fixed.

As discussed in Chapter 1 the RMF thruster's main CW-mode advantage over more traditional inductive pulsed plasma thrusters is that the plasma current relies on the RMF frequency rather than magnitude [19]. This would allow for significantly easier PPU design, as the peak currents—and therefore transient voltages—are far less, with 30 kV and 100 kA peak values for the PIT Mk V [35] compared to the ≈10 kV and 400 A in the pulsed mode for the RMFv3. However, if increasing the bias field requires an increase to the RMF, this advantage may not be relevant for practical operating conditions. If the fundamental scaling limits of the RMF thruster are to be understood, it is key to understand the relationship between current drive, bias field, and RMF strengths. We therefore believe it is imperative as the next step in RMF thruster research to derive an updated theory of operation to better understand performance limitations of this device.

### 7.6.2 CW-Mode Versus Pulsed-Mode

A primary motivator behind the design of this thruster and PPU was to investigate CW-mode behavior for the RMF thruster. While performance in both pulsed-mode and CW-mode remain low, with pulsed-mode exhibiting no improvement over past designs, we report a roughly two and a half-fold increase in efficiency between the most performant CW-mode and pulsed-mode points, a number remarkably close to the factor of three predicted by our previous zero-dimensional analytical modelling [89]. Further, the difference in performance between operational modes is due specifically to plasma-based effects as coupling efficiency for these top cases are both the same $\eta_c \approx 31\%$, again agreeing with the hypothesis motivating the CW-mode investigation. We therefore expect that our attempt to minimize losses by reducing the plasma densities was a success, although a full efficiency breakdown contrasting those two operating conditions is ongoing at the time of writing. We caveat this discussion with the note that the CW and pulsed operating modes were not compared over a wide range of like conditions. The impact of this this conclusion is reduced as it is based on a few isolated examples and comparison over unlike operating points. With this said, we anticipate that an updated model for thruster operation which takes into account the bias field trends shown in this paper will shed light on this matter as discussed in Chapter 8.

## 7.7 Conclusions

This chapter has detailed the design and baseline performance for the RMFv3 thruster. We began by outlining the motivation for the creation of this test article by citing the heavy wall and radiation losses in the RMFv2 which we speculate can be alleviated through CW-mode operation and/or enhanced bias field strength. We then gave a description of the thruster design before discussing the qualitative aspects of thruster operation including RMF waveforms, plume imaging and propagation, and how the RMF frequency is tuned to produce the most uniform and highest amplitude field possible. Next we presented the results of our baseline performance characterization campaign. These were primarily split between global results, guided by surrogate optimzation, and those focusing on the effect of the bias field on performance. We found that by far the strongest trend was that there exists a performance optimum with bias field strength, something which is not expected at all from the Blevin and Thonemann RMF current drive model but does follow from our updated theory. These results are then discussed in the context of thruster performance and next steps, with the critical conclusion that the updated RMF theory must be validated experimentally.

Ultimately, the two chief takeaways we wish to highlight from these results are that a) CW-mode appears to be superior to pulsed-mode operation, although more data at like operating conditions is warranted to complete this conclusion, and b) the performance trends with bias field strength do not match with the established theory, but our updated model provides explanation for the behavior observed. Therefore it is imperative to experimentally determine the accuracy of our new model to understand the performance limitations of this device.

# CHAPTER 8

# The PEPL RMFv3 Thruster: Understanding Performance Limitations

## 8.1 Introduction

In this section we seek to explain the performance trends shown in Chapter 7 by using inductive probing to show the application of our updated RMF current drive theory, then discuss how this theory predicts limited performance in this regime. To do so, we begin by listing the operating conditions for which the probing was conducted. This is followed by a discussion of general trends when considering inductive probing on the RMF thruster. Next current density experimental measurement is compared to theory. Finally these results are discussed in the context of thruster behavior and the direction of future research effort.

## 8.2 Operating Conditions

In this study we are primarily concerned with varying bias and rotating magnetic field strengths to examine their effect on current drive. Further, we focus on pulsed-mode probing due to the high signal strength associated with the strong currents in that mode. To that end, we examine operating conditions which vary main bias magnet current as measured at the same location as shown in Fig. 7.2 from 0 G to 109 G at 200 V and 275 V backing voltage, and 0 to 91 G for 350 V DC backing voltage. For each series of points, we hold neutral injection flow constant at 120 sccm Xe through the wall injector with 200 $\mu$s duration pulses and the trim magnet off to eliminate the effect of a changing bias field shape. When we compare the model directly to experiment, we use the 350 V series, although the general conclusions are the same for the other two.

## 8.3 Inductive Probing Trends

To establish similarity of operation between this device and previous published work, we first present magnetic field data throughout a pulse for an example condition in Fig. 8.1. We observe qualitative similarity to data taken on the PEPL RMFv2 thruster [76]. Current is driven, resulting in an induced magnetic field opposite the bias field and exceeding it near centerline. A separatrix forms around the location of lowest net field strength, which propogates axially downstream and dissipates as propellant is ejected, reducing the electron density available to generate current and sustain the FRC plasmoid's shape. Significantly, this test condition therefore belongs in the regime by which radial electron pressure balance can be achieved between thermal and magnetic effects. In the Blevin and Thonemann current drive model, we would therefore expect that $1 < \frac{4\pi B_0}{\mu_0 N_0 e \omega} < 2$ assuming Eq. 2.27 is satisfied. Having verified FRC formation in the thruster at a nominal condition we examine trends across all points considered. Fig. 8.2a shows peak induced plasma current across the range of bias strengths for three backing voltages which approximately correspond to separate RMF amplitudes. A clear peak in the induced current is observed across all three series. Both the value of that peak and the bias field strength associated with it increase as the RMF is increased.

The drift velocity in Eq. 2.22 explains both the increased value of current with enhanced RMF strength and the reduction of current with enhanced bias field strength. This is because the first term in Eq. 2.22, $\frac{-E_z B_r}{|B|^2}$, scales approximately as $v_\phi \approx \frac{\omega r}{\left(1+\frac{B_0}{B_\omega}\right)^2}$. As the RMF strength is increased relative to the bias strength, this scaling factor approaches unity, allowing the drift velocity to approach its ideal value. Meanwhile, the low currents driven at low bias field strengths can be explained by our assumptions in arriving at the electron density in Eq. 2.20, which require a radial pressure balance. In the case of a bias field which is weak enough to be reversed everywhere—as is approximately true for the 0 and 18 G magnet conditions for the 350 V series as is seen in Figs. 8.4a and 8.4b—we expect high recombination rates due to electron/wall contact. Thus our assumption of full ionization is broken for these conditions. Taken together, this current drive optimum should be expected from our updated current drive model. However, the lack of mechanism by which an enhanced bias field can retard current drive means that the Blevin and Thonemann model does not explain this behavior sufficiently.

In Fig. 8.2b the net impulse imparted to the plasma by the Lorentz force follows a similar but not identical trend to the peak currents. Although higher currents can be expected to correlate with higher impulse owing to Eq. 2.34, the bias field's retarding effect on current drive at high strengths is mitigated by the the Lorentz force's dependence on the radial bias

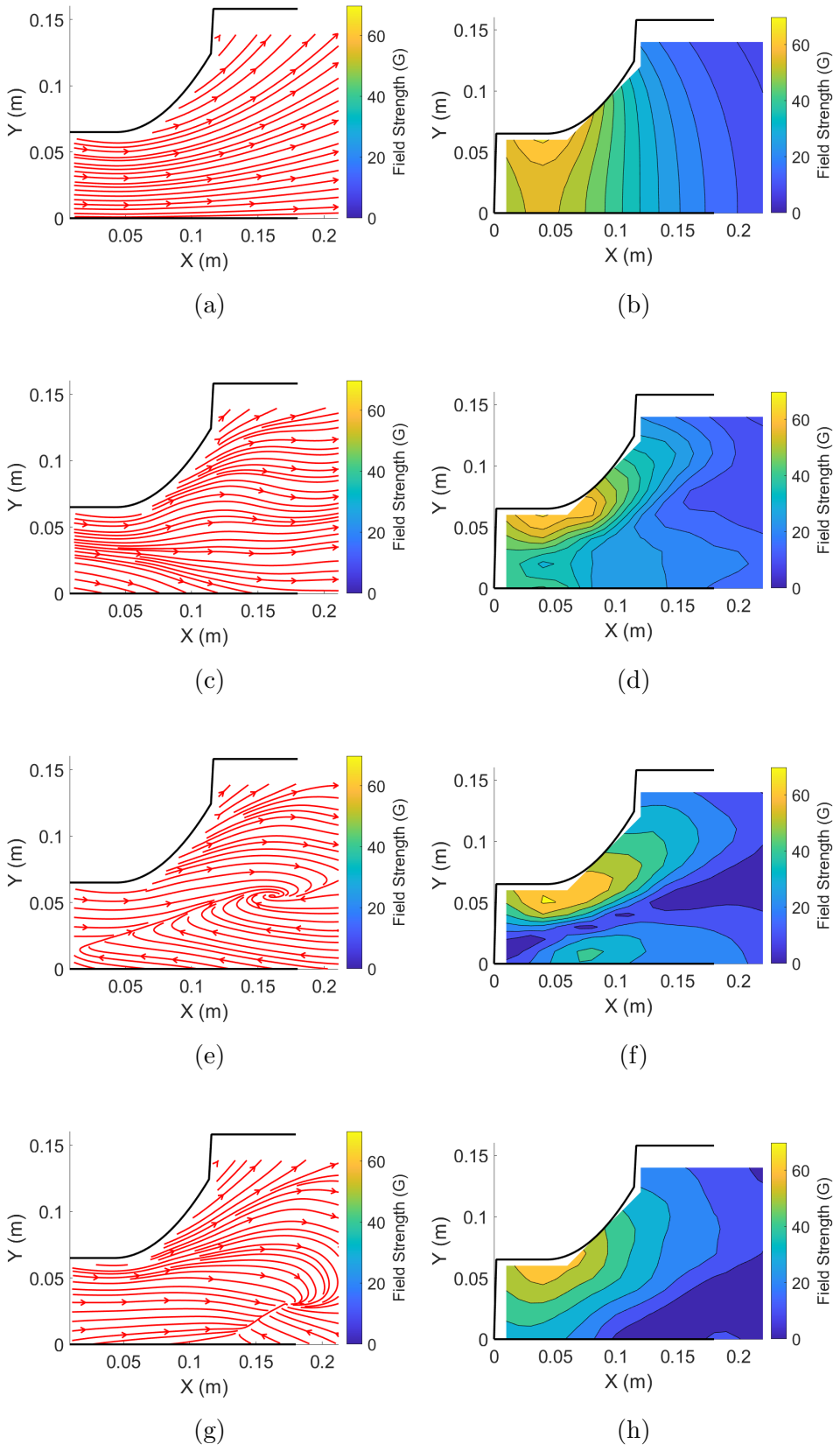


Figure 8.1: Magnetic field streamlines and strength for the 350 V DC backing voltage, 54 G main magnet current condition throughout the 200 $\mu$s pulse: Pre-pulse (a,b), 80 $\mu$s (c,d), 120 $\mu$s (e,f), 160 $\mu$s (g,h)

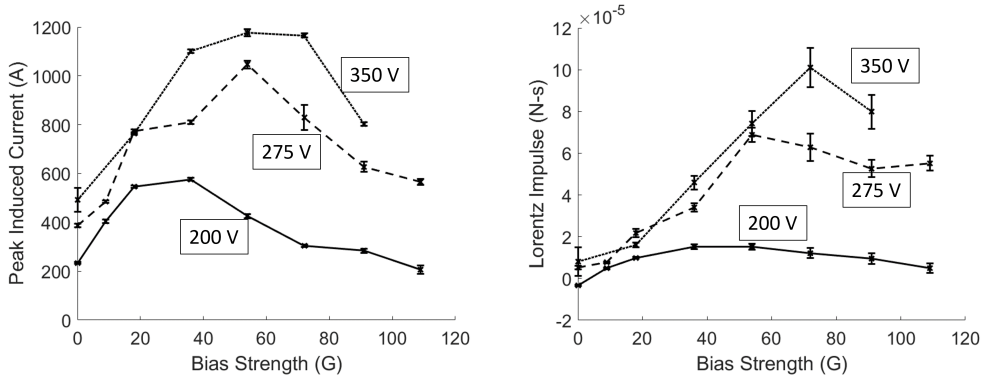


(a) (b)

Figure 8.2: Trends across all operating conditions: a) peak current and b) total Lorentz impulse per shot

field strength. This helps to explain why the impulse does not decrease as quickly as the peak currents after the peak of a given series.

To gain further insight into the current drive at various bias field strengths we plot in Fig. 8.3 the total induced current over time for every condition we examined in Fig. 8.2. First focusing on the 350 V case, we find that at low bias strengths (0 and 18 G magnet current) ionization of the plasma tends to occurs relatively quickly but peak currents remain low. The current then remains near its maximum value throughout most of the pulse. This behavior suggests that although the bias field is not strong enough to significantly impede current drive, the plasma experiences lower levels of ionization due to the tendency for recombination at the thruster walls where we expect high electron densities owing to the strongly reversed field structure. In addition, the relatively constant sustained current is consistent with the low Lorentz force measured for these conditions as the plasma remains in the cone and is not rapidly ejected. For the 36, 54, and 72 G conditions, sharper and taller peaks form, but ionization onset is delayed relative to the low field conditions by the increased bias magnitude. The current also decays much more quickly, which may be interpreted as the plasma having been exhausted from the thruster. Finally at the 91 G condition, ionization is significantly delayed and peak currents are again reduced.

These trends are replicated for the 275 V and 200 V cases with some changes which can be ascribed to the lower RMF amplitudes. In particular, we see the effects of delayed ionization become more readily apparent. At the 91 G condition the current drops off sharply at exactly the 200 $\mu$s point, suggesting that it had yet to reach its natural peak value if the pulse were allowed to continue. This holds as well for the 6A case.

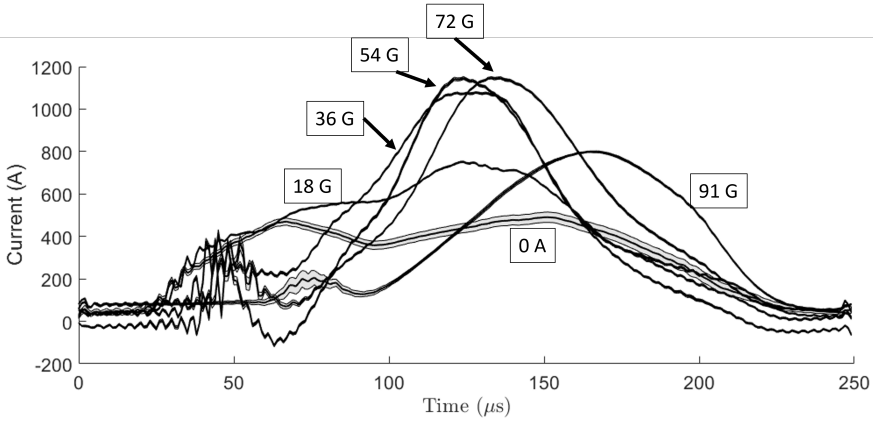


(a)

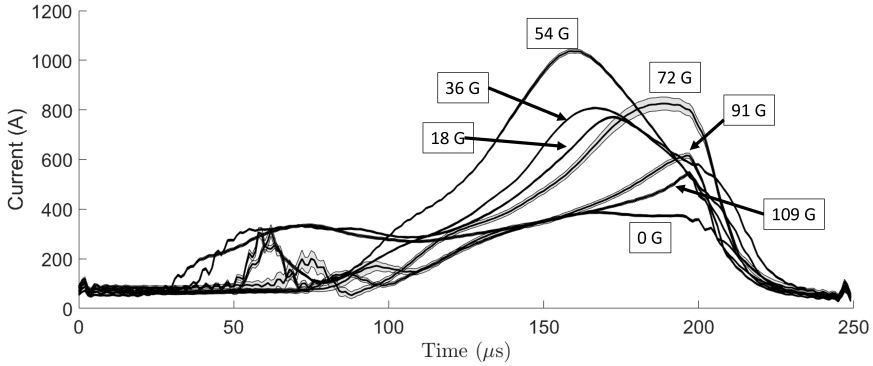


(b)

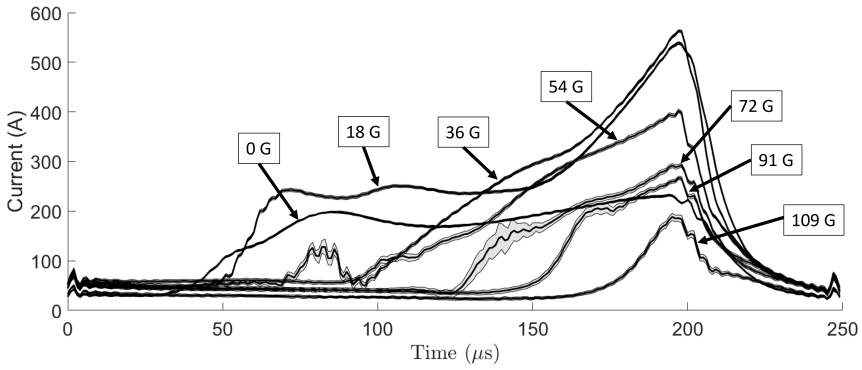


(c)

Figure 8.3: Total induced current versus time for all bias field strengths for the a) 350 V, b) 275 V, and c) 200 V DC backing voltage series. For better resolution, the 200 V case is at half scale relative to the other plots.

## 8.4 Comparison to Theory

In this section, we wish to provide comparisons of current density maps between direct experimental measurement and the models presented in Chapter 2 by examining the 350 V series whose current vs time traces are shown in Fig. 8.3. The 350 V case is chosen because the RMF is able to fully couple to and ionize the plasma for all bias field strengths, as opposed to the lower voltage conditions where higher bias strength pulses are cut off before a current maximum can be achieved.

### 8.4.1 Model Inputs

In this analysis we have treated magnetic field strengths, electron temperature, and electron number per axial slice as known parameters to solve for drift velocities.

Bias magnetic field is known because we have measured it using a Hall sensor, with ther resulting the bias field shape shown in Fig.7.2. This field is constant in time. A higher degree of coupling is associated with a lower amplitude. The induced field, which is required for the updated analysis, is also a strong function of time. To select the moment in time for which we make our comparison between theory and experiment, we wish to identify when the plasma is fully ionized and the current has been fully driven. We observe in our results in Fig. 8.3 that the total induced current across these conditions tends to reach a maximum. We therefore select the time for which the total current peaks to perform our comparison.

Electron temperature, important for calculating electron-ion collision frequency and pressure gradients, has been assumed constant in both analyses. While we do not have bulk electron temperature measurements for the operating conditions used in this study, it was found for the previous iteration of this thruster that electron temperatures typically peaked at ∼8-9 eV [87], and this peak occurred roughly simultaneously with the peak in total induced current [76]. Therefore we select 8 eV as the electron temperature for this analysis.

Finally we must determine the values to be used for $N_0$, the number of electrons per axial slice of the thruster which requires several assumptions, which in turn are motivated by observations made when operating the RMFv3 thruster and the RMFv2 thruster. First, we note that the ionization fraction is very high, with mass utilization approaching unity for the RMFv2 [88]. Second, we observe that total induced current tends to remain at zero for a period of time after the RMF pulse begins whose length depends on several parameters, but after this time the induced current rises to a peak before decaying back to zero as the plasma is ejected [76]. We then make the following assumptions:

- The pre-pulse neutral density is dictated by neutral diffusion through the thruster cone

at thermal speed $c_{th} = \sqrt{\frac{8eT_{eV}}{2\pi M}}$ for atomic mass $M$.

- The electrons present in the cone begin at 100% ionization of the pre-pulse neutrals at the moment when the total induced current begins to rise.
- The total number of electrons decays linearly to zero at the point when the total induced current returns to zero.
- The relative profile of the electron number per axial slice (i.e. $\frac{1}{N_0}\frac{\partial N_0}{\partial z}$) is constant with time.

These assumptions together provide the result

$$N_0 = \frac{t_1}{t_2 - t_0}\frac{4\dot{m}}{Mc_{th}} \tag{8.1}$$

where $t_0$ is the time at which the plasma current begins to rise, $t_1$ is the time at which we wish to apply these models, and $t_2$ is the time at which the current returns to zero after having ejected the plasma.

### 8.4.2 Results

Significantly, the Blevin and Thonemann current drive model does not apply to any of these conditions as $1\frac{4\pi B_0}{\mu_0 N_0 e\omega} < 1$ everywhere for each case presented here. Therefore Eq. 2.26 predicts a negative current density in this device, which is nonphysical. The bias field's strength relative to the RMF is the cause for this unrealistic prediction. Key to the derivation of Eq. 2.26 is the assumption that the electrons rotate synchronously with the RMF which allows the differential equation for $n(r)$ to be analytically solved self-consistently with the induced field. However, in the case of non-synchronous rotation—which it appears is the case in this device—the induced field will be weaker than is anticipated by this theory and therefore confinement will be enhanced relative to the model. In light of the apparent non-applicability of the Blevin and Thonemann model to this device, Fig. 8.4 shows comparisons of measured plasma current density and that predicted by our updated model for the 350 V series already discussed in the previous subsection. Magnetic field streamlines are overlaid onto the current density to provide additional context. The domain of the measured current is smaller than that of the thruster volume because the spatial derivatives required to calculate current density cannot be evaluated on the edge of the probed domain. The predicted current, however, does not require the derivative of the field measurements and therefore has the same $z - r$ domain as that of Fig. 8.1.

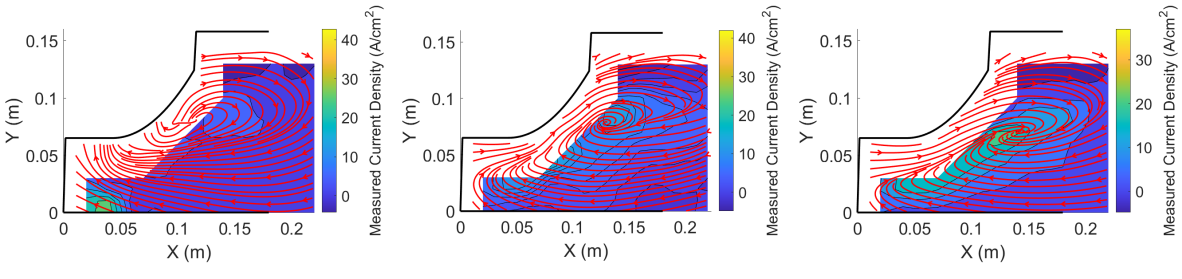


(a) 0 G Measured (b) 18 G Measured (c) 36 G Measured

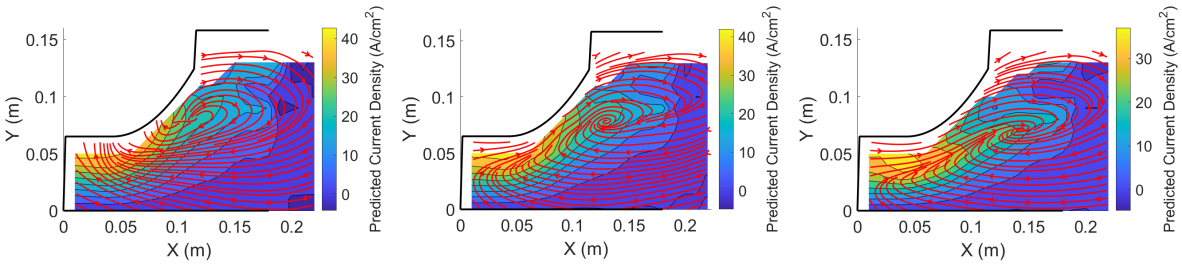


(d) 0 G Predicted (e) 18 G Predicted (f) 36 G Predicted

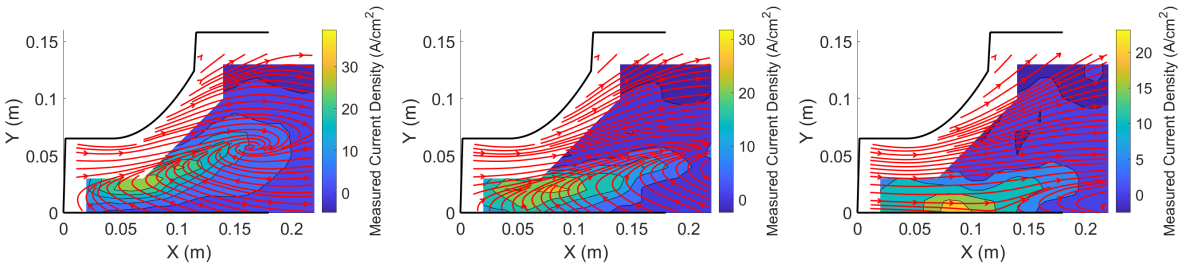


(g) 54 G Measured (h) 72 G Measured (i) 91 G Measured

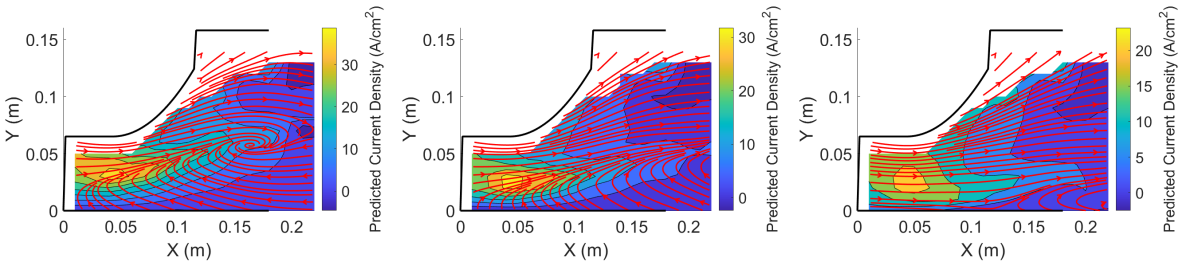


(j) 54 G Predicted (k) 72 G Predicted (l) 91 G Predicted

Figure 8.4: Comparison of measured and predicted current density, overlaid with magnetic field streamlines for the 350 V supply voltage, 200 $\mu$s pulse length, 120 sccm Xe rear flow condition, with bias magnet current at 0 G (a,d), 18 G (b,e), 2 (c,f), 54 G (g,j), 72 G (h,k), 91 G (i,l)

As anticipated, we see poor agreement between experiment and theory at low bias field strengths where the model dramatically over predicts the current drive. Indeed, the predicted current peaks against the wall of the thruster where it would quickly be quenched by the close contact with the pyrex wall. This poor agreement remains until the 54 G case where the separatrix has shifted radially inwards sufficiently to reduce electron/wall contact. At this condition we see qualitative agreement but ∼50% difference in peak current density value. At the 72 G condition, which corresponds to peak Lorentz impulse, we see excellent matching between the model and experiment, with both the shape and magnitude of the high current density region agreeing. At the 91 G condition when Lorentz force has reduced again, we continue to see agreement in magnitude, but the location of high current drive is shifted relative to experiment. At this condition, as will be shown in Fig. 8.6, ∼20% of the impulse generated at this condition is estimated to be due to the diamagnetic drift current which depends chiefly on the electron pressure distribution, the weakest portion of the current drive theory that requires the most assumptions. Taken together, we draw the conclusion that the drift velocities calculated are likely accurate across all conditions while it is the assumptions for density which fail at off-nominal magnetic field strengths.

## 8.5 Discussion

### 8.5.1 Model Drawbacks

While our updated model enjoys success at reproducing thruster current drive behavior and explaining heretofore unresolved questions about practical thruster behavior, it is not without drawbacks. Most significantly, this is not a predictive model. Without including the induced field, which must be measured directly, this model would not produce reasonable current drive results because the induced field is of similar magnitude to the bias field and the rotating field. It is therefore useful as an explanatory theory, but cannot directly guide the design of a new, more efficient device. The calculation of an induced field from an arbitrary current density distribution is by nature a complex process because the Biot-Savart Law must be integrated over all space. Therefore, self-consistently solving for current density including the induced field is impossible without either numerical simulation or strong symmetry assumptions such as Blevin and Thonemann made.

Even given the number of relaxed assumptions made in the derivation of our updated current drive model in in Chapter 2, we still anticipate that some simplifications made may not be completely true to reality, especially in regards to electron density distribution. Pressure gradients clearly exist in the axial direction, for example, which is inconsistent with

our assumption that these gradients occur only radially. The inclusion of such an effect would preclude the zero-dimensional nature of this analysis as it would then be necessary to self-consistently solve a two-dimensional partial differential equation for the electron density along with Eqs. 2.14-2.16. Ignoring this effect allows an algebraic solution to exist but requires further assumptions for the axial density distribution, which given the realities of propellant injection and axial electron mobility may not be fully accurate. Finally, this model provides no means of determining the degree of ionization experienced by the plasma, which we believe is the cause of our overestimation of current density at low bias field strengths. We anticipate that this may also cause overestimation of current density at very high bias field strengths not investigated in this study because experimental evidence shows that at sufficient bias fields the plasma will not ionize at all.

In summary, we suspect that no algebraic theory will be able to capture the complex physics involved in the RMF thruster. Its fundamental nature as a three-dimensional time-resolved problem necessitate numerical solutions of a second order system of differential equations, even under the simplifications associated with representing the system as Ohm's Law which ignores mass continuity and energy conservation. The key to an intuitive picture of device operation therefore is to relax those assumptions which are most critical to recover observed behavior. We believe that, despite the drawbacks listed above, we have struck a balance to describe thruster operation simply and intuitively while capturing the most relevant physics. However, the assumptions required to derive the model, in particular those necessary to arrive at the electron density distribution, should be kept in mind when applying it.

### 8.5.2 Model Implications for Current Drive

Despite the drawbacks discussed above, our updated model shows good quantitative agreement to experiment in a regime where the established theory predicts nonphysical behavior and qualitatively explains many of the challenges we have experienced while testing the RMF thruster. Therefore, even if it does not perfectly capture every aspect of the physics involved, we can still apply it to draw conclusions about the operation of the thruster.

In the previous subsection we have asserted that the Blevin and Thonemann density model is not applicable to this device because of its assumption of synchronous electron rotation with the RMF. To quantify the synchronicity of rotation, we employ the concept of slip from the design of induction motors:

$$s = 1 - \frac{\omega_e}{\omega} = 1 - \frac{v_\phi}{r\omega} \tag{8.2}$$

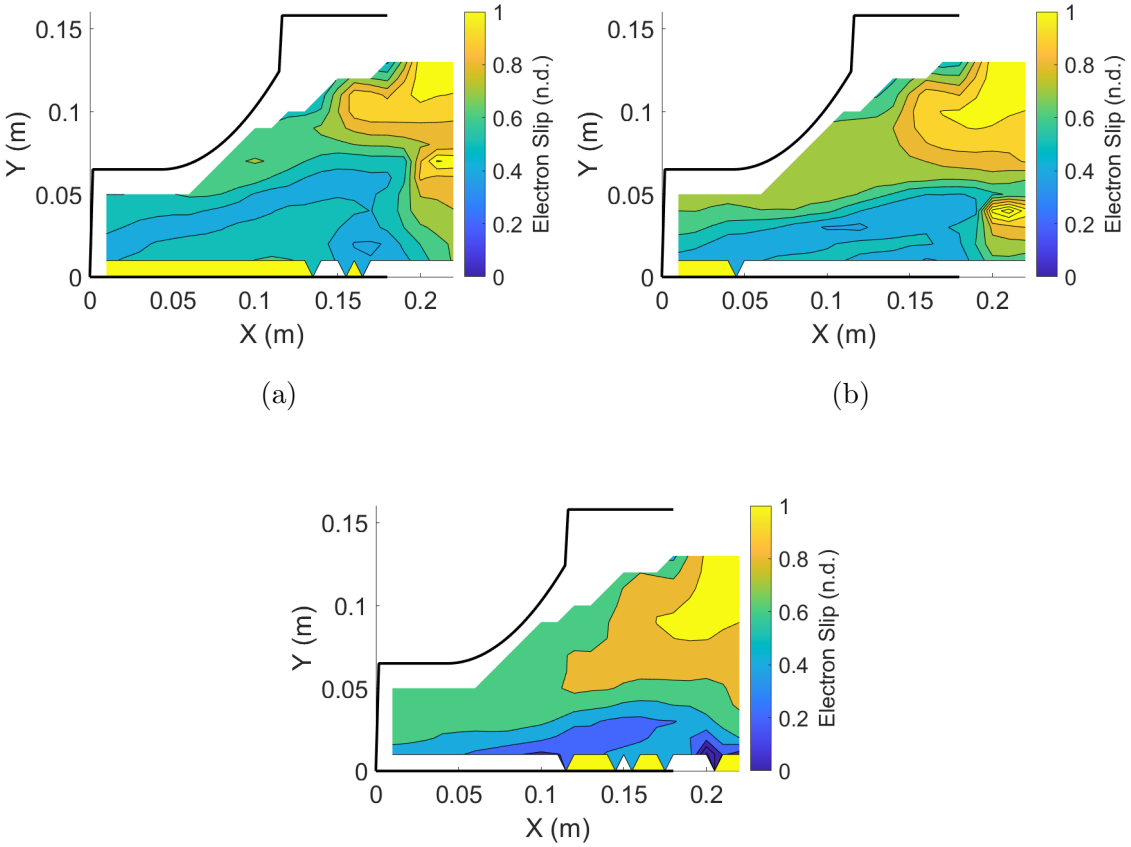


(a) (b)

(c)

Figure 8.5: Predicted electron slip for the 350 V series for a) 54 G, b) 72 G, and c) 91 G magnet current

where $s$ is slip, $\omega_3 = \frac{v_\phi}{r}$ refers to the actual rotation frequency of the electrons as predicted by our azimuthal drift velocity and the local radius, and $\omega$ is the RMF frequency. A slip of 1 implies stationary electrons, while a slip of 0 implies synchronous rotation. By taking our theoretical drift velocity as correct, we can compute slip without any assumptions for electron density.

Fig. 8.5 shows the predicted electron slip for the three cases discussed in Fig. 8.4 which show good agreement to experiment: 54 G, 72 G, and 91 G magnet current. High slip is observed across all three cases, with the region of lowest slip being close to the axis in the 91 G condition with a slip of $s \approx 0.33$. Throughout most of the volume of the thruster, the slip is greater than or approximately equal to 0.5 and increases with the bias field strength. This confirms our assertion that the analysis leading to Eq. 2.26 is invalid due to the assumption of synchronous rotation. Further, the slip is caused by the allowance for radial electron

velocity to provide a mechanism by which the axial bias field can slow azimuthal electron motion. The region of Fig. 8.5c with reduced slip can be attributed to enhanced diamagnetic drift caused by a steep density gradient in that location. This location also corresponds to a region of relatively high experimentally measured current drive (Fig. 8.4i). It is possible that the densities in this region are higher in reality than are dictated by our assumptions, leading to this behavior.

The relative significance of diamagnetic drift versus RMF drift when calculating slip begs an investigation into the significance of each when calculating Lorentz-based impulse. Fig. 8.6 shows a breakdown of predicted impulse due to the diamagnetic drift current $j_D = \frac{\nabla P_r B_z}{|B|^2}$ versus the total current $j_\phi = en_e \frac{-E_z B_r}{|B|^2} + \frac{\nabla P_r B_z}{|B|^2}$ for those operating conditions with the degree of confinement that the theory presented in this paper agrees with experiment. We see that as the bias current is increased, the relative fraction of the impulse which arises from the diamagnetic drift increases as the electrons are more effectively confined and density gradients become steeper. Additionally, the fraction of impulse caused by diamagnetic drift is not a strong function of the RMF strength. This physically suggests that although the RMF drift $j_\phi$ is reduced as RMF strength is reduced, the correspondingly lower induced magnetic field is less able to create a region of low total field strength for electrons to reside in at high density, reducing the diamagnetic drift $j_D$ commensurately.

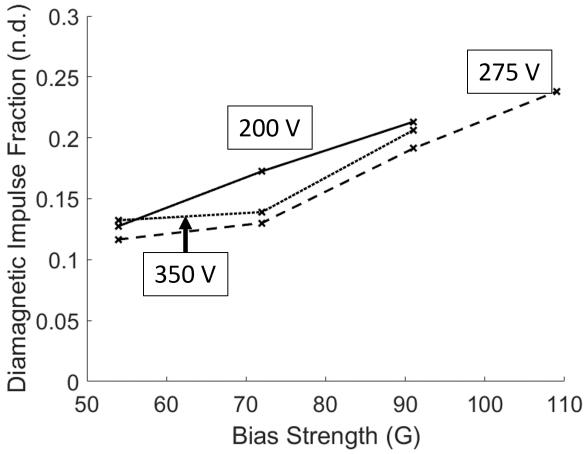


Figure 8.6: Predicted impulse due to the diamagnetic drift as a fraction of total predicted impulse.

### 8.5.3 Model Implications for Thruster Design

As discussed in Sec. 6.4.4, our updated model is able to successfully reproduce thruster behavior where the Blevin and Thonemann model cannot. In particular, we find that by

relaxing the assumption of zero radial electron velocity, the bias field is provided a mechanism by which it can retard electron motion by the rotating magnetic field, which is consistent with experimental evidence across many flow rates, pulse lenghts, and even CW-mode (i.e. 100% duty cycle) operation that an optimal value for $\frac{B_0}{B_\omega}$ exists and that sufficiently high magnetic field prohibits ionization. Even in cases where the bias field's strength is optimal to produce thrust, the ∼50% rotational slip observed is sufficient to invalidate the assumption of synchronous rotation by the Blevin and Thonemann model which suggests that our bias field strengths are an order of magnitude too low for the propellant density present. While the Blevin and Thonemann model is attractive due to its self-consistent and predictive nature, we find that it is only valid in the limit that the RMF is significantly stronger than all other magnetic fields present.

We expect that for this device to function in the regime described by the Blevin and Thonemann model, we would need approximately an order of magnitude stronger RMF so that $B_\omega/gg B_0$. To approach such a condition without experiencing prohibitively high ohmic losses in the power processing circuitry and RMF transmission lines and antennas would require a commensurate reduction in the PPU's effective resistance (power per unit RMF magnitude). This can be improved by upgrading switching components to more efficient counterparts and optimizing the RMF antennas to account for skin depth, although both of these together are unlikely to provide the required improvement. We can also increase the number of turns in the RMF antennas to multiplicatively increase field strength per amp, although this comes with increased antenna voltage which may become prohibitively high in turn. These practical limitations on increasing RMF strength without increasing ohmic losses imply that achieving synchronous rotation in a thruster architecture, where electrical efficiency is of paramount importance, may not be feasible.

To then achieve radial pressure balance and thus a confined plasmoid to mitigate electron/wall losses, the density would be required to drop by an amount commensurate with the reduction in slip. At the limit of synchronous rotation, we would require roughly a factor of 10 reduction in densities such that $1 < \frac{4\pi B_0}{\mu_0 N_0 e \omega} < 2$ in Eq. 2.26. We suspect that to reach these low densities while maintaining a reasonable mass flow rate for thruster operation, CW-mode operation may be necessary. Such a mode would sacrifice any impact of the structure field in exchange for these lower densities, which have the additional benefit of reduced wall and radiative losses. Even at the RMF amplitudes tested for this device which are on par with bias field strengths, we observed that performance improved by a factor of ∼2.5 when operating in CW-mode.

Taking these arguments together, we believe that CW-mode should be the focus of future efforts for this device. Further, this discussion suggests a thruster design process. First, we

make the assumption that the RMF strength is much greater than the bias field strength to ensure synchronous electron rotation. After determining an anticipated plasma density during thruster operation, the bias field strength can be set to ensure plasma confinement via Blevin and Thonemann's FRC indication term $1 < \frac{4\pi B_0}{\mu_0 N_0 e \omega} < 2$. To maintain the RMF strength assumption, this in turn sets the RMF amplitude. The major remaining challenge is a reasonable determination of $n_e$ during operation, which will require a self-consistent solution between propellant flow rate and the bias field strength and shape given an RMF frequency. Such a solution will likely require computational modelling of the thruster. We also wish to emphasize that this new analysis does not place additional constraints on the RMF frequency $\omega$ apart from the Jones and Hugrass penetration condition Eq. 2.27 which we have already been considering in the thruster design process. Further, given that the RMF must be so strong compared to the bias field, which in turn must be strong enough to confine the plasma, we do not anticipate this condition to be challenging to meet. Therefore, the RMF frequency should be increased as much as the switching circuitry will allow, anticipating that a higher frequency corresponds to a more demanding circuit design.

## 8.6 Conclusions

In this chapter we have presented the main performance limitation of the RMFv3 thruster, current drive behavior. We have shown that the current drive and magnetic field structure does not match the established theory for RMF current drive, and instead agrees well with our updated model. This model in turn suggests that our RMF strength is much too low in comparison with the bias field strength to achieve high entrainment and therefore synchronous rotation with the RMF. We have followed this with a discussion for how this applies to thruster design. In particular, the scaling suggested by the model implies that pulsed-mode operation is unlikely to ever be able to achieve synchronous rotation with the field strengths available to a thruster architecture where RMF current and input power is of paramount importance. CW-mode's lower densities, however, may enable efficient operation for that mode. We then suggest a possible design path for a future CW-mode thruster.

# CHAPTER 9

# Conclusions and Future Work

## 9.1 Summary

In Chapter 1 we introduce the goals and organization of this work. We provide context for this research by briefly discussing rocket propulsion as a whole before focusing on electric propulsion in particular. We introduce some key figures of merit to describe these devices and describe the baseline plasma physics required for the rest of the work. We provide further background detail in Chapter 2 by focusing on the operating principles of the RMF thruster, and present our updated model for RMF current generation and contrast it with established theory. In Chapter 3 we discuss the physical setup required to do testing on an RMF thruster, including the facility, thrust stand, and probes. Chapter 4 follows with a description of how the data from these apparatus can be analyzed to produce meaningful results.

We arrive at the thrust of this work beginning in Chapter 5, which tells the story of the design and construction of the PEPL RMFv2 thruster as well as its baseline performance characterization. We find here that the overall performance of this device, which is operated only in the pulsed-mode, is prohibitively low. However, plasma probing and further analysis in Chapter 6 suggested that changes to the bias magnetic field and a shift to CW-mode operation may serve to eliminate the worst of the loss mechanisms identified. Because the results of those experiments directly motivate the design and testing of the RMFv3 thruster, this leads into Chapter 7, which focuses on the design and baseline characterization of that device. We find that while CW-mode operation provides nearly a factor of four improvement over pulsed-mode at similar conditions, overall performance is still low. Additionally, we find that thruster behavior does not match the established theory as the bias field strength is adjusted, displaying clear performance optima with bias strength. In Chapter 8 we show that trends with changing bias field strength, which can now be resolved on the new device show qualitative agreement with what can be expected from our updated theory. This

theory is validated by comparing predictions of current density with experiment and showing quantitative agreement.

## 9.2 Contributions to the Field

The primary goal of this work was to improve the understanding of the performance and behavior of the RMF thruster from the perspective of RMF current drive and Lorentz force. A necessary step toward that objective was to design and build a test article on which we may experiment. That done, thruster performance could be characterized and the physics behind plasma acceleration can be investigated. In this work, this cycle of thruster design, build, and characterization was repeated twice as we discovered where to seek greater understanding of the physics at play. Major contributions in this work included:

1. **The first direct thrust measurement of an RMF thruster in both pulsed-mode and CW-mode.** We used an inverted-pendulum thrust stand to make direct performance measurements on two thrusters, the PEPL RMFv2 and PEPL RMFv3, over a wide variety of operating conditions. The design of the RMFv3, which is capable of CW-mode operation, was motivated by findings for the v2 thruster. It is found that, consistent with the hypotheses which inspired its construction, the CW-mode dramatically reduces the primary energy loss mechanisms present in the pulsed-mode. Further, trends are observed with changing bias magnetic field strength that are not explained by theory to-date.

2. **The first direct measurement of field-reversed configuration (FRC) formation and translation in an RMF thruster.** While excluded flux probes were used in other RMF thrusters to infer field reversal and therefore FRC formation, we provide a direct time-resolved picture of the fields present in the thruster by means of inductive probing. We show FRC formation, acceleration, and ejection which matches qualitatively with structures observed using high-speed video of the thruster plume.

3. **The derivation and validation of an updated current drive model for the RMF scheme.** Motivated by experimental measurement of the RMFv3 thruster's performance with changing bias magnetic field strength, a new current drive model is derived. It is found that the current drive model in use in the field of RMF thrusters since its derivation in 1962 is only applicable under more restrictive conditions than previously understood. The new model accurately and quantitatively predicts values for current density measured in the RMFv3 thruster.

## 9.3 Implications

We wish to highlight here the major takeaways from this work. Perhaps most significantly, we have shown that the established current drive model used in the design of each RMF thruster of which we are aware does not in fact apply in the regime we operate. This fundamentally changes our outlook on how to pursue an efficient device. We have shown in our updated theory that an enhanced bias magnetic field serves to retard azimuthal electron motion, and therefore that to avoid high electron slip the RMF strength must be much greater than the bias field strength. Meanwhile the ideal bias field strength is set by the condition that it be commensurate in magnitude with the induced magnetic field. This implies that propellant densities dictate bias field strength which in turn dictates RMF strength. This drives us to lower flow rates and higher field amplitudes than have been considered in the past. Further, we expect that the high densities associated with pulsed-mode operation for reasonable mass flow rates would require prohibitively high rotating field strengths.

We have also demonstrated experimentally that pulsed-mode operation is much less efficient than CW-mode for the RMF thruster, with an efficiency gap of nearly four times at otherwise like operating conditions. In the regimes we tested we believe that this improvement is likely due to a reduction in loss mechanisms. However, when taken together with the conclusions regarding required field strengths, we believe this eliminates pulsed-mode operation as a useful direction of research.

We have made the first published direct thrust measurements for an RMF thruster. While this was a prerequisite for the previous two conclusions, it is a significant result in and of itself, as it shows unequivocally the performance of these devices is suboptimal under the present operating conditions.

## 9.4 Future Work

Although throughout the course of this work we have uncovered additional physics that grant insight into the behavior of the RMF thruster, there is still much to be learned. We discuss here a few avenues for additional research.

### 9.4.1 Improving CW-Mode Operation

As discussed previously, we believe that the results shown throughout this work point to the conclusion that future efforts on the RMF thruster should be focused on CW-mode operation. The lower densities associated with CW-mode allow lower bias field strengths to be employed for synchronously-rotating electrons, which in turn allow lower RMF strengths

to enable synchronous rotation. With this in mind, even at the lower densities from CW-mode, we expect that a much higher RMF strength than the RMFv3 is capable of is necessary for ideal current drive. While this can be done in a straightforward manner by increasing RMF current amplitude, such a strategy would also cause increased ohmic losses in the power circuitry and transmission lines. These losses, which scale quadratically with current, would serve to reduce the coupling efficiency. Therefore it is imperative to investigate means of increasing the RMF field strengths without a commensurate increase to the current supplied.

One possible strategy is to increase the number of turns on each leg of the RMF antenna. While this would reduce the current required to reach a given field strength, it would also increase the voltage across the antenna—and therefore across the tuning capacitor banks—for that same increased field. At present, because the thruster is designed to be compatible with both high amplitude burst (pulsed-mode operation) and low amplitude sustained currents (CW-mode operation) a balance must be struck in the design of the capacitor banks between current rating and voltage rating. By focusing on CW-mode performance, therefore, the number of turns on the antenna could be increased safely while keeping voltages under a reasonable limit. This would amplify the RMF for the same current output from the supply.

Alternative geometries for the thruster can also be identified toward increasing the rotational field strength. One such option is inspired by annular theta-pinch FRC experiments [97, 98]. Because the currents generated in the thruster have been shown to fill only a narrow radial band, a coaxial design could be implemented to better use the space close to the axis of the thruster. By opening up this volume for design, additional RMF antennas could be implemented for use in concert with the existing antennas on the outer radius. By firing both sets at once, the radial field could be further improved.

### 9.4.2 Thruster Modelling

Now that we have a current drive model which accurately predicts the azimuthal drift velocities of the electrons in the RMF thruster, we propose that this model should be integrated into simulation. The key weaknesses of our model are a) that the difficulty of analytically determining the induced field precludes a closed-form solution for the magnetic field and b) the introduction of new physics necessary to accurately resolve drift velocities then requires further assumptions about the plasma density distribution. However, by incorporating Ohm's Law into a quasi 1D model, for example, these difficulties could be solved in large part. This would then enable better performance prediction for a thruster and aid in design before committing to a geometry and power processing unit architecture.

## 9.5 Concluding Remarks

We believe based on the results and analysis presented here that future research effort should not be placed toward pulsed-mode operation. The high plasma densities associated with pulsed-mode operation lead to unacceptable radiation losses and wall losses. We believe that wall losses could be mitigated through an enhanced bias field to reduce radial electron mobility. According to our updated current drive theory, however, to do so would require commensurately higher rotating field strengths to maintain a high enough drift velocity for full ionization of the propellant gas. The resulting high RMF antenna currents defeat a primary advantage the RMF thruster has over other IPPTs, namely that the lower antenna currents and therefore transient voltages reduce concerns for power supply design and lifetime. Meanwhile, radiation losses are only avoidable via reduced electron densities. These lower densities would reduce the rate of plasma current rise, reducing the impact of the structure field and removing the quadratic thust scaling which allow the RMF thruster to be properly considered an IPPT. Taken together, we see that the only methods to eliminate these crippling losses also eliminate in turn the pulsed RMF thruster's unique advantages.

We also expect based on these results that any CW-mode thrusters will require significantly higher RMF strengths than have been implemented to date on this thruster to achieve enhanced current drive. The key challenge to overcome will be to maintain these high field amplitudes without Ohmic losses in the transmission lines and power switching circuitry driving poor coupling efficiency. The combination of enhanced current amplitude and reduced plasma density will tend to drive poorer coupling. For the CW-mode RMF thruster to be effective, this consequence must be overcome.

This work represents an important step forward in our understanding of Rotating Magnetic Field thrusters. We have successfully performed direct performance measurements on two test articles and found performance trends that did not agree with established theory. This led therefore to the development of a new RMF current drive model to better explain this behavior. Our updated theory suggests that a dramatically different operating regime than what has currently been explored by any RMF thruster is required for efficient thrust generation. This will ultimately guide future research to explore efficient RMF thruster operation.

# BIBLIOGRAPHY


[1] Joshua M Woods, Christopher L Sercel, Tate Gill, and Benjamin Jorns. Performance measurements of a 60 kw field-reversed configuration thruster. In *AIAA Propulsion and Energy 2020 Forum*, page 3633, 2020.

[2] David Y Oh, Steve Collins, Tracy Drain, William Hart, Travis Imken, Kristina Larson, Danielle Marsh, Dhack Muthulingam, John Steven Snyder, Denis Trofimov, et al. Development of the psyche mission for nasa's discovery program. 2019.

[3] Christopher A. Dodson and Benjamin A. Jorns. Capabilities enabled in cislunar space by low specific mass solar electric power and propulsion systems. In *2023 AIAA Ascend Conference*, 2023.

[4] Giulio Coral, Kiyoshi Kinefuchi, Daisuke Nakata, Ryudo Tsukizaki, Kazutaka Nishiyama, and Hitoshi Kuninaka. Design and testing of additively manufactured high-efficiency resistojet on hydrogen propellant. *Acta Astronautica*, 181:14–27, 2021.

[5] Birk Wollenhaupt, Quang Hoa Le, and Georg Herdrich. Overview of thermal arcjet thruster development. *Aircraft Engineering and Aerospace Technology*, 90(2):280–301, 2018.

[6] Shadrach Hepner. *The Influence of Instabilities on the Electron Dynamics of a Magnetic Nozzle*. PhD thesis, University of Michigan, 2022.

[7] Benjamin Wachs. *Optimization and Characterization of Facility Effects for a Low-Power Electron Cyclotron Resonance Magnetic Nozzle Thruster*. PhD thesis, University of Michigan, 2022.

[8] Kristof Holste, Patrick Dietz, Steffen Scharmann, Konstantin Keil, Thomas Henning, Daniel Zschätzsch, M Reitemeyer, Benny Nauschütt, F Kiefer, F Kunze, et al. Ion thrusters for electric propulsion: Scientific issues developing a niche technology into a game changer. *Review of Scientific Instruments*, 91(6), 2020.

[9] Collin B Whittaker, Henry A Sodano, and Benjamin A Jorns. A resilient extractor for electrospray arrays. In *37th International Electric Propulsion Conference (IEPC)*, number IEPC-2022-206, 2022.

[10] CB Whittaker and BA Jorns. Modeling multi-site emission in porous electrosprays resulting from variable electric field and meniscus size. *Journal of Applied Physics*, 134(8), 2023.

[11] K Uematsu, S Morimoto, and K Kuriki. Mpd thruster performance with various propellants. *Journal of Spacecraft and Rockets*, 22(4):412–416, 1985.

[12] Kurt A Polzin. Comprehensive review of planar pulsed inductive plasma thruster research and technology. *Journal of Propulsion and Power*, 27(3):513–531, 2011.

[13] Leanne Su. *Performance of a Magnetically Shielded Hall Thruster Operating on Krypton at High Powers*. PhD thesis, University of Michigan, 2023.

[14] Richard R Hofer, Sarah E Cusson, Robert B Lobbia, and Alec D Gallimore. The h9 magnetically shielded hall thruster. In *35th International Electric Propulsion Conference*, pages 2017–232. Electric Rocket Propulsion Soc., 2017.

[15] M Anand, Ian A Crawford, M Balat-Pichelin, S Abanades, W Van Westrenen, G Péraudeau, R Jaumann, and W Seboldt. A brief review of chemical and mineralogical resources on the moon and likely initial in situ resource utilization (isru) applications. *Planetary and Space Science*, 74(1):42–48, 2012.

[16] Alex Ellery. Sustainable in-situ resource utilization on the moon. *Planetary and Space Science*, 184:104870, 2020.

[17] Stanley O Starr and Anthony C Muscatello. Mars in situ resource utilization: a review. *Planetary and Space Science*, 182:104824, 2020.

[18] Joshua L Rovey, Christopher T Lyne, Alex J Mundahl, Nicolas Rasmont, Matthew S Glascock, Mitchell J Wainwright, and Steven P Berg. Review of multimode space propulsion. *Progress in Aerospace Sciences*, 118:100627, 2020.

[19] Kurt Polzin, Adam Martin, Justin Little, Curtis Promislow, Benjamin Jorns, and Joshua Woods. State-of-the-art and advancement paths for inductive pulsed plasma thrusters. *Aerospace*, 7(8):105, 2020.

[20] C Lee Dailey and Ralph H Lovberg. The pit mkv pulsed inductive thruster. Technical report, Lewis Research Center, 1993.

[21] Ashley K Hallock, Adam K Martin, Kurt A Polzin, Adam C Kimberlin, and Richard H Eskridge. Single-and repetitive-pulse conical theta-pinch inductive pulsed plasma thruster performance. *IEEE Transactions on Plasma Science*, 43(1):433–443, 2014.

[22] Stirling A Colgate and Harold P Furth. Stabilization of pinch discharges. *The Physics of Fluids*, 3(6):982–1000, 1960.

[23] K Hirano. Steady state theta pinch concept for slow formation of frc. Technical report, Nagoya Univ.(Japan). Inst. of Plasma Physics, 1987.

[24] JT Slough, AL Hoffman, and RD Milroy. Formation studies of field-reversed configurations in a slow field-reversed theta pinch. *Physics of Fluids B: Plasma Physics*, 1(4):840–850, 1989.

[25] M Tuszewski, DP Taggart, RE Chrien, DJ Rej, RE Siemon, and BL Wright. Axial dynamics in field-reversed theta pinches. ii: Stability. *Physics of Fluids B: Plasma Physics*, 3(10):2856–2870, 1991.

[26] GA Wurden, TP Intrator, SY Zhang, IG Furno, SC Hsu, JY Park, R Kirkpatrick, RM Renneke, KF Schoenberg, MJ Taccetti, et al. Frc plasma studies on the frx-l plasma injector for mtf. 2005.

[27] Thomas Weber, Ian Bean, John Boguski, and Evan Dodd. Modular theta-pinch experiment (mtx) overview and initial results. *Bulletin of the American Physical Society*, 2023.

[28] Ian Bean, Colin Adams, and Thomas Weber. Pre-ionization studies on the modular theta-pinch experiment (mtx) for field-reversed configuration (frc) formation. *Bulletin of the American Physical Society*, 2023.

[29] Syri Koelfgen, Clark Hawk, Richard Eskridge, Michael Lee, Adam Martin, and James Smith. A plasmoid thruster for space propulsion. In *39th AIAA/ASME/SAE/ASEE Joint Propulsion Conference and Exhibit*, page 4992, 2003.

[30] DE Kirtley, JT Slough, and G Votroubek. Neutral entrainment demonstration in a xenon frc thruster experiment. In *Joint Army Navy NASA Air Force Conference*, 2013.

[31] Carrie Hill, Nolan Uchizono, and Michael Holmes. Results on a 15-joule theta-pinch frc-physics test cell for space propulsion research. In *APS Division of Plasma Physics Meeting Abstracts*, volume 2014, pages UP8–024, 2014.

[32] John Slough and George Votroubek. Magnetically accelerated plasmoid (map) propulsion. In *42nd AIAA/ASME/SAE/ASEE Joint Propulsion Conference & Exhibit*, page 4654, 2006.

[33] John Slough, Arthur Blair, Chris Pihl, and George Votroubek. Magnetically accelerated plasmoid (map) thruster - initial results and future plans. *IEPC-2007-16*, 2007.

[34] Kathleen Quinlan, David B Cope, and Roger Myers. Magnetic induction plasma engine. *IEPC-2022-412*, 2022.

[35] Pavlos G Mikellides and Chris Neilly. Modeling and performance analysis of the pulsed inductive thruster. *Journal of propulsion and power*, 23(1):51–58, 2007.

[36] Pavlos G Mikellides and James K Villarreal. High energy pulsed inductive thruster modeling operating with ammonia propellant. *Journal of Applied Physics*, 102(10), 2007.

[37] Pavlos Mikellides and James Villarreal. Numerical modeling of a low energy pulsed inductive thruster. In *44th AIAA/ASME/SAE/ASEE Joint Propulsion Conference & Exhibit*, page 4726, 2008.

[38] RH Lovberg and CL Dailey. Large inductive thruster performance measurement. *AIAA Journal*, 20(7):971–977, 1982.

[39] Adam Martin and Richard Eskridge. Electrical coupling efficiency of inductive plasma accelerators. *Journal of Physics D: Applied Physics*, 38(23):4168, 2005.

[40] Kurt A Polzin and Edgar Y Choueiri. Performance optimization criteria for pulsed inductive plasma acceleration. *IEEE Transactions on Plasma Science*, 34(3):945–953, 2006.

[41] Ivana Hrbud, Michael LaPointe, Robert Vondra, C Lee Dailey, and Ralph Lovberg. Status of pulsed inductive thruster research. In *AIP conference proceedings*, volume 608, pages 627–632. American Institute of Physics, 2002.

[42] C.E. Myers, M.R. Edwards, B. Berlinger, A. Brooks, and S.A. Cohen. Passive superconducting flux conservers for rotating magnetic field driven field reversed configurations. *Fusion Science and Technology*, 61:86–103, 2012.

[43] CL Dailey and RH Lovberg. Pulsed inductive thruster component technology. *Final Report to Air Force Astronautics Laboratory, published Apr*, 1987.

[44] Adam K Martin, Alexandra Dominguez, Richard H Eskridge, Kurt A Polzin, Daniel P Riley, and Kevin A Perdue. Design and testing of a small inductive pulsed plasma thruster. In *International Electric Propulsion Conference (IEPC)*, number M15-4728 in 2015, 2015.

[45] Ashley K Hallock, Adam K Martin, Kurt A Polzin, Adam C Kimberlin, and Richard H Eskridge. Single-and repetitive-pulse conical theta-pinch inductive pulsed plasma thruster performance. *IEEE Transactions on Plasma Science*, 43(1):433–443, 2014.

[46] Edgar Y Choueiri and Kurt A Polzin. Faraday acceleration with radio-frequency assisted discharge. *Journal of Propulsion and Power*, 22(3):611–619, 2006.

[47] Dan Lev. *Investigation of efficiency in applied field magnetoplasmadynamic thrusters*. PhD thesis, Princeton University, 2012.

[48] Roger Myers, Michael Lapointe, and Maris Mantenieks. Mpd thruster technology. In *Conference on Advanced SEI Technologies*, page 3568, 1991.

[49] National Academies of Sciences Engineering and Medicine. *Space Nuclear Propulsion for Human Mars Exploration*. The National Academies Press, Washington, DC, 2021.

[50] H. A. Blevin and P. C. Thonemann. Plasma confinement using an alternating magnetic field. *Nuclear Fusion Supplement, Part 1*, page 55, 1962.

[51] W N Hugrass, T Okada, and M Ohnishi. Plasma-circuit interactions in rotating magnetic field current drive. *Plasma Physics and Controlled Fusion*, 50:055008, February 2008.

[52] Richard E Siemon, W Thomas Armstrong, Daniel C Barnes, R Richard Bartsch, Robert E Chrien, James C Cochrane, Waheed N Hugrass, Ralph W Kewish Jr, Phillip L Klingner, H Ralph Lewis, et al. Review of the los alamos frx-c experiment. *Fusion Technology*, 9(1):13–37, 1986.

[53] Kenneth Miller, John Slough, and Alan Hoffman. An overview of the star thrust experiment. In *AIP Conference Proceedings*, volume 420, pages 1352–1358. AIP Publishing, 1998.

[54] JT Slough and KE Miller. Enhanced confinement and stability of a field-reversed configuration with rotating magnetic field current drive. *Physical Review Letters*, 85(7):1444, 2000.

[55] John Slough, David Kirtley, and Thomas Weber. Pulsed plasmoid propulsion: The elf thruster. In *31th International Electric Propulsion Conference*, pages 20–24, 2009.

[56] TE Weber, JT Slough, and D Kirtley. The electrodeless lorentz force (elf) thruster experimental facility. *Review of Scientific Instruments*, 83(11), 2012.

[57] Thomas E. Weber. *The Electrodeless Lorentz Force Thruster Experiment*. PhD thesis, University of Washington, 2010.

[58] David Kirtley, Anthony Pancotti, John Slough, and Christopher Pihl. Steady operation of an frc thruster on martian atmosphere and liquid water propellants. In *48th AIAA/ASME/SAE/ASEE Joint Propulsion Conference & Exhibit*, page 4071, 2012.

[59] Daniel L Brown, Brian E Beal, and James M Haas. Air force research laboratory high power electric propulsion technology development. In *2010 IEEE Aerospace Conference*, pages 1–9. IEEE, 2010.

[60] T Furukawa, K Takizawa, D Kuwahara, and S Shinohara. Electrodeless plasma acceleration system using rotating magnetic field method. *AIP Advances*, 7(11):115204, 2017.

[61] T Furukawa, K Takizawa, K Yano, D Kuwahara, and S Shinohara. Spatial measurement in rotating magnetic field plasma acceleration method by using two-dimensional scanning instrument and thrust stand. *Review of Scientific Instruments*, 89(4):043505, 2018.

[62] T Furukawa, K Shimura, D Kuwahara, and S Shinohara. Verification of azimuthal current generation employing a rotating magnetic field plasma acceleration method in an open magnetic field configuration. *Physics of Plasmas*, 26(3):033505, 2019.

[63] T Furukawa, D Kuwahara, and S Shinohara. Spatial characteristics of rotating magnetic field (rmf) plasma acceleration method in open magnetic field configuration under partial rmf penetration. *Physics of Plasmas*, 28(7):073507, 2021.

[64] Kurt A Polzin, Ashley K Hallock, Kamesh Sankaran, and Justin M Little. *Circuit Modeling of Inductively-coupled Pulsed Accelerators*. CRC Press, 2022.

[65] KA Polzin, AK Martin, RH Eskridge, AC Kimberlin, BM Addona, AP Devineni, NR Dugal-Whitehead, and AK Hallock. Summary of the 2012 inductive pulsed plasma thruster development and testing program. Technical report, Marshall Space Flight Center, 2013.

[66] Richard H. Eskridge, Peter J. Fimognary, Adam K. Martin, and Michael H. Lee. Design and construction of the pt-1 prototype plasmoid thruster. *AIP Conference Proceedings*, pages 813, 474, 2006.

[67] Carrie S. Hill. Preliminary results on an annular field reversed configuration translation experiment. *IEPC-2011-281*, 2011.

[68] Carrie S Hill. *Translation studies on an annular field reversed configuration device for space propulsion*. Michigan Technological University, 2012.

[69] Joshua M Woods, Benjamin A Jorns, and Alec Gallimore. Scaling laws of rotating magnetic field field-reversed configuration thrusters. In *2018 Joint Propulsion Conference*, page 4911, 2018.

[70] Joshua M Woods, Christopher L Sercel, Tate M Gill, Eric Viges, and Benjamin A Jorns. Data-driven approach to modeling and development of a 30 kw field-reversed configuration thruster. In *36th International Electric Propulsion Conference (IEPC)*, 2019.

[71] Joshua M Woods, Christopher L Sercel, Tate Gill, and Benjamin Jorns. Equivalent circuit model for a rotating magnetic field thruster. In *AIAA Propulsion and Energy 2021 Forum*, page 3400, 2021.

[72] Joshua Woods. *Performance of a Rotating Magnetic Field Thruster*. PhD thesis, University of Michigan, 2022.

[73] Francis F Chen. *Introduction to plasma physics*. Springer Science & Business Media, 2012.

[74] Dan M. Goebel and Ira Katz. *Fundamentals of Electric Propulsion: Ion and Hall Thruster*. Jet Propulsion Laboratory, California Institute of Technology, 2008.

[75] Ieuan R Jones and Waheed N Hugrass. Steady-state solutions for the penetration of a rotating magnetic field into a plasma column. *Journal of Plasma Physics*, 26(3):441–453, 1981.

[76] Christopher Lee Sercel, Tate Marlow Gill, and Benjamin A Jorns. Inductive probe measurements in a rotating magnetic field thruster. *Plasma Sources Science and Technology*, 2023.

[77] Tate M Gill, Christopher L Sercel, and Benjamin A Jorns. Experimental investigation into efficiency loss in rotating magnetic field thrusters. In preparation.

[78] Robert G. Jahn. *Physics of Electric Propulsion*. McGraw-Hill Book Company, New York, 1968.

[79] Eric A Viges, Benjamin A Jorns, Alec D Gallimore, and JP Sheehan. University of michigan's upgraded large vacuum test facility. In *36th International Electric Propulsion Conference*, 2019.

[80] John W Dankanich, Mitchell Walker, Michael W Swiatek, and John T Yim. Recommended practice for pressure measurement and calculation of effective pumping speed in electric propulsion testing. *Journal of Propulsion and Power*, 33(3):668–680, 2017.

[81] Andrea R Wong, Alexandra Toftul, Kurt A Polzin, and J Boise Pearson. Non-contact thrust stand calibration method for repetitively pulsed electric thrusters. *Review of Scientific Instruments*, 83(2):025103, 2012.

[82] James E Polk, Anthony Pancotti, Thomas Haag, Scott King, Mitchell Walker, Joseph Blakely, and John Ziemer. Recommended practice for thrust measurement in electric propulsion testing. *Journal of Propulsion and Power*, 33(3):539–555, 2017.

[83] Kurt A Polzin, Carrie S Hill, Peter J Turchi, Rodney L Burton, Sarah Messer, Ralph H Lovberg, and Ashley K Hallock. Recommended practice for use of inductive magnetic field probes in electric propulsion testing. *Journal of Propulsion and Power*, 33(3):659–667, 2017.

[84] Kurt Alexander Polzin. *Faraday accelerator with radio-frequency assisted discharge (FARAD)*. PhD thesis, Princeton University, 2006.

[85] Sarah Cusson. *Impact of neutral density on the operation of high-power magnetically shielded Hall thrusters*. PhD thesis, University of Michigan, 2019.

[86] Christopher L Sercel, Joshua M Woods, Tate Gill, and Benjamin Jorns. Impact of flux conservers on performance of inductively driven pulsed plasmoid thrusters. In *AIAA Propulsion and Energy 2020 Forum*, page 3632, 2020.

[87] Tate Gill, Christopher L Sercel, Joshua M Woods, and Benjamin A Jorns. Experimental characterization of efficiency modes in a rotating magnetic field thruster. In *AIAA SCITECH 2022 Forum*, page 2191, 2022.

[88] Tate M Gill, Christopher L Sercel, and Benjamin A Jorns. Experimental investigation into mechanisms for energy loss in a rotating magnetic field thruster. In *37th International Electric Propulsion Conference*, 2022.

[89] Christopher L Sercel, Tate Gill, and Benjamin Jorns. Performance predictions for cw-mode operation of an rmf thruster. In *AIAA SCITECH 2023 Forum*, page 0449, 2023.

[90] Kazunori Takahashi, Aiki Chiba, Atsushi Komuro, and Akira Ando. Experimental identification of an azimuthal current in a magnetic nozzle of a radiofrequency plasma thruster. *Plasma Sources Science and Technology*, 25(5):055011, 2016.

[91] Ioannis Mikellides, Ira Katz, Myron Mandell, and J Snyder. A 1-d model of the hall-effect thruster with an exhaust region. In *37th Joint Propulsion Conference and Exhibit*, page 3505, 2001.

[92] Ml Hayashi. Luminous layers in the prebreakdown region of low pressure noble gases. *Journal of Physics D: Applied Physics*, 15(8):1411, 1982.

[93] Makoto Hayashi. Determination of electron-xenon total excitation cross-sections, from threshold to 100 ev, from experimental values of townsend's $\alpha$. *Journal of Physics D: Applied Physics*, 16(4):581, 1983.

[94] Christopher L Sercel, Tate Gill, Joshua M Woods, and Benjamin Jorns. Performance measurements of a 5 kw-class rotating magnetic field thruster. In *AIAA Propulsion and Energy 2021 Forum*, page 3384, 2021.

[95] Kazunori Takahashi. Thirty percent conversion efficiency from radiofrequency power to thrust energy in a magnetic nozzle plasma thruster. *Scientific reports*, 12(1):18618, 2022.

[96] Tate M Gill, Christopher L Sercel, and Benjamin A Jorns. Design of a power processing unit for a rotating magnetic field thruster. In preparation.

[97] David Kirtley, Alec D Gallimore, James Haas, and Michael Reilly. High density magnetized toroid formation and translation within xocot: An annular field reversed configuration plasma concept. In *Proceedings of the 30th International Electric Propulsion Conference, Florence, Italy*, pages 17–20, 2007.

[98] CS Niemela and LB King. Numerical optimization of an annular field reversed configuration translation experiment. In *31st International Electric Propulsion Conference*, Ann Arbor, Michigan, September 2009.